DISSERTATION

ON THE OBSERVED AND SIMULATED RESPONSES OF THE EXTRATROPICAL ATMOSPHERE TO SURFACE THERMAL FORCING

Submitted by
Samantha M. Wills
Department of Atmospheric Science

In partial fulfillment of the requirements
For the Degree of Doctor of Philosophy
Colorado State University
Fort Collins, Colorado
Spring 2019

Doctoral Committee:

Advisor: David W. J. Thompson

Michael Alexander
Elizabeth Barnes
Eric Maloney
Subhas Karan Venayagamoorthy

ABSTRACT

ON THE OBSERVED AND SIMULATED RESPONSES OF THE EXTRATROPICAL ATMOSPHERE TO SURFACE THERMAL FORCING

The ocean is an integral part of the climate system, and its closely-coupled interactions with the atmosphere system have wide-ranging impacts on the large-scale and local patterns of climate and weather variability from one region of the globe to another. Improvements in the resolution of satellite observations and numerical models over the past decade have led to a series of advances in understanding the role of the ocean in extratropical air-sea interaction. While the influence of the extratropical ocean can be relatively subtle and difficult to detect, recent studies have provided a growing body of evidence suggesting that the extratropical ocean has a potentially important influence on the atmospheric circulation on a wide variety of timescales. The aim of this thesis is to improve the current understanding on the role of the extratropical ocean in climate by 1) presenting new observational analyses on the relationships between midlatitude SST anomalies and the atmospheric circulation on subseasonal timescales and 2) providing a new, simplistic framework for interpreting the atmospheric response to surface thermal forcing across the globe in an idealized global climate model.

In the first theme of this thesis, observational analyses of daily-mean data are exploited to re-examine the evidence for midlatitude air-sea interaction over the Kuroshio-Oyashio Extension region, and important comparisons are drawn to a previous companion study over the Gulf Stream Extension region. The results indicate that during the boreal winter season, SST anomalies in both the Gulf Stream and Kuroshio-Oyashio Extension regions are associated with distinct spatial and temporal patterns of atmospheric variability that precede and follow peak amplitude in the SST field on daily-mean timescales. In particular, a very similar pattern of low pressure anomalies that develops over the warm SST anomalies is viewed as the most robust common aspect of the atmospheric “response” over both ocean basins. The least common aspect of the “response” is characterized by robust high pressure anomalies that develop over the North Atlantic and have a seemingly unique relationship to positive lower-tropospheric temperature anomalies generated over the Gulf Stream Extension region. These results suggest that extratropical SST anomalies on subseasonal timescales are capable of forcing significant changes in the large-scale atmospheric circulation through the transfer of heat from the ocean to the atmosphere.

Partially motivated by the results from the observational analyses, the second theme of this thesis presents a simplified model framework to critically assess the one-way influence of the ocean on the atmosphere at different locations across the globe. A series of steady-state and transient numerical experiments are designed to explore the atmospheric response to surface thermal forcing in an idealized “aquaplanet” configuration of the NCAR Community Atmosphere Model, Version 5.3. The results indicate that in each of the extratropical SST perturbation experiments, there is a consistent and robust steady-state atmospheric response (of similar sign and amplitude) to surface thermal forcing. The response is characterized by a hemispheric-scale, equivalent-barotropic pattern of atmospheric circulation anomalies reminiscent of the model’s leading mode of internal variability and is seemingly *independent* of the latitudinal placement of the heat source. This result is explored further, and a possible explanation of the consistent steady-state atmospheric circulation response is discussed.

ACKNOWLEDGMENTS

The author would like to thank Dr. David W. J. Thompson of the Department of Atmospheric Science at Colorado State University for serving as an advisor and providing wisdom and guidance throughout the graduate degree program. The author would also like to thank Dr. Michael Alexander, Dr. Elizabeth Barnes, Dr. Eric Maloney, and Dr. Subhas Karan Venayagamoorthy for serving on the Ph.D. committee and providing valuable insight. Finally, the author thanks her family and friends for their invaluable support, love, and encouragement over the years.

This material is based on work supported by the NASA Physical Oceanography program under Grant NNX13AQ04G and the NSF Climate Dynamics program under grant AGS-1734251. The author acknowledges high-performance computing support from Cheyenne (doi:10.5065/D6RX99HX) and Yellowstone (ark:/85065/d7wd3xhc) provided by NCAR's Computational and Information Systems Laboratory, sponsored by the National Science Foundation.

TABLE OF CONTENTS

CHAPTER 1: INTRODUCTION AND BACKGROUND

The ocean and the atmosphere form a closely coupled system in which heat, momentum, and water are exchanged across the air-sea interface. The interactions between the ocean and atmosphere play a key role in the Earth's complex climate system, controlling weather and climate patterns through the transport of energy across the globe. Given its high heat capacity and vast surface coverage (~ 70% of the Earth's surface), the ocean is capable of storing and releasing large quantities of heat, helping to regulate temperatures in the atmospheric boundary layer and influencing atmospheric motions. In turn, the general atmospheric circulation acts to force wind-driven upper ocean currents through the transfer of momentum, redistributing oceanic heat transport to other geographic locations between the tropics and the poles (e.g., Trenberth et al. 1990).

The relative impact of the ocean on the atmosphere in balancing diabatic (or radiative) heating varies greatly from one region of the globe to another. From a simple thermodynamic perspective, surface heat fluxes associated with tropical sea surface temperature (SST) anomalies are balanced by large changes in the vertical wind field (e.g., Hoskins and Karoly 1981), which can perturb the free-tropospheric circulation and have a notable impact on global climate (e.g., Horel and Wallace 1981). In contrast, the surface heat fluxes associated with midlatitude SST anomalies are readily balanced by modest changes in the *low-level* horizontal wind field since the horizontal gradients in temperature are relatively large (e.g., Hoskins and Karoly 1981). However, from a dynamic perspective, variations in both tropical and midlatitude SST *gradients* have also been found to induce surface convergence patterns that lead to deep convection on climatological-mean time scales (e.g., Lindzen and Nigam 1987; Back and Bretherton 2009; Minobe et al. 2008, 2010).

The dissertation is centered around two main themes aimed at improving the current understanding on the coupled ocean-atmosphere system, with specific emphasis on the role of the ocean and its impact on the large-scale atmospheric circulation. The first theme is based on a re-examination of the observational evidence for midlatitude air-sea interaction on *daily-mean* time scales, a topic which remains uncertain in the existing (but growing) body of literature. The second theme is based on numerical experiments that explore an idealized framework for understanding how the atmosphere responds to SST anomalies varying between the equator and the pole. In this chapter, Section 1.1 reviews the existing literature on the atmospheric response to diabatic heating in the Tropics on both climatological-mean and transient time scales. Section 1.2 provides an overview of midlatitude air-sea interaction and focuses on recent advancements in the field over the past decade, with emphasis on midlatitude SST variability. An outline and description of the remaining chapters in the dissertation are given in Section 1.3.

1.1 Tropical Air-Sea Interaction

In the Tropics (defined over the latitude belt between the Tropic of Capricorn and the Tropic of Cancer, or ~ 23.5°S - 23.5°N, respectively), the climatological-mean surface temperature distribution is largely horizontally uniform, with small zonal and meridional SST gradients in the eastern equatorial Pacific and the tropical Atlantic. The following sections explore the relative contributions of elevated surface heating and tropical SST gradients in forcing the boundary layer and free tropospheric circulation on climatological-mean and transient times scales.

1.1.1 The Climatological-Mean Atmospheric Response to Diabatic Heating

The climatological distribution of surface winds and convergence in the tropical belt is largely driven by the physical processes that influence surface pressure gradients; the two most common thermal influences are considered to be elevated heating by cumulus convection and SST gradients (e.g., Gill 1980; Lindzen and Nigam 1987; Chiang et al. 2001; Back and Bretherton 2009). It is argued that the relative influence of each process varies geographically across the Tropics, where one process tends to dominate over the other based on the surrounding environment. Theoretical explanations of each thermal influence are provided below.

The first theoretical framework for understanding the tropical atmospheric response to heating was proposed by Gill (1980), who hypothesized that the flow generated by latent heat release in cumulus towers is an important component of low-level convergence in the Tropics. To test this hypothesis, the author solves a set of shallow water equations for a simple two-layer model in which the atmosphere has a first baroclinic mode (i.e., waves are strongly coupled and out of phase). The analytical solutions for an elevated heating symmetric about the equator are shown in Fig. 1.1 (Gill 1980; c.f. Fig. 1a,b), where contours in the top (bottom) panel depict vertical velocity (perturbation pressure) and vectors in each panel represent the velocity field for the lower layer. The results indicate that upward motion occurs in the region of heating (top panel), with two cyclones forming on the northwest and southwest flanks of the forcing region (bottom panel). The results in the bottom panel of Fig. 1.1 also reveal that easterlies (westerlies) form to the east (west) of the heat source and are associated with that of an eastward-propagating Kelvin wave (westward-propagating Rossby waves). Hence, the solutions to the simple shallow water model in Gill (1980) suggest that elevated (or free tropospheric) heating associated with the condensation of water vapor in cumulus convection acts to perturb the tropical surface pressure field, thus influencing surface winds and the consequent low-level patterns of convergence.

In contrast, Lindzen and Nigam (1987) proposed that it is the gradients in SST, rather than cumulus heating in the free troposphere, that influence patterns of low-level convergence in the surface wind field. While latent heating is large in the Tropics, it is argued that small horizontal gradients in the tropical SST field (such as those mentioned earlier over the equatorial eastern Pacific and tropical Atlantic) are capable of influencing the boundary layer temperature distribution and (consequently) the near-surface pressure field (e.g., Lindzen and Nigam 1987; Chiang et al. 2001; Back and Bretherton 2009). Using a simple modified linear model analogous to that of Gill (1980), Lindzen and Nigam (1987) found that a key relationship between SST gradients and the surface winds is a dependence of the eddy sea level pressure field on the surface temperature distribution. In this framework, as differential heating occurs between the sea surface and boundary layer, the boundary layer temperatures are modified similar to that of the underlying SST gradients, resulting in the formation of an anomalous surface low (high) pressure over relatively warm (cold) tropical SSTs. Hence, the results suggest that zonal and meridional gradients in the tropical SST field can directly determine the patterns of low-level convergence in the surface wind field, which in turn can influence the location and intensity of tropical precipitation.

As inferred from the above frameworks, the dominant process that influences the distribution of tropical surface winds is dependent on the background environment and location across the Tropics. For example, studies have found that while elevated heating generates the bulk of zonal wind forcing in the Tropics (as well as meridional wind in the subtropics), surface forcing is the dominant contributor to the meridional wind and near-surface convergence response in regions of strong boundary layer temperature gradients near the equator and trade cumulus inversion (where meridional SST gradients are largest) (e.g., Chiang et al. 2001; Back and Bretherton 2009). Thus, the climatological-mean tropical atmospheric response to diabatic heating can be understood as a combination of the following: 1) deep convective heating forces free-tropospheric pressure gradients and downward momentum mixing that largely determine the surface zonal wind throughout the Tropics, and 2) in regions of tropical SST gradients, asymmetric heating of the tropical atmospheric boundary layer can induce near-surface pressure gradients that directly force the meridional wind field and low-level convergence.

1.1.2 The Transient Atmospheric Response to Diabatic Heating

It is important to consider the transient relationships between the atmosphere and the ocean to fully understand the climatological-mean balance to thermal forcing, especially in applications of numerical weather prediction. To resolve the basic features of the mean tropical circulation, studies have explored the transient evolution of the atmospheric response to a tropical heat source in both observations and numerical models. In particular, analyses have investigated the transient response to a sudden "switch-on" of heating, with a focus on how the atmospheric circulation evolves toward the steady (or climatological-mean) state and how long the adjustment takes.

Heckley and Gill (1984) explore the simple paradigm in Gill (1980), where time-dependent solutions are analyzed for a sudden "switch-on" of heating in the Tropics. As in Fig. 1.1 from Gill (1980), the results in Fig. 1.2 from Heckley and Gill (1984; c.f. Fig. 2) show the analytical horizontal solutions to a set of shallow water equations for a heating that is symmetric about the equator; the response amplitudes are shown at different time steps (T) after the heating is suddenly switched on at T = 0 in both an undamped (left column) and damped (right column) case. In the damped case (which achieves a steady-state due to the inclusion of dissipative processes), an eastward-propagating Kelvin wave front emanates from the forcing region, completely emerging after approximately one day. Ascent occurs in the heating region and descent occurs in the wave front (as indicated by the dashed contours with +/− symbols), with low-level easterlies (and upper-level westerlies) in between. As the Kelvin wave front propagates away from the region of forcing, the area of descent spreads between the heating and the front until it becomes negligible. On the western side of the forcing region, the westward-propagating Rossby wave front emanates from the forcing region at about one third of the speed of the Kelvin wave front, with descending air to the north and south of the equator (e.g., Heckley and Gill 1984). The descent again spreads over the region between the front and the heating until it becomes negligible, leaving behind a steady-state flow that is cyclonic at low levels (and anticyclonic at high levels). The steady-state solution seen in Fig. 1.1 (and shown at T = 40 in Fig. 1.2) is achieved after approximately 10 days, suggesting a rapid adjustment of the tropical atmospheric circulation to diabatic heating.

The influence of the fast-moving, eastward-propagating Kelvin wave front found in Heckley and Gill (1980) has important implications for interannual and intraseasonal variability in the Tropics. Studies have shown that efficient and fast warming of the entire upper tropical troposphere in response to enhanced precipitation associated with the Madden-Julian Oscillation (MJO; i.e., the dominant mode of tropical intraseasonal variability) is consistent with the notion of a Kelvin wave front, where the wave front acts to redistribute latent heat release in regional convective systems over the tropical belt (e.g., Madden and Julian 1994; Bantzer and Wallace 1996; Maloney and Sobel 2007). Similar results have been found with respect to the remote tropical response to a sudden onset of El Niño conditions, in that a fast (~10 day) atmospheric adjustment to anomalously warm tropical SSTs is dominated by moist Kelvin-like wave propagation (e.g., Chiang and Sobel 2002; Lintner and Chiang 2006). This suggests that the transient relationships between the ocean and atmosphere in the Tropics play an important role in maintaining the observed degree of spatial homogeneity in the tropical temperature field on different time scales.

1.1.3 Remote Teleconnections to the Extratropics

In addition to forcing the tropical atmospheric response, an anomalous heat source in the Tropics is capable of perturbing the large-scale midlatitude circulation through remote teleconnections (or connections at widely separated points on the globe) via atmospheric Rossby wave trains (e.g., Hoskins and Karoly 1981; Horel and Wallace 1981; Alexander et al. 2002). Figure 1.3 illustrates the theoretical barotropic Rossby wave rays and phases for different zonal wavenumbers obtained by Hoskins and Karoly (1981; c.f. Fig. 12a) in response to a tropical heat source centered at 15°; the results represent the steady-state solutions of the linearized nondivergent barotropic vorticity equation on a sphere in the absence of dissipative processes. The two key features shown in Fig. 1.3 are as follows: 1) the phases (marked by crosses) on each ray indicate alternating positive and negative vorticity centers of action along the wave train and 2) the rays (denoted by lines) that connect the centers are directed first poleward, then curve eastward, and finally equatorward along a circular path. Note that the role of dissipation (not shown) in the solutions is to absorb the waves at the critical line, or turning point of the waves, which prevents propagation back to the source region.

The theoretical, steady-state linear response to thermal forcing presented in Hoskins and Karoly (1981) is consistent with the observed atmospheric teleconnection patterns associated with the warm phase of the El Niño Southern Oscillation (ENSO), or the leading mode of climate variability on interannual to decadal time scales (eg., Walker and Bliss 1932; Horel and Wallace 1981; Wright et al. 1988). Figure 1.4 provides a schematic illustration from Horel and Wallace (1981; c.f. Fig. 11) of the hypothetical atmospheric response to warm SST anomalies in the tropical Pacific, which has a strong qualitative resemblance to the analytical solutions shown in Fig. 1.3. Remote teleconnections associated with ENSO are best understood via the "atmospheric bridge", or the idea that the atmospheric response (i.e., the excitation of Rossby wave trains) to SST anomalies in the equatorial Pacific remotely influences ocean conditions in regions across the globe (e.g., Alexander et al. 2002).

1.2 Midlatitude Air-Sea Interaction

As reviewed in the previous section, the atmospheric response to *tropical* SST anomalies is robust in both models and observations, and the physical processes governing tropical air-sea interactions are generally well-understood. In contrast, the atmospheric response to *midlatitude* SST anomalies is relatively subtle and difficult to detect, particularly in observations. That is because in the midlatitudes, air-sea interaction is dominated by atmosphere-to-ocean forcing (e.g., Davis 1976, 1978; Deser and Timlin 1997; Ciasto and Thompson 2004), and the influence of the ocean on the atmosphere is small in comparison to internal atmospheric variability (e.g., Palmer and Sun 1985; Barsugli and Battisti 1998; Kushnir et al. 2002). However, given advancements in the resolution of satellite observations and numerical models over the past decade, there is a growing body of evidence that suggests the midlatitude ocean has a more important influence on the atmospheric circulation than previously thought. This section reviews fundamental features of the midlatitude ocean and atmospheric circulation and explores recent developments on the current understanding of midlatitude ocean-atmosphere interaction.

1.2.1 Dominant Patterns of Extratropical Climate Variability

This section briefly reviews the leading structures of extratropical climate variability on interannual time scales. Patterns of midlatitude atmospheric variability can be thought of as teleconnections to internal atmospheric dynamics, where variations in the quasi-stationary planetary waves produce spatially coherent large-scale red-noise patterns of climate anomalies (such as geopotential height, temperature, and zonal wind) that occur on monthly or seasonal time scales (e.g., Wallace and Gutzler 1980; Hurrell 1995; Quadrelli and Wallace 2004). The most prominent and recurrent (or leading) modes of interannual atmospheric variability in the Northern and Southern Hemispheres (NH and SH, respectively) are the annular modes, or hemispheric scale, zonally-symmetric equivalent barotropic patterns characterized by pressure anomalies of opposite sign between polar and middle latitudes associated with meridional shifts in the midlatitude westerlies (e.g., Kidson 1988; Thompson and Wallace 1998, 2000; Limpasuvan and Hartmann 1999).

The Northern Annular Mode (NAM) in the NH is calculated as the leading Empirical Orthogonal Function (EOF) of NH monthly-mean sea level pressure, where the positive phase is defined by anomalously low (high) pressure in polar (middle) latitudes, as depicted in Fig. 1.5 (top left). The anomalies associated with the NAM are maintained by feedback forcing from anomalous synoptic-scale eddy and planetary wave activity (e.g., Lorenz and Hartmann 2003). The top right panel of Fig. 1.5 shows the positive phase of the Southern Annular Mode (SAM), or the Southern Hemisphere counterpart to the NAM, also calculated here as the leading EOF of monthly-mean sea level pressure over the SH (e.g., Kidson 1988;

Thompson and Wallace 2000). Note that, given the higher degree of zonal symmetry in the SH, the SAM is more commonly defined as a zonal index based on the zonal-mean zonal wind (e.g., Lorenz and Hartmann 2001). Anomalies associated with the SAM are primarily maintained through a positive feedback between the zonal-mean wind anomalies and the eddy momentum fluxes (e.g., Lorenz and Hartmann 2001). The annular modes exist year round and explain ~20 - 30% of the total variance in the geopotential height and wind fields of their respective hemispheres, with fluctuations in the variance explained depending on season (e.g., Thompson and Wallace 2000).

Regionally dominant patterns of wintertime atmospheric variability in the Northern Hemisphere consist of the North Atlantic Oscillation (NAO) and the Pacific-North American Pattern (PNA) (e.g., Wallace and Gutzler 1980; Hurrell 1995; Thompson and Wallace 1998; Wallace and Thompson 2002; Quadrelli and Wallace 2004). The NAO is similar to the NAM in that both patterns are related to the leading EOF of sea level pressure anomalies in the Northern Hemisphere; however, the NAO primarily emphasizes the north-south dipole structure between the North Atlantic sector and the polar region (not shown), with little relation to the Pacific sector (e.g., Hurrel 1995; Wallace and Thompson 2002). The PNA pattern is the key source of interannual atmospheric variability over the Pacific sector and is defined as the second EOF (or second leading mode) of monthly-mean wintertime SLP anomalies over the Northern Hemisphere (e.g., Quadrelli and Wallace 2004). The positive phase of the PNA pattern is characterized by above-average 500-hPa geopotential heights (Z_{500}) over North America and below average Z_{500} heights south of the Aleutian Islands and over the southeastern United States, as depicted in the bottom panel of Fig. 1.5.

1.2.2 Western Boundary Currents and Sea Surface Temperature Fronts

Increasingly high-resolution satellite observations reveal that the climatological-mean near-surface wind field is strongly influenced by large horizontal gradients in the midlatitude

SST field, such as those associated with the major western boundary currents (e.g., O'Neill et al. 2003; Nonaka and Xie 2003; Chelton et al. 2004; Chelton and Xie 2010). Western boundary currents (WBC) are strong poleward flowing currents along the western sides of the wind-driven subtropical ocean gyres off the eastern coast of continents that transport heat from the tropics to higher latitudes. The two main WBCs in the Northern Hemisphere are the Kuroshio Current in the North Pacific Ocean and the Gulf Stream Current in the North Atlantic Ocean. The Oyashio Current is also a WBC in the North Pacific, except that it flows equatorward and advects subarctic SST to the midlatitudes where it joins the Kuroshio current. The counterparts in the Southern Hemisphere are the Brazil-Malvinas Current in the South Atlantic, East Australia Current in the South Pacific, and Agulhas Current in the South Indian Ocean. The eastward meanders (or extensions) of these currents are characterized by tight north-south gradients in the SST field, with relatively warmer water toward the equator and relatively colder water toward the pole.

Similar to the surface wind response to tropical SST gradients (e.g., Lindzen and Nigam 1987), observations of wind stress curl and divergence from the QuikSCAT satellite radar scatterometer (e.g., Chelton et al. 2001) indicate that surface air blowing across an ocean front accelerates the surface flow, leading to patterns of convergence and divergence in the atmospheric boundary layer (e.g., O'Neill et al. 2003; Nonaka and Xie 2003; Chelton et al. 2004; Chelton and Xie 2010). It is argued that in addition to the pressure adjustment mechanism, the cross-frontal air flow leads to stability driven wind mixing, such that destabilization in the boundary layer increases mixing and brings higher momentum air to the surface (e.g., Small et al. 2008; Kilpatrick et al. 2016; Schneider and Qiu 2015). Observational and numerical studies have also shown that climatological-mean SST gradients in the midlatitudes are capable of forcing vertical motion (i.e., through changes in the near-surface wind field) well into the free troposphere (e.g., Minobe et al. 2008, 2010). As noted for the tropical ocean in Section 1.1.3, the extent to which the midlatitude ocean perturbs the free troposphere can have important implications for the large-scale atmospheric circulation. Indeed, studies suggest that climatological-mean midlatitude SST fronts play an important role in determining the strength and position of the extratropical storm tracks and the eddy-driven jet (e.g., Nakamura et al. 2004, 2008; Sampe et al 2010; Small et al. 2014; Piazza et al. 2016; Shaw et al. 2016).

In general, storm tracks are regions of baroclinic instability off the east coast of continents within which extratropical cyclones tend to generate, transporting energy poleward to reduce the energy imbalance due to differential solar heating between the Equator and the pole (e.g., Hoskins and Valdes 1990; Trenberth and Stepaniak 2003; Shaw et al. 2016). Midlatitude surface temperature gradients are a key source of baroclinicity-forming processes in the midlatitudes, where cross-frontal differential heat supply from the ocean maintains a region of near-surface baroclinic instability that in turn organizes a storm track (e.g., Nakamura et al. 2004, 2008; Brayshaw et al. 2008; Sampe et al. 2010). This process, known as an "oceanic baroclinic adjustment" (e.g., Nakamura et al. 2004, 2008), is hypothesized as follows: poleward eddy heat fluxes act to relax the surface air temperature (SAT) gradient (driven by sharp gradients in the SST front), yielding greater SST−SAT differences at the air-sea interface that give rise to enhanced and reduced surface sensible heat fluxes on the equatorward and poleward flanks of the SST front, respectively; the enhanced differential heat supply then restores the near-surface baroclinicity, thus anchoring the storm track. Importantly, studies suggest that the influence of oceanic frontal zones on the eddy-driven jet (i.e., strong surface westerlies collocated with the storm track) may have a significant impact on the leading modes of midlatitude atmospheric variability (e.g., Nakamura et al. 2008; Ogawa et al. 2016; O'Reilly et al. 2017; Seo et al. 2017).

1.2.3 Variations in Midlatitude Sea Surface Temperatures and the Atmospheric Circulation

A growing body of research suggests that *temporal variations* in midlatitude SSTs can also have a significant impact on the atmospheric circulation on a variety of time scales.

While the atmosphere serves as the primary driver of SST anomalies over the extratropical ocean basins (e.g., Deser and Timlin 1997; Kushnir et al. 2002), the largest variations in midlatitude SSTs occur in regions of strong horizontal temperature gradients (e.g., Nakamura et al. 1997; Nonaka and Xie 2003; Ciasto and Thompson 2004; Deser et al. 2010; Smirnov et al. 2014), such as those associated with the major western boundary currents, where variations can also arise from forcing by the ocean circulation itself (e.g., Frankignoul and Reynolds 1983; Smirnov et al. 2014).

Observational and numerical studies have shown that meridional shifts (associated with SST anomalies) in the locations of the Kuroshio-Oyashio Extension and Gulf Stream Extension fronts are significantly linked to variations in the large-scale atmospheric circulation on intraseasonal, interannual, and decadal time scales (e.g., Frankignoul et al. 2011; Czaja and Blunt 2011; Taguchi et al. 2012; Sheldon and Czaja 2014; Smirnov et al. 2015; Wills et al. (2016); Révelard et al. 2016; Seo et al. 2017). For example, Révelard et al. (2016) found a coherent response to decadal fluctuations in the Kuroshio Extension during the cold season in observational analyses of ERA-Interim during the 1979 - 2012 time period; the hemispheric scale atmospheric response consists of an equivalent barotropic high downstream of the Kuroshio Extension (and a weak high over the western United States), and an equivalent barotropic low over the Arctic. Taguchi et al. (2012) argued that SST anomalies in the subarctic frontal zone (associated with the Oyashio Extension) precede the development of an anomalous circulation pattern reminiscent of the PNA pattern, while an observational study by Frankignoul et al. (2011) indicated that a northward shift in the Oyashio Extension front precedes the development of circulation anomalies reminiscent of the North Pacific Oscillation.

In the North Atlantic, Seo et al. (2017) investigated the extratropical atmospheric response to meridional shifts in Gulf Stream position and found a dominant nonlinear response pattern that resembled the negative phase of the NAO. In a numerical experiment by Smirnov et al. (2015), results from a high-resolution atmospheric general circulation model suggested that positive SST anomalies over the Kuroshio-Oyashio Extension lead changes in upward vertical motion by several weeks, consistent with studies that have linked anomalously warm SSTs in the Gulf Stream region to vertical motion in the warm sector of extratropical storms (e.g., Czaja and Blunt 2011; Sheldon and Czaja 2014). Similarly, Wills et al. (2016) identified a significant transient pattern of circulation anomalies that lags SST anomalies in the Gulf Stream Extension by several weeks, consisting of an anomalous low pressure anomaly over the Gulf Stream region and a high pressure anomaly south of Iceland. Aside from the western boundary currents, an idealized numerical experiment by Ogawa et al. (2016) indicated that characteristics of the SAM exhibit strong sensitivity to the position of a SST front situated at middle and subpolar latitudes in the Southern Hemisphere.

In addition to variations in the latitudinal locations of midlatitude SST fronts, variations in the *gradients* of midlatitude SSTs are capable of influencing the amplitudes and locations of the storm tracks (e.g., Brayshaw et al. 2008; Nakamura and Yamane 2010; Deremble et al. 2012; Michel and Riviére 2014; O'Reilly and Czaja 2015; Parfitt et al. 2016; O'Reilly et al. 2017). Brayshaw et al. (2008) concluded that the structures of SST gradient anomalies yield a greater influence on the atmospheric response than the midlatitude SST anomaly itself. For example, a warm SST anomaly modifies the background temperature distribution such that the SST gradient is enhanced on the poleward side of the SST anomaly (increasing the baroclinicity) and reduced on the equatorward side of the SST anomaly (decreasing the baroclinicity), leading to a stronger storm track poleward of the warm SST anomaly (e.g., Brayshaw et al. 2008). In an observational study by Nakamura and Yamane (2010), the leading EOFs of anomalous near-surface baroclinicity in the North Pacific basin revealed patterns of shifts and changes in the strength of the near-surface baroclinicity that were accompanied by large SST anomalies in the Kuroshio-Oyashio Extension during midsummer. O'Reilly and Czaja (2015) also found observational evidence suggesting that when the Kuroshio Extension is less meandering (i.e., the current is narrower and stronger), the strengthened SST gradient enhances the low-level baroclinicity and localizes the North Pacific storm track zonally and more effectively over the western Pacific.

Similarly, a study by O'Reilly et al. (2017) found that stronger SST gradients in the Gulf Stream generate stronger meridional eddy heat fluxes in the lower troposphere and are associated with northward shifts in the North Atlantic eddy-driven jet. In numerical experiments on eddy-driven jet variability, Michel and Riviére (2014) showed that a more intense, a wider, or a more equatorward SST front leads to a strengthening in the low-level baroclinicity, storm track, and eddy-driven jet. They also argue that the systematic poleward displacement of the eddy-driven jet relative to the storm track is due to the predominance of anticyclonic wave-breaking events over cyclonic wave-breaking events with increasing latitude (e.g., Riviére 2009), where anticyclonic wave-breaking induces poleward momentum fluxes on the equatorward side of the jet. In contrast, Deremble et al. (2012) suggest that moist processes are in part responsible for the poleward displacement of the eddy-driven jet, arguing that the nonlocal nature of water vapor effects leads to increases in temperature at higher latitudes, thus displacing the jet poleward due to thermal wind balance. A recent numerical study by Parfitt et al. (2016) indicated that on smaller spatial scales inside the storm tracks, variations in midlatitude SST gradients are crucial to the thermal dampening and strengthening of passing atmospheric cold fronts embedded within extratropical cyclones.

1.3 Outline of Dissertation

The ocean is an integral part of the climate system, where its currents are crucial to the transport of heat from the Tropics to the polar regions, and its interactions with the atmospheric circulation have wide-ranging impacts on the large-scale and local patterns of climate and weather variability across the globe. As summarized in this chapter, past studies have demonstrated that: 1) the tropical ocean is a strong driver of atmospheric variability both locally and remotely, where anomalous warming is largely balanced by surface convergence processes due to elevated heating and surface temperature gradients, which in turn induce rising motion that can incite Rossby wave trains and lead to remote teleconnections; and 2) there is clear evidence that climatological-mean variations in the midlatitude ocean (especially midlatitude SST gradients) influence the relative strength and position of the atmospheric storm tracks and eddy-driven jets, while a growing body of evidence suggests subseasonal variations in the midlatitude SST field can influence the free tropospheric circulation and impact the leading modes of midlatitude atmospheric variability.

The aim of this dissertation is to provide new insights into the role of the ocean in climate by 1) presenting new observational analyses on the relationships between midlatitude SST anomalies and the atmospheric circulation on subseasonal time scales and 2) providing a new, simplistic framework for understanding how the atmosphere responds to a one-way forcing of heat from the ocean surface at different locations across the globe in an idealized global climate model. Chapter 2 provides a description of the data and methods used to perform both the observational and numerical analyses. Chapter 3 is based on previously published material from Wills et al. (2016) and Wills and Thompson (2018) and explores the observed relationships between variations in North Pacific SSTs in the Kuroshio-Oyashio Extension and the overlying atmospheric circulation on daily-mean timescales, in addition to some key comparisons with results over the North Atlantic. Motivated by the results in Chapter 3, the numerical analyses in Chapter 4 attempt to isolate the role of the ocean using an atmosphere-only model with an idealized aquaplanet configuration to explore the atmospheric response to a prescribed ‘realistic’ SST anomaly at varying latitudes across the globe. Chapter 5 provides a summary and discussion of the key results from the dissertation and outline topics of future research.

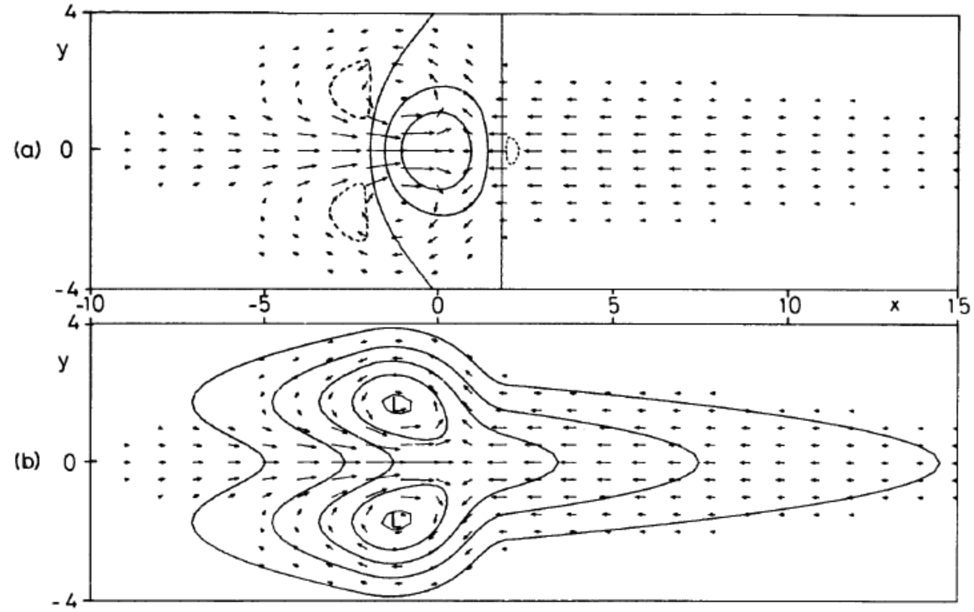

Figure 1.1. From Gill (1980). Matsuno-Gill model solutions for elevated heating symmetric about the equator. (Top) Contours of vertical velocity w (solid contours are 0, 0.3, 0.6, broken contour is -0.1) superimposed on the velocity field for the lower layer. (Bottom) Contours of perturbation pressure p (contour interval 0.3), which is everywhere negative, superimposed on the velocity field.

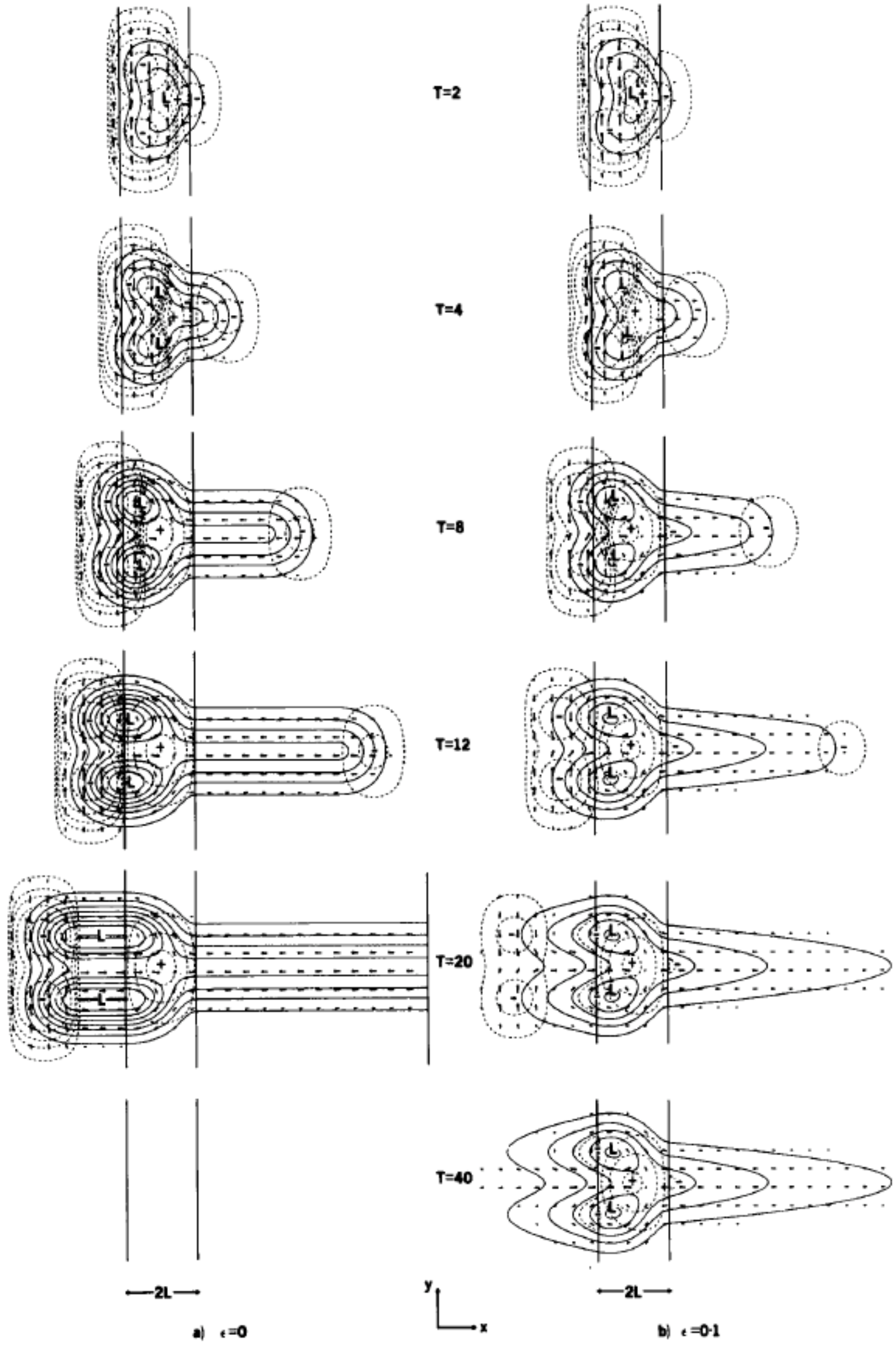

Figure 1.2. From Heckley and Gill (1984). Total response amplitude as a function of x, y at specific times to heating symmetric about the equator localized in the region $|x| < 2|$ suddenly switched on at $t = 0$. Solid lines are pressure perturbation, p, contour interval 0.3. Dashed lines vertical velocity w, contour levels ± 0.1; $\pm 2^n/10$ ($n \geqslant 2$). The horizontal arrows are in the direction of the horizontal velocity, v, the lengths of the arrows proportional to the logaritm of $|v| = (u^2 + v^2)^{\frac{1}{2}}$. + indicates ascent, −, descent. (a) The undamped case ($\epsilon = 0$). (b) The damped case ($\epsilon = 0.1$).

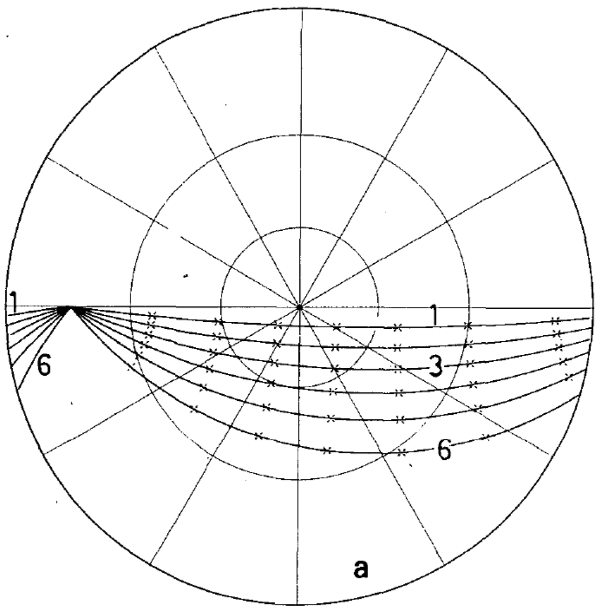

Figure 1.3. From Hoskins and Karoly (1981). Rays and phases marked by a cross every 180° for a source at 15° in a super-rotation flow. If all wavelengths give a negative extremum at the source, the crosses mark the positions of successive positive and negative extrema. Lines of latitude and longitude are drawn every 30° and the zonal wavenumbers associated with the rays are indicated.

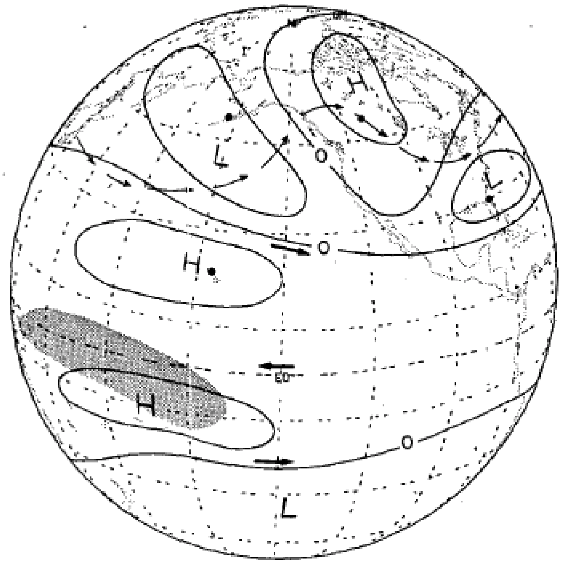

Figure 1.4. From Horel and Wallace (1981). Schematic illustration of the hypothesized global pattern of middle and upper tropospheric geopotential height anomalies (solid lines) during a Northern Hemisphere winter which falls within an episode of warm sea surface temperatures in the equatorial Pacific. The arrows in darker type reflect the strengthening of the subtropical jets in both hemispheres along with stronger easterlies near the equator during warm episodes. The arrows in lighter type depict a mid-tropospheric streamline as distorted by the anomaly pattern, with pronounced "troughing" over the central Pacific and "ridging" over western Canada. Shading indicates regions of enhanced cirriform cloudiness and rainfall.

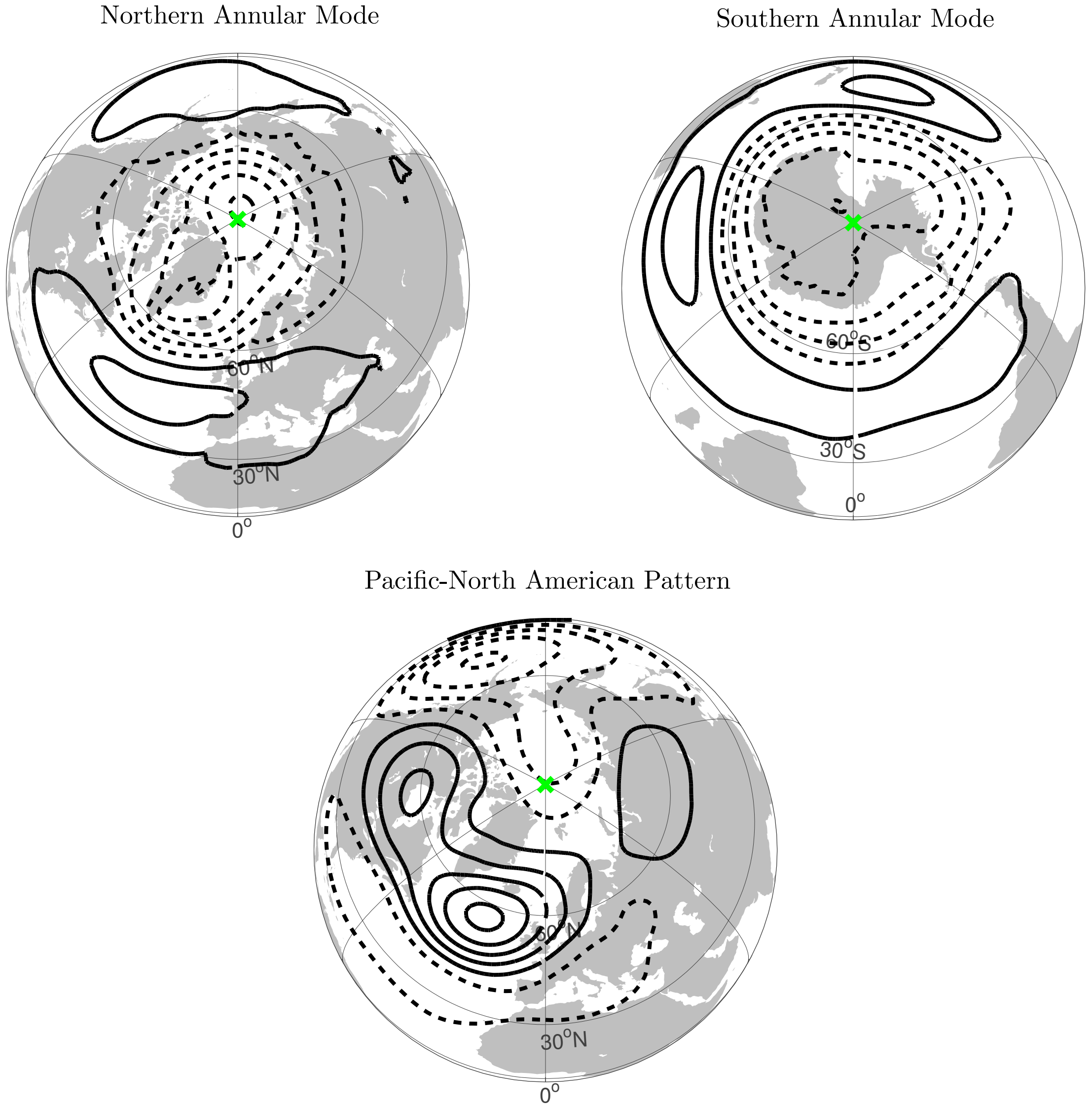

Figure 1.5. (top row) Annual regressions of monthly-mean Z_{1000} on the standardized (left) NAM and (right) SAM indices in the Northern and Southern Hemisphere, respectively. (bottom) Wintertime regression of monthly-mean Z_{500} on the standardized PNA index in the Northern Hemisphere. The regressions are based on ERA-Interim output from 1979 - 2013. Z_{1000} contours are spaced at intervals of 10 meters (-15, -5, 5, 15...m) and Z_{500} contours are spaced at intervals of 15 meters (-22.5, -7.5, 7.5, 22.5...m). The green X denotes the location of the pole.

CHAPTER 2: DATA AND METHODS

2.1 Data

2.1.1 ECMWF ERA-Interim Reanalyses

The European Center for Medium Range Weather Forecasts (ECMWF) Interim Reanalyses product is used to perform the observational analyses described in Ch. 3 of this dissertation. The dataset comprises of global atmospheric reanalyses available from January 1, 1979 - present and provides output on a variety of temporal (3-hourly - monthly) and spatial (1/8° - 3°) scales across the globe (e.g., Dee et al. 2011; http://apps.ecmwf.int/datasets/data/intertim-full-daily/levtype=sfc/). The analyses in Ch. 3 focus on daily-mean output examined on a 1.5°-resolution grid over the 35-yr period 1979 - 2013.

The key variables obtained from ERA-Interim include SST, potential temperature (θ), wind (v), surface turbulent heat flux (THFLX; sensible + latent heat flux), and geopotential height (Z). To remove the influence of trends on the results, the data were detrended by removing the linear fit from the daily-mean time series at each grid point. Anomalies for each field were calculated by removing the long-term mean seasonal cycle from the data at all grid points, where the long-term mean seasonal cycle is found by averaging all 35 years of the data record as a function of calendar day. Note that THFLX anomalies are positive downward (i.e., positive THFLX anomalies are directed from the atmosphere into the ocean).

2.1.2 NCAR Community Atmosphere Model, Version 5.3

The numerical analyses performed in Ch. 4 of this dissertation are based on a new aquaplanet configuration of the Community Atmosphere Model, Version 5.3 (CAM5.3), global climate model, the atmospheric component of the Community Earth System Model (CESM), Version 1.2.2, released in June 2014 (e.g., Medeiros et al. 2016). By definition, an aquaplanet is an idealized configuration in which a planet's surface is completely covered by water (i.e., features such as topography, land, and sea ice are absent), allowing for the removal of complexities from the climate system such as land-sea contrasts, land-atmosphere interactions, orography effects, asymmetric SST distributions, etc. (e.g., Neale and Hoskins 2000a,b; Williamson et al. 2013). With the aquaplanet configuration, the full CAM parameterization suite can be run above a prescribed, zonally-symmetric surface temperature distribution that varies only in latitude (e.g., Medeiros et al. 2016).

The Community Atmosphere Model, Version 5, uses a finite volume dynamical core (as in the older CAM4 version) and contains 30 vertical levels defined on a hybrid pressure-sigma coordinate system (e.g., Neale et al. 2010). For the CAM5.3 aquaplanet configuration, orbital parameters are set for perpetual equinox conditions, and effects due to aerosols are removed by setting aerosol emissions to zero and specifying constant cloud droplet and crystal number concentrations (see Medeiros et al. (2016) for further details). The numerical simulations performed here are run on the model's nominal 1° (0.9° x 1.25°) horizontal grid resolution, and model output is saved at 6-hour, 24-hour, and 30-day time intervals.

2.2 Methods

2.2.1 Observational Analyses

This section details the statistical techniques used to perform the observational analyses presented in Ch. 3, which explore the observed intraseasonal relationships between SST anomalies within western boundary currents and the overlying atmospheric circulation. A primary focus is placed on SST variability in the Kuroshio-Oyashio Extension in the North Pacific (e.g., Wills and Thompson 2018), and additional comparisons are made to SST variability in the Gulf Stream Extension in the North Atlantic (e.g., Wills et al. 2016).

2.2.1.1 Definition of SST Indices

Time series of daily-mean SST anomalies are created to capture the wintertime (December - February) SST variability associated with the Kuroshio-Oyashio and Gulf Stream Extension regions. The SST index for the Kuroshio-Oyashio Extension (hereinafter K_{SST}) is averaged over all grid points in the region 36° - 42°N, 140° - 171°E, and the SST index for the Gulf Stream Extension (hereinafter G_{SST}) is averaged over all grid points in the region 37.5° - 45°N, 72° - 42°W. The averages over each region are cosine-weighted to account for the decrease in area towards the poles. It should be noted that the results are not sensitive to the specific domains used to define the Kuroshio-Oyashio and Gulf Stream Extension regions. Each index is standardized so that is has a mean of zero and standard deviation of one, where positive values of the index correspond to positive SST anomalies in each region, and vice versa.

2.2.1.2 Linear Regression

Linear regression models a dependent variable (or predictand) y in terms of an independent variable (or predictor) x as a linear least-squares fit of the form

$$\hat{y} = a_1 x + a_o \tag{2.1}$$

where $\hat{y}$ is an estimate of y based on a linear relationship with x. The coefficient a_1 (i.e., the regression coefficient) represents the slope of the straight line curve between $\hat{y}$ and x, and the constant a_o represents the y-intercept. Per a linear least-squares fit, the values of a_o and a_1 are chosen to minimize the sum of the squared differences between y and $\hat{y}$, and the formulas for a_1 and a_o are calculated as:

$$a_1 = \frac{\overline{x'y'}}{\overline{x'^2}} \tag{2.2}$$

$$a_o = \bar{y} - a_1 \bar{x} \tag{2.3}$$

Overbars ($^{-}$) denote means and primes ($'$) denote departures from the mean. Based on Eq. 2.2, the regression coefficient a_1 is equal to the covariance between x and y divided by the variance of x. The regression maps presented in the observational analyses in Ch. 3 are plotted in terms of the regression coefficient, thus highlighting the amplitude of the linear relationship between the predictand (i.e., the atmospheric variables) and the predictor (i.e., the SST indices) at each grid point.

2.2.1.3 Correlation and Significance Testing

To determine the robustness of the relationship between x and y based on linear regression analysis, it is important to understand what fraction of variance is explained by the linear fit (or the regression coefficient). A correlation coefficient r can be calculated to provide a quantitative indication of the spread in the real data about the best fit line, where the squared correlation coefficient r^2 is equal to the fraction of variance explained by a linear least-squares fit between x and y. The correlation coefficient is calculated as

$$r = \frac{\overline{x'y'}}{\sigma_x \sigma_y} \tag{2.4}$$

or the covariance between x and y divided by the product of the standard deviations of x and y (σ_x and σ_y, respectively). The correlation coefficient is then applied to a Student's *t* test to assess the statistical significance of the patterns in the regression map.

A Student's *t*-statistic of the form

$$t = \frac{r\sqrt{N^* - 2}}{1 - r^2} \tag{2.5}$$

is calculated to test whether or not the linear correlation coefficient r between two time series x and y is statistically different from zero at each grid point. The *t*-statistic is evaluated at the 95% confidence level for a two-tailed Student's *t* test, as it is not known *a priori* if the correlation coefficient will have a positive or negative value. The constant N^* represents an estimate of the independent samples from the data and is calculated per Eq. (31) from Bretherton et al. (1999) of the form

$$N^*_{xy} = N\frac{1 - r_x r_y}{1 + r_x r_y} \tag{2.6}$$

where N is the total sample size of the data and r_x/r_y are the lag-1 autocorrelations of time series x/y, respectively. The purpose of the effective sample size N^* is to account for persistence in the data which can erroneously inflate the statistical significance.

2.2.2 Model Experiments

This section describes the experimental design and statistical techniques used to perform the numerical analyses presented in Ch. 4, which explore the steady-state and transient atmospheric circulation responses to prescribed SST anomalies in an idealized global climate model.

2.2.2.1 Experimental Design and Definitions

A series of numerical simulations were performed on the NCAR CAM5.3 global climate model to test the atmospheric response to an imposed surface thermal forcing prescribed at different latitudes on an idealized aquaplanet (or a completely water-covered planet) under perpetual equinox conditions. Two sets of fixed-SST experiments were designed to test the 1) steady-state and 2) transient evolution of the atmospheric circulation response. Each set consists of five zonally- and hemispherically-asymmetric perturbation experiments where a 1 Kelvin SST anomaly is imposed on the background SST field in the model's northern hemisphere at the centers of the following latitudes: 0°, 20°N, 45°N, 60°N, and 90°N. In addition to the two sets of experiments, a 10,000-day control simulation was conducted in which no SST perturbations are applied to the background SST field; the control simulation serves as a basis of comparison for the perturbation experiments.

The 10,000-day control is prescribed with a fixed, analytical background SST distribution derived from observations. The top left panel of Fig. 2.1 shows the climatological-mean meridional distribution of zonally-averaged 2-meter temperature (T_{2m}) across the Northern and Southern Hemispheres during average equinoctial conditions; the top right panel shows T_{2m} for the Northern Hemisphere only, mirrored across the equator. The red lines indicate observations of T_{2m} based on ERA-Interim reanalyses from 1979 - 2013 averaged over the March - May and September - November seasons. The black lines indicate the solution to the analytical function that best fits the equinoctial T_{2m} observations and is of the form

$$\mathrm{SST}(\theta) = 27 \cos\left(\frac{3}{2}\theta\right) \tag{2.7}$$

where θ represents latitude and the maximum SST is equal to 27°C on the equator. Unlike the commonly used "QOBS" SST distribution (e.g., Neale and Hoskins 2000a), which prescribes SST to be 0°C poleward of 60°, the SST distribution used here extends the zonally-symmetric SST gradient to the pole, as depicted in the bottom panel of Fig. 2.1. Note that SST is plotted in units of Kelvin. While this distribution requires SSTs prescribed below 0°C (or 273 Kelvin) that may introduce complications due to sea ice, extending the SST gradient to the pole provides 1) a better background representation of the observed near-surface temperature (T_{2m}) field and 2) a better context for evaluating the atmospheric circulation response to an anomalous surface heating imposed at higher latitudes (i.e., evaluating the atmospheric response to an SST anomaly in the presence – and not the absence – of background temperature gradients).

For the two sets of zonally- and hemispherically-asymmetric SST perturbation experiments, five different fixed SST anomalies are added to the background SST field as a function of longitude and latitude. The anomaly is defined as a piecewise function similar to the form used for the 1KEQ/3KEQ experiments in Neale and Hoskins (2000a):

$$\mathrm{SST}'(\lambda,\theta)=\begin{cases}\chi\cos^2\left(\frac{\pi}{2}\left[\frac{\lambda-\lambda_o}{\lambda_d}\right]\right)\cos^2\left(\frac{\pi}{2}\left[\frac{\theta-\theta_o}{\theta_d}\right]\right) & :\lambda_o-\lambda_d<\lambda<\lambda_o+\lambda_d\\ & :\theta_o-\theta_d<\theta<\theta_o+\theta_d\\ 0 & :\text{otherwise}\end{cases}\tag{2.8}$$

In Eq. 2.8, SST' is the sea surface temperature anomaly (in units of Kelvin), χ denotes the maximum amplitude of the SST anomaly, λ denotes longitude, θ denotes latitude, λ_o/θ_o are the longitude/latitude of the maximum SST anomaly center, and λ_d/θ_d are the decay (in longitude/latitude) of the SST anomaly from its maximum. As motivated by observed daily-mean SST anomalies over the Gulf Stream and Kuroshio-Oyashio Extension in Ch. 3, in each experiment, $\chi = 1\text{K}$, $\lambda_o = 0°\text{E}$, $\lambda_d = 20°$, and $\theta_d = 10°$, resulting in an elliptical shape of the SST anomaly. However, an exception is made for a SST anomaly centered at the pole, which can only be a function of latitude, resulting in a circular shape. In this case, the SST anomaly is defined as a modified version of Eq. 2.8:

$$\mathrm{SST}'(\lambda,\theta)=\begin{cases}\chi\cos^2\left(\frac{\pi}{2}\left[\frac{\theta-\theta_o}{\theta_d}\right]\right) & :\theta_o-\theta_d<\theta<\theta_o+\theta_d\\ 0 & :\text{otherwise}\end{cases}\tag{2.9}$$

where $\theta_o = 90°$ and the SST anomaly spans all longitudes along a latitude circle. As mentioned earlier, the latitudes of the maximum SST anomaly are defined at $\theta_o = 0°$, 20°N, 45°N, 60°N, and 90°N (denoted as 1KEQ, 1K20N, 1K45N, 1K60N, and 1K90N, respectively).

The two sets of perturbation experiments, hereafter referred to as “steady-state” and “transient”, were conducted as follows. The steady-state experiments consist of five 10,000-day integrations for the 1KEQ, 1K20N, 1K45N, 1K60N, and 1K90N SST perturbations, all initialized from the same atmospheric initial conditions. Initial conditions for CAM5.3 were provided and based on a previous model-simulated state with some adjustments to follow previous aquaplanet configurations (see Williamson et al. (2013) and Medeiros et al. (2016) for additional details). The initial conditions for the steady-state experiments are identical to those used for the control. Thus, the atmospheric response to a prescribed SST anomaly is defined as the difference between the SST perturbation experiment and the control experiment; the steady-state response is calculated as the average 10,000-day difference (with the first 100 days excluded to account for model "spin-up").

The 10,000-day control simulation was also used to perform the transient experiments, which consist of five 100-member ensembles of 100-day integrations for the 1KEQ, 1K20N, 1K45N, 1K60N, and 1K90N SST perturbations. The atmospheric initial conditions are different for each ensemble member and were obtained every 50 days from the start of the control run (with the first set obtained on the 51st day of the control to account for model "spin-up"); the atmospheric conditions used to initialize each ensemble member are identical across the SST perturbation experiments. Again, the atmospheric response is defined as the difference between the perturbation and control experiments; however, the differences are obtained between each "pair" of integrations for days 1 - 100. The ensemble-mean is then calculated by averaging the differences of all 100 pairs on each day of the integrations, and can thus be viewed as the average daily evolution of the atmospheric circulation response to a sudden "switch-on" of anomalous surface heating.

2.2.2.2 Difference of Means and Significance Testing

A "difference of means" test is used to compare two sample means between two sample populations. A Student's *t*-statistic of the form

$$\mathsf{t} = \frac{\bar{\mathsf{x}}_1 - \bar{\mathsf{x}}_2}{\hat{\sigma}\sqrt{\frac{1}{\mathsf{N}_1} + \frac{1}{\mathsf{N}_2}}} \tag{2.10}$$

is calculated to test whether or not the difference between two sample means is statistically different from zero, where $\bar{\mathsf{x}}_1/\bar{\mathsf{x}}_2$ are the sample means from two sample populations (i.e., the perturbation experiment and the control experiment), $\mathsf{N}_1/\mathsf{N}_2$ are the number of independent samples from each sample population, and $\hat{\sigma}^2$ is defined as a weighted average of the sample variances (s_1^2/s_2^2) from each sample population:

$$\hat{\sigma} = \sqrt{\frac{N_1 s_1^2 + N_2 s_2^2}{N_1 + N_2 - 2}} \tag{2.11}$$

The *t*-statistic is evaluated at the 95% confidence level for a two-tailed Student's *t* test, as it is not known *a priori* if the difference between two sample means will be positive or negative. As detailed earlier in Section 2.2.1.3, effective sample sizes N_1^*/N_2^* are calculated per Eq. (31) from Bretherton et al. (1999) to account for persistence in the data.

2.2.2.3 Empirical Orthogonal Function/Principal Component Analysis

Empirical Orthogonal Function (EOF)/Principal Component (PC) analysis is a useful tool for calculating the leading modes of variability in a dataset between two dimensions, such as time and space. EOF's and PC's share a one-to-one relationship, where EOF's represent a set of structures in the spatial (i.e., longitude/latitude grid points) dimension and PC's represent a complementary set of structures in the sampling (i.e., time) dimension.

To calculate EOF1 (or the leading spatial structure that explains the largest fraction of variance) of a data matrix $\mathbf{X}$ with M dimensions in time by N dimensions in space, the data is first detrended and weighted by the square root of the cosine of latitude. The cosine-weighting accounts for the decrease in area towards the pole when calculating the temporal covariance matrix $\mathbf{C}$

$$\mathbf{C} = \frac{1}{M}\mathbf{X}^{T}\mathbf{X} \tag{2.12}$$

where $\mathbf{X}^{T}$ is the transpose of matrix $\mathbf{X}$. The EOF's are obtained by eigenanalyzing the temporal covariance matrix $\mathbf{C}$ as follows:

$$\mathbf{CE} = \mathbf{E\Lambda} \tag{2.13}$$

Here, the eigenvectors $\mathbf{e}_i$ (or EOF's) of the covariance matrix are contained in the columns of matrix $\mathbf{E}$, and the corresponding eigenvalues λ_i (or values related to the variance explained by the eigenvectors) are contained in the diagonal of matrix $\mathbf{\Lambda}$. The eigenvector $\mathbf{e}_1$ associated with the biggest eigenvalue λ_1 is defined as EOF1. The fraction of variance of $\mathbf{X}$ explained by EOF1 is calculated as λ_1 divided by the sum of all eigenvalues. The corresponding principal component time series (PC1) is found by regressing the anomalous data in $\mathbf{X}$ onto EOF1 and explains the temporal evolution of the EOF pattern.

2.2.2.4 Spatial Linear Decomposition

To isolate a specific spatial characteristic embedded in a spatial pattern, it can be useful to apply a spatial linear decomposition in which the pattern is decomposed into two parts: a component that is linearly congruent with the characteristic pattern and a residual component that is linearly unrelated to the characteristic pattern. For example, consider two data matrices $\mathbf{A}$ and $\mathbf{B}$ each consisting of x dimensions in latitude and y dimensions in longitude, where $\mathbf{A}$ represents an arbitrary spatial pattern and $\mathbf{B}$ represents a characteristic pattern. Analogous to the linear least-squares fit relationship in Eq. 2.1, the linear decomposition of $\mathbf{A}$ in terms of $\mathbf{B}$ is defined as

$$\mathbf{A}(x, y) = \alpha\mathbf{B}(x, y) + \mathbf{A}_r(x, y), \tag{2.14}$$

where $\alpha\mathbf{B}$ (or the "embedded" characteristic pattern) represents the component of $\mathbf{A}$ that is linearly congruent with $\mathbf{B}$, and $\mathbf{A}_r$ represents the residual (or "leftover") component of $\mathbf{A}$. The constant α represents the "spatial" regression coefficient and is calculated as a cosine-weighted projection of $\mathbf{A}$ onto $\mathbf{B}$. By construction, the embedded characteristic pattern in $\mathbf{A}$ is constrained to be identical to a unit amplitude of $\mathbf{B}$, where the amplitude is determined by the spatial regression coefficient.

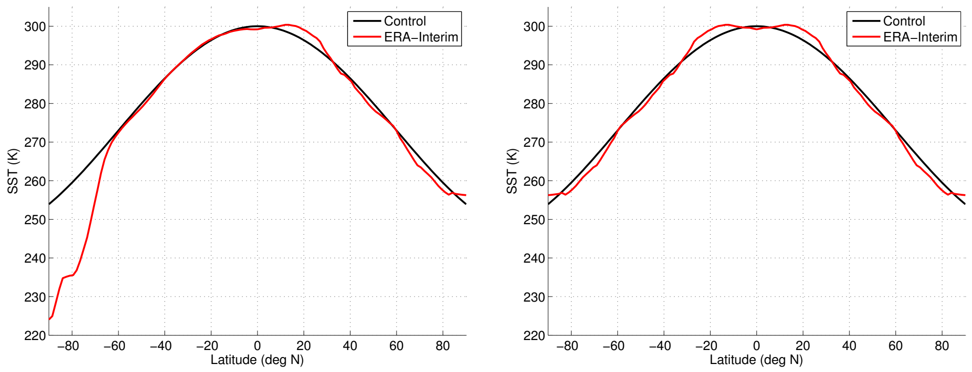
(a) T_{2m} NH and SH

(b) T_{2m} NH (Mirrored)

(c) Control SST Background

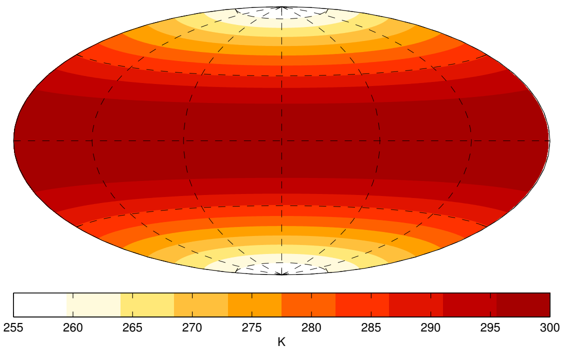

Figure 2.1. (top row) zonal-mean 2-meter temperature (T_{2m}) profiles across the Southern and Northern Hemispheres (panel a, top left) and Northern Hemisphere only (panel b, top right) during average equinoctial conditions for each hemisphere. Red lines indicate T_{2m} observations from the 1979 - 2013 ERA-Interim period, and black lines indicate the analytical function used to create the background SST distribution shown in panel c (bottom).

CHAPTER 3: AN OBSERVATIONAL ANALYSIS OF MIDLATITUDE AIR-SEA INTERACTION OVER THE MAJOR NORTHERN HEMISPHERE WESTERN BOUNDARY CURRENTS[1]

This chapter explores the observational evidence for midlatitude air-sea interaction over the major Northern Hemisphere (NH) western boundary currents using lead/lag regressions based on daily-mean data. This research continues analyses introduced in the Master's Thesis, which explored the varying relationship between the atmospheric circulation and sea surface temperature (SST) anomalies over the North Atlantic sector (e.g., Wills et al. 2016). Here, observational analyses focus on SST anomalies over the Kuroshio-Oyashio Extension region in the North Pacific (e.g., Wills and Thompson 2018), and the observed relationships are compared between the North Atlantic and North Pacific. The results presented in this chapter form the basis of the motivation for the numerical experiments conducted in Ch. 4.

Advancements in the resolution of satellite observations and numerical models over the past decade have provided new evidence that suggests the midlatitude ocean has a more important influence on the atmospheric circulation than previously thought, particularly in regions of large horizontal SST gradients. Previous observational and numerical studies on midlatitude air-sea interaction have shown that the *climatological-mean* SST gradients associated with the major western boundary currents are capable of forcing vertical motion (i.e., through changes in the near-surface wind field) well into the free troposphere (e.g., Minobe et al. 2008, 2010), thus influencing the strength and position of the extratropical storm tracks (e.g., Nakamura et al. 2008; Sampe et al. 2010; Small et al. 2014; Piazza et al. 2016). A growing body of work also suggests that *temporal variations* in midlatitude SSTs can have a significant impact on the atmospheric circulation, where studies have shown that anomalously warm SSTs lead significant changes in upward vertical motion on subseasonal timescales (e.g., Czaja and Blunt 2011;

---

[1] This chapter contains material from Wills et al. (2016) and Wills and Thompson (2018).

Sheldon and Czaja 2014; Smirnov et al. 2015) and variations in midlatitude SST gradients are capable of influencing the amplitudes and locations of the atmospheric storm tracks (e.g., Brayshaw et al. 2008; Nakamura and Yamane 2010; Michel and Rivieré 2014; O'Reilly and Czaja 2015). The goal of this chapter is to reexamine the observational evidence for midlatitude ocean-atmosphere interaction by exploiting daily-mean data, with a focus on SST variations over the Kuroshio-Oyashio western boundary current extension.

The results of this chapter are organized into three main parts. Section 3.1 explores the observed relationships between wintertime variability in Kuroshio-Oyashio Extension (KOE) SSTs and the atmospheric circulation over the North Pacific using lead/lag regressions based on daily-mean data. Section 3.2 presents a key comparison of the KOE results with results based on SST anomalies in the Gulf Stream Extension from Wills et al. (2016). Unlike the Gulf Stream, the extensions of the Kuroshio-Oyashio currents expand into the open ocean and are not as constrained by land barriers. The North Atlantic and Pacific sectors are also subject to different patterns of climate variability, such as the North Atlantic Oscillation in the North Atlantic sector and ENSO and the Pacific-North American pattern in the North Pacific sector. Hence, it is not clear a priori whether the lead-lag relationships between the atmospheric circulation and SSTs in the western boundary current regions will be similar in the two sectors. The linkages between SST anomalies in the Gulf Stream region and the free tropospheric circulation are analyzed in Section 3.3. Conclusions are provided in Section 3.4.

3.1 Kuroshio-Oyashio Extension in the North Pacific Sector

This section details the lead/lag relationships between SST anomalies over the KOE region and the atmospheric circulation during the Northern Hemisphere winter (December - February) season. The observational analyses are based on daily-mean output from the ERA-Interim Reanalyses dataset, as described in Section 2.1.1.

3.1.1 Lead/Lag Regressions based on KOE SST Anomalies

Figure 3.1 provides a brief synopsis of the winter mean circulation and SST field over the North Pacific. Figure 3.1a shows the climatological-mean DJF SST and 850-hPa horizontal wind fields ($\mathbf{u}_{850}$); Fig. 3.1b shows the associated climatological standard deviation of the daily-mean SST anomaly field. Based on the standard deviation of the SST field, it is evident that there are two primary regions of enhanced SST variability in the North Pacific: one to the east of Japan and one in the southeastern North Pacific. Primary focus is placed on the region to the east of Japan (indicated by the box in Fig. 3.1b), which is associated with variability in the KOE (e.g., Nonaka and Xie 2003; Frankignoul et al. 2011; Smirnov et al. 2015), and is where approximately 40%-60% of SST variability is intrinsic to the ocean (i.e., $\sim$ 50% of monthly SST variability in the KOE region is not influenced by variations in surface atmospheric temperature, or atmosphere-to-ocean forcing) (e.g., Smirnov et al. 2014). The second region of large SST variance (centered near 160°W) is linked to the extratropical atmospheric response to ENSO (e.g., Alexander 1992; Cayan 1992; Diaz et al. 2001) and is not the focus of the analyses presented in the current chapter. The potential contamination of the results by ENSO variability is discussed later in this section.

To investigate the statistical covariability between KOE SST anomalies and the anomalous atmospheric circulation, various atmospheric fields are regressed against the $\mathsf{K}_{\mathsf{SST}}$ index, or the standardized time series of daily-mean SST anomalies averaged over the KOE region (i.e., the variance maximum to the east of Japan in Fig. 3.1b). The calculation of the $\mathsf{K}_{\mathsf{SST}}$ index is explained in Section 2.2.1.1. The regressions are performed on daily-mean time scales at lags spanning from -30 to +30 days. By construction, the $\mathsf{K}_{\mathsf{SST}}$ index is always centered within the 90-day period from 1 December to 28 February (i.e., periods highlighted by blue bars in Fig. 3.1c), and negative (positive) lags indicate results where the SST fields being regressed precede (follow) the largest KOE SST anomalies. Hence, at a lag of -30 days (+30 days), the fields being regressed are centered on the 90-day period from 1 November to 29 January (31 December - 30 March). The statistical significance of the sea level pressure (SLP) anomalies at lags of -30 and +30 days is also calculated to assess the robustness of the SLP regression patterns at negative and positive lags (Fig. 3.4), and details of the significance test are provided in the caption.

The lag regressions in the left column of Fig. 3.2 highlight the evolution of the anomalous surface atmospheric circulation associated with SST anomalies in the KOE region on daily-mean time scales. Regression coefficients of SST (shading) and SLP (contours) are shown every 15 days between lags of -30 and +30 days. Note that, throughout this chapter, SLP is expressed as geopotential height at 1000 hPa, or Z_{1000}. As per the definition of the $\mathsf{K}_{\mathsf{SST}}$ index, anomalously warm SSTs peak in amplitude over the KOE region at a lag of zero days, and the results show strong persistence in the anomalous SST field through all lags (consistent with the large heat capacity of the ocean). Based on the regressions at negative lags (i.e., when the fields *precede* the largest KOE SST anomalies), it is evident that the warmest SST anomalies are associated with positive SLP anomalies (which peak in amplitude at a lag of -20 days; not shown) that span much of the North Pacific basin, such that the anomalous surface atmospheric circulation inferred from the top-left panel of Fig. 3.2 acts on the climatological-mean SST gradient (i.e., Fig. 3.1a) to advect anomalously warm air from the east-southeast over the KOE region. As observed for the Gulf Stream in Wills et al. (2016) and documented in previous literature (e.g., Deser and Timlin 1997; Kushnir et al. 2002; Ciasto and Thompson 2004), this result is consistent with atmospheric forcing of the SST field. Lag regressions of surface turbulent heat flux anomalies onto the $\mathsf{K}_{\mathsf{SST}}$ index (Fig. 3.3; shaded) further support this result, as positive (downward) surface turbulent heat flux anomalies at negative lags indicate that the atmosphere is fluxing heat into the ocean prior to the formation of peak SST anomalies.

The results at positive lags in the left column of Fig. 3.2 (i.e., when the fields *follow* the largest KOE SST anomalies) indicate that anomalously warm SSTs are followed by a very different pattern of atmospheric circulation anomalies that peak in amplitude at a lag of +30 days (and damp thereafter; lags greater than +30 are not shown). At positive lag, the circulation anomalies are dominated by low SLP anomalies that overlie and extend downstream of the KOE region. The anomalies also include anomalously high SLP centered (approximately) between Alaska and Kamchatka, but as noted below, the high pressure feature is not statistically significant. Importantly, negative (upward) surface turbulent heat flux anomalies are also found over the KOE region at positive lags (Fig. 3.3), indicating that the ocean is fluxing heat into the overlying atmosphere. This result is consistent with previous findings that suggest a large amount of heat is released to the atmosphere over the Kuroshio-Oyashio confluence region (35° - 40°N, 142° - 150°E) during periods of anomalously warm SSTs (e.g., Sugimoto and Hanawa 2011; Sugimoto 2014).

The associated structures in the 200-hPa geopotential height and $\mathsf{Z}_{200}-\mathsf{Z}_{1000}$ thickness fields (right column of Fig. 3.2) reveal that: 1) the circulation anomalies at negative lag amplify with height and are associated with positive thickness anomalies that extend through the depth of the troposphere and 2) the circulation anomalies at positive lag are associated with much weaker thickness anomalies and are thus relatively confined to lower levels.

The statistical significance of the anomalous circulation patterns at negative and positive lags is shown in Fig. 3.4. As expected from previous analyses based on pentad and weekly-mean SST data (e.g., Deser and Timlin 1997; Ciasto and Thompson 2004), the most significant SLP and Z_{200} anomalies are found at negative lags (top panels in Fig. 3.4), when - as discussed above - the atmospheric circulation anomalies are consistent with forcing of the SST field. At positive lag, the low pressure center of action is most significant at the surface. The weak center of high pressure to the north of the KOE region is not statistically significant at any level.

The temporal and spatial resolutions of SSTs prescribed in ERA-Interim are not consistent throughout the entire 1979 - 2013 time period and this could have an impact on regression analyses based on ERA-Interim SSTs. For example, Masunaga et al. (2015, 2016) found that the location of the near-surface baroclinic zone near the Kuroshio Extension region is highly sensitive to the “low” (1979 - 2001) and “high” (2002 - 2012) resolution periods of ERA-Interim SST, suggesting that long-term changes in the near-surface atmospheric circulation over the western Pacific sector are largely due to improvements in the resolution of SSTs over time. Furthermore, decadal variability in the Pacific decadal oscillation (PDO) can also influence regressions based on data that span the "regime shift" in the PDO ~1998/99 (e.g., Mantua et al. 1997; Newman et al. 2016). To test the influence of these factors on the results, the analyses in Fig. 3.2 were repeated for the 1979 - 95 and 1996 - 2013 time periods (Fig. 3.5, center and right columns, respectively). As evidenced in Fig. 3.5, the primary features found in the full 35-yr record are reproducible in both halves of the data record.

3.1.2 Testing for "Contamination" by ENSO Variability

ENSO has a marked influence on the North Pacific SST field (e.g., Alexander 1992). However, and importantly, it does not contribute to the results shown here. The influence of ENSO was tested as detailed below.

First, ENSO is defined as the standardized low-pass (30 day) filtered time series of daily-mean SST anomalies averaged over the region 6°S - 6°N, 171° - 120°W (i.e., Niño-3.4). Then, the ENSO index is linearly regressed from the wintertime (November - March) SLP time series at each grid point to form the ENSO-residual SLP data. The optimal lag for the regression is determined as follows: 1) the amplitude of the North Pacific SLP pattern associated with ENSO is calculated as a function of lag (not shown) and 2) the time lag is identified when the pattern has maximum amplitude relative to variations in the ENSO index. This lag is used when calculating the linear fit of the gridded SLP data to ENSO at each grid point over the North Pacific sector. The fits were done for the SLP field lagging the ENSO index by 40 days, but the overall results are largely unchanged for lags ranging from 0 to 90 days.

After removing the ENSO time series from the gridded SLP data, the analyses in Fig. 3.2 were repeated using the ENSO-residual SLP data. Importantly, removing ENSO from the SLP data does not change the overall patterns or significance of the results in Fig. 3.2 (results not shown). This is expected, since 1) the correlation between ENSO and the $\mathsf{K_{SST}}$ time series is low ($\mathsf{r} \sim 0.07$ at lag 0), 2) ENSO explains less than ~ 10% of the total variance in North Pacific SLP anomalies on daily time scales (not shown), and 3) ENSO is unlikely to contribute to the day-to-day evolution of the North Pacific SLP field, and thus is unlikely to influence the evolution of the SLP anomalies shown in Fig. 3.2.

3.1.3 Results based on an Atmospheric Index

Analyses based on the $\mathsf{K_{SST}}$ index indicate a significant and distinct pattern of atmospheric circulation anomalies at positive lags (Fig. 3.2), but it is unclear whether this pattern is dependent on SST anomalies within the KOE region. The SLP pattern at positive lags may be “forced” by the underlying SST anomalies. But it may also simply reflect the evolution of the atmospheric circulation anomalies found at negative lags that would occur independent of the SST field. To test against the latter possibility, the analyses in Fig. 3.2 are repeated for regressions based on the expansion coefficient time series of the “atmospheric forcing” pattern (i.e., the pattern of circulation anomalies at negative lags). The atmospheric forcing time series (hereinafter $\mathsf{K_{ATMO}}$) was created by calculating the cosine-weighted average of daily-mean SLP anomalies over the region 39° - 54°N, 150°E - 171°W (i.e., near the center of action of the SLP anomalies in the lag -30 regression map in Fig. 3.2) for all days 1979 - 2013 and then standardizing the resulting index. By construction, the $\mathsf{K_{ATMO}}$ index indicates the temporal evolution of the anomalous atmospheric circulation observed at negative lags (top-left panels of Fig. 3.2) that does not depend on (direct) information from the SST field. To compare against the results based on the $\mathsf{K_{SST}}$ index, the SST and SLP fields are regressed onto $\mathsf{K_{ATMO}}$ at 15-day intervals for lags spanning 0 to +60 days. Hence, lags of 0, +15, +30, +45, and +60 days from the $\mathsf{K_{ATMO}}$ regressions directly correspond to lags of -30, -15, 0, +15, and +30 days from the $\mathsf{K_{SST}}$ regressions, respectively.

The lag regressions of SST and SLP onto $\mathsf{K_{ATMO}}$ are shown in Fig. 3.6. The results indicate that the $\mathsf{K_{ATMO}}$ index projects onto SST anomalies over the KOE region, as expected from results based on the $\mathsf{K_{SST}}$ index (Fig. 3.2). The results also indicate that the SLP anomalies associated with the atmospheric index decay quickly over a time period of a few weeks, in contrast to the persistence of the atmospheric forcing pattern associated with the SST index (Fig. 3.2, left column). The shorter persistence of the atmospheric anomalies in Fig. 3.6 is consistent with the fact that the basis of the regression in Fig. 3.6 ($\mathsf{K_{ATMO}}$) has much more power on daily time scales than the basis of the regression in Fig. 3.2 ($\mathsf{K_{SST}}$). More importantly, the circulation anomalies associated with $\mathsf{K_{ATMO}}$ (Fig. 3.6) do *not* evolve into the pattern of SLP anomalies that lag the $\mathsf{K_{SST}}$ index. Thus, the evolution of the atmospheric forcing pattern appears to be independent of the anomalous atmospheric circulation that forms approximately a month after peak KOE SST anomalies. The results suggest that the pattern of circulation anomalies found at positive lags in Fig. 3.2 derives from information unique to the SST field.

3.2 Comparison with Results based on SST Anomalies in the Gulf Stream Extension

The observational results presented in the previous section indicate that there are two very different and independent patterns of atmospheric circulation anomalies that lead and lag variations in KOE SSTs in the North Pacific on daily-mean time scales. The first pattern, which leads the largest KOE SST anomalies by several weeks, is characterized by statistically significant high pressure anomalies that span much of the North Pacific basin, and is consistent with atmospheric forcing of the ocean - as evidenced by the inferred pattern of warm temperature advection in Fig. 3.2 (top left) and the positive (downward) surface turbulent heat flux anomalies in Fig. 3.3 (top). The second pattern, which lags the largest KOE SST anomalies by approximately a month, is characterized by statistically significant low pressure anomalies that overlie the positive SST anomalies. The latter pattern is marked by negative (upward) turbulent heat flux anomalies and is most robust at the surface. These results are broadly similar to those found for SST anomalies in the Gulf Stream Extension region in the companion study Wills et al. (2016), as discussed in more detail below.

To provide context for the following analyses, Fig. 3.7 reviews key aspects of the climatological-mean circulation and SST field over the North Atlantic during the NH winter months, similar to Fig. 3.1 for the North Pacific. Figure 3.7a shows the DJF-mean SST and 850-hPa wind fields; Fig. 3.7b shows the standard deviation of daily-mean SST anomalies during DJF. Like the $\mathsf{K_{SST}}$ index, a $\mathsf{G_{SST}}$ index was generated to capture the wintertime SST variability associated with the Gulf Stream region (indicated by the box in Fig. 3.7b). Additional details on the calculation of the $\mathsf{G_{SST}}$ index can be found in Section 2.2.1.1. By construction, the $\mathsf{G_{SST}}$ index is always centered on the same 90-day period as the $\mathsf{K_{SST}}$ index, from 1 December to 28 February.

Figure 3.8 compares the SST and SLP fields regressed onto the $\mathsf{K_{SST}}$ index (left) and the $\mathsf{G_{SST}}$ index (right). As in Fig. 3.2, lags span from -30 to +30 days, with negative lags indicating results where the SLP and SST fields precede peak amplitude in the SST index, and vice versa. In both the North Pacific and North Atlantic, positive SST anomalies in the western boundary current regions are preceded by circulation anomalies that are consistent with anomalous warm air advection over the western boundary current regions. The largest SST anomalies in each basin are of comparable amplitude and decay slowly over time. The circulation anomalies at negative lags are of similar magnitude and size and peak approximately 15-20 days prior to the strongest SST anomalies in both basins.

Importantly, the circulation anomalies at positive lag are also very similar over both ocean basins (bottom panels of Fig. 3.8). In particular, both basins exhibit anomalously low SLP centered approximately over the SST anomalies. High pressure anomalies are also found over each sector at positive lags, but the high pressure anomalies in the North Pacific are not statistically significant (Fig. 3.4). *Hence, the anomalous low pressure pattern that develops over the SST anomalies is viewed as the most robust common aspect of the atmospheric "response" over both ocean basins.*

It is important to note that the processes responsible for the formation of temporal SST anomalies differ between the Kuroshio-Oyashio and Gulf Stream regions. For example, the deeper thermocline in the Gulf Stream Extension region allows for larger quantities of heat storage in the subtropical mode water (STMW) volume, while the shallower thermocline in the Kuroshio-Oyashio Extension region allows for wind-forced thermocline motion to impact heat storage (e.g., Kelly et al. 2010). On low-frequency time scales, wind-driven baroclinic Rossby waves can influence SST anomalies in both western boundary currents, but the impacts on the Gulf Stream are more limited given the relatively small size of the North Atlantic, the orientation of the Gulf Stream, and low-frequency interactions with the Atlantic meridional overturning circulation (e.g., Kwon et al. 2010). Nonetheless, the results presented in Fig. 3.8 suggest that there are very similar spatial and temporal relationships between atmospheric forcing and wintertime SST variability in both the Kuroshio-Oyashio and Gulf Stream Extension regions on daily-mean time scales.

3.3 Influence of the Gulf Stream Extension on the Free Troposphere

As noted in the previous section, the most robust common aspect of the atmospheric circulation "response" to wintertime variations in SSTs over the Kuroshio-Oyashio and Gulf Stream Extension regions is a pattern of low pressure anomalies that develops over the region of SST anomalies. However, Wills et al. (2016) also found a robust and statistically significant pattern of high pressure anomalies that develop downstream and to the northeast of anomalously warm SSTs in the Gulf Stream Extension region. Figure 3.9 reviews the 850-hPa potential temperature (θ_{850}) and 500-hPa geopotential height (Z_{500}) fields regressed onto the G_{SST} index at lags of -15 and +15 days, when the atmospheric "forcing" and "response" patterns over the North Atlantic peak in amplitude, respectively. The results indicate that the anomalous high pressure pattern seen at positive lags in Fig. 3.8 (right column, bottom panels) extends into the upper troposphere and has an equivalent barotropic structure. That is, the circulation anomalies are vertically stacked and increase in strength with height. The pattern of high pressure anomalies is statistically significant at all levels (not shown). The results in Fig. 3.9 also indicate that the temperature changes in the lower troposphere lie directly over the SST anomalies when the atmosphere leads $\mathsf{G_{SST}}$, but are shifted to the northeast of the SST anomalies when the atmosphere lags $\mathsf{G_{SST}}$. As noted in the following sections, the structure of the lower-tropospheric temperature anomalies may provide an important clue regarding the development of the high pressure anomalies over the North Atlantic sector that follow variations in Gulf Stream SSTs by a few weeks.

3.3.1 Signature in Temperature Advection

What physical processes might give rise to the pattern of high pressure anomalies over the North Atlantic at positive lag? It is argued here that the pattern may reflect the circulation response to the poleward and upward advection of anomalously warm air from the Gulf Stream Extension.

As shown in Fig. 3.9, the circulation anomalies associated with $\mathsf{G_{SST}}$ are accompanied by two distinct patterns of lower-tropospheric temperature anomalies: 1) positive temperature anomalies that overlie the Gulf Stream Extension during the weeks preceding variations in $\mathsf{G_{SST}}$; and 2) positive temperature anomalies to the northeast of the Gulf Stream Extension during the weeks following variations in $\mathsf{G_{SST}}$. As shown below, the former temperature anomalies are consistent with temperature advection by the *anomalous* circulation across the *climatological-mean* gradients in lower-tropospheric temperature, whereas the latter are in part dependent on temperature advection by the *climatological-mean* circulation across the *anomalous* gradients in temperature. As such, the former are not dependent on the existence of anomalies in the SST field, but the latter are dependent.

The relative roles of temperature advection by the anomalous and climatological-mean atmospheric circulation can be quantified by decomposing the total anomalous horizontal temperature advection at 850-hPa as follows:

$$(\mathbf{u}\cdot\nabla\theta)_{\mathrm{TOT}} = \overset{\text{(I)}}{\mathbf{u}_{\mathrm{A}}\nabla\theta_{\mathrm{C}}} + \overset{\text{(II)}}{\mathbf{u}_{\mathrm{C}}\nabla\theta_{\mathrm{A}}} + \overset{\text{(III)}}{\mathbf{u}_{\mathrm{A}}\nabla\theta_{\mathrm{A}}}, \tag{3.1}$$

where $\mathbf{u}$ and θ represent the horizontal components of the wind and potential temperature at 850hPa, respectively, C denotes the climatological mean, and A denotes the anomalies. The total anomalous temperature advection is given by the left hand side (LHS), and the terms on the right hand side (RHS) denote I) advection by the anomalous flow across the climatological-mean temperature gradients; II) advection by the climatological-mean flow across the anomalous temperature gradients; and III) advection by the anomalous flow across the anomalous temperature gradients.

Figure 3.10 shows the patterns of temperature advection associated with all three terms at lag 0. The top panel shows results for the first term on the RHS of Eq. (3.1). Contours indicate the climatological-mean isotherms at 850 hPa, vectors indicate the anomalous flow at 850 hPa, and shading indicates the associated anomalous temperature advection. As inferred in Section 3.2 for both the North Pacific and North Atlantic sectors, advection by the anomalous flow across the climatological-mean temperature gradients gives rise to a pattern of temperature tendencies at 850 hPa that peaks over the region of largest SST anomalies, consistent with forcing of the SST field by the anomalous atmospheric circulation.

The middle panel of Fig. 3.10 shows results for the second term on the RHS of Eq. (3.1). Here, contours indicate the 850-hPa temperature anomalies, vectors indicate the climatological-mean flow at 850 hPa, and shading indicates the associated temperature advection. Advection by the climatological-mean flow across the anomalous temperature gradients gives rise to a very different pattern of temperature tendencies than that shown in the upper panel. The anomalous temperature advection in the middle panel has comparable amplitude to that in the top panel, but projects onto the atmospheric temperature and circulation anomalies over the central North Atlantic rather than the Gulf Stream Extension. Since it is dependent on the *anomalies* in lower-tropospheric temperature, the pattern of temperature tendencies in the middle panel of Fig. 3.10 (and thus the lower-tropospheric temperature anomalies over the North Atlantic following $\mathsf{G}_{\mathsf{SST}}$) derive from the warming of the lower troposphere over the Gulf Stream region.

The bottom panel of Fig. 3.10 shows the results for the third term on the RHS of Eq. (3.1). Advection by the anomalous flow across the anomalous temperature gradients has a relatively small contribution to temperature advection in the lower troposphere.

3.3.2 Signature in Vertical Motion

To the extent that the underlying SST field influences variations in lower-tropospheric temperatures over the Gulf Stream Extension, it follows that the pattern of temperature advection in the middle panel of Fig. 3.10 may be at least partially attributed to the underlying temperature anomalies in the SST field. Figure 3.11 reveals that the resulting positive temperature anomalies over the central North Atlantic during the period following peak amplitude in $\mathsf{G}_{\mathsf{SST}}$ are also associated with anomalous rising motion.

Figure 3.11 shows meridional and vertical circulation anomalies regressed on $\mathsf{G}_{\mathsf{SST}}$ at a lag of +20 days over the boxed region indicated in the second panel of Fig. 3.10. The warming to the northeast of the Gulf Stream Extension is marked by positive temperature anomalies that extend throughout the atmospheric column at positive lag. Notably, the positive temperature anomalies also coincide with anomalous upward motion between ~45° and 60° latitude. The anomalous rising motion is consistent with results from a numerical study by Smirnov et al. (2015), who noted that SST anomalies over the Kuroshio-Oyashio Extension region are associated with warm, rising air when the atmosphere lags the SST field by several weeks. Similar results were also noted in previous studies by Czaja and Blunt (2011) and Sheldon and Czaja (2013), who argued that SST-induced heating in the Gulf

Stream region can be advected upward and poleward in the warm sector of extratropical storms.

The anomalous rising motion indicated in Fig. 3.11 is important for three reasons. One, the coexistence of heating and rising motion indicates that anomalous heating may be viewed as forcing, rather than responding, to the changes in vertical motion (if the anomalous motion was downward, then the positive temperature anomalies in the free troposphere would be consistent with adiabatic compression). Two, it suggests that the heating due to extratropical SST anomalies is being balanced, at least in part, by anomalous vertical motion. Third, the changes in vertical motion suggest that the anomalous heating of the lower troposphere in regions to the northeast of the Gulf Stream Extension extends to the upper-tropospheric circulation.

3.4 Conclusions

Observational analyses of daily-mean air-sea interaction in the vicinity of the major NH western boundary currents during the cold season suggest that SST anomalies in both the Gulf Stream and Kuroshio-Oyashio Extension regions are associated with distinct patterns of atmospheric variability that precede and follow peak amplitude in the SST field. Prior to the onset of peak SST anomalies, both basins exhibit similar “atmospheric forcing” patterns that are consistent with anomalous temperature advection due to the anomalous flow acting on the climatological-mean SST gradient. Following peak amplitude in the SST anomalies, both basins exhibit a distinct pattern of pressure anomalies centered over and to the east of the western boundary currents: warm SST anomalies are associated with low SLP anomalies that do not notably amplify with height.

The most notable difference in the lagged patterns between the two ocean basins is the absence in the Pacific sector of significant high pressure anomalies to the north of the warm SST anomalies. In the North Atlantic sector, high pressure anomalies develop downstream of the Gulf Stream region after a few weeks. It is argued that this pattern of circulation anomalies is driven by anomalous vertical motion in the region to the northeast of the Gulf Stream Extension: for example, positive lower-tropospheric temperature anomalies over the Gulf Stream region are advected northeastward by the climatological-flow (Fig. 3.10) where they are at least partially balanced by anomalous rising motion (Fig. 3.11). The anomalous rising motion is important, since it suggests heating over the Gulf Stream Extension is capable of perturbing the free-tropospheric circulation. The discrepancy in the atmospheric response between the North Pacific and North Atlantic sectors may be due to a "third party" influence, such as differences in the geometries of the ocean basins, proximities to land (i.e., interactions with continental air masses), remote teleconnections, or other factors.

Nevertheless, it is hypothesized that the low surface pressure anomalies that lag SST anomalies in both western boundary currents reflects the most common aspect of the "atmospheric response" to the SST field based on the following observations:

1. Results based on analyses over the Kuroshio-Oyashio and Gulf Stream Extension regions both yield very similar atmospheric "response" patterns during the weeks following peak SST anomalies in the western boundary currents (Fig. 3.8).

2. The response patterns have very different spatial structures than the "forcing" patterns that precede peak SST anomalies (Fig. 3.8).

3. The response patterns are associated with negative (upward) surface turbulent heat flux anomalies, indicating that heat is being fluxed from the ocean surface to the overlying atmosphere as the SST anomalies decay (Fig. 3.3).

4. The response patterns are statistically significant over both ocean basins [Fig. 3.4 here and Fig. 3 from Wills et al. (2016)].

5. The response patterns do not emerge from analyses based on the evolution of the atmospheric circulation in the absence of (direct) information from the SST field [Fig. 3.6 here and Fig. 5 from Wills et al. (2016)].

6. The formation of low sea level pressure anomalies at a positive lag over and slightly east of warm SST anomalies is broadly consistent with the theoretical linear response to midlatitude SST anomalies (e.g., Hoskins and Karoly 1981).

The response pattern bears some resemblance to results from previous studies. Frankignoul et al. (2011) also found (weak) low pressure anomalies lagging warm SST anomalies in the KOE region by approximately one season in observational analyses based on lag regressions of a northward shift in the Kuroshio Extension. In addition to the low pressure anomalies, the authors found a significant equivalent barotropic high pressure centered over the northwestern North Pacific, similar to the pattern of (insignificant) high pressure anomalies found in this chapter. Smirnov et al. (2015) found low pressure anomalies over the KOE region in numerical experiments forced with a realistic northward shift of the Oyashio Extension SST front in a low-resolution model, albeit the simulated response in their high-resolution model yielded enhanced ascent and much weaker low pressure anomalies over the KOE region (consistent with the observed response to Gulf Stream Extension SST anomalies over the North Atlantic shown in Figs. 3.9 and 3.11). In observational analyses of decadal-scale variations in KOE SSTs, Taguchi et al. (2012) and Révelard et al. (2016) found that upward surface turbulent heat flux anomalies lagged warm SST anomalies by ~2 months, but their response patterns indicated robust high pressure anomalies near the Gulf of Alaska and the central and northwestern North Pacific, respectively.

Wintertime variations in SSTs in the Kuroshio-Oyashio Extension region are forced not only by variations in the surface turbulent heat fluxes - as emphasized here - but also by the ocean dynamical response to surface wind stress anomalies, variations in STMW volume, changes in the path and transport of the western boundary current, anomalous oceanic temperature advection, remote teleconnections, and other factors (eg., Kelly et al. 2010; Kwon et al. 2010; Frankignoul et al. 2011; Kwon and Joyce 2013; Smirnov et al. 2015). Hence, the results presented in this chapter have potential implications for understanding the atmospheric response to internal ocean dynamics in the Kuroshio-Oyashio Extension region.

In the remainder of this dissertation, the following chapters explore and discuss analyses based on idealized numerical experiments designed to isolate and gain new insight into the role of the ocean in air-sea interaction and the implications for the climate system. The experiments are partially motivated by the observational analyses presented in this chapter, which suggest that small, daily-mean variations in midlatitude SSTs are capable of perturbing variations in the free tropospheric circulation. The experiments presented in the next chapter explore the atmospheric response to a prescribed (and "realistic") SST anomaly at different latitudes and provide an idealized context for interpreting the observed atmospheric response to the SST field over the North Atlantic and North Pacific basins.

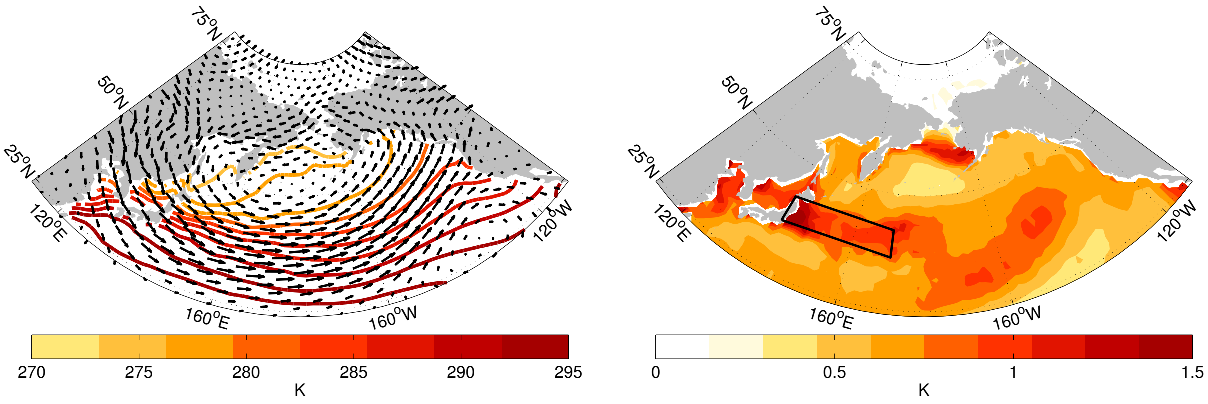
(a) $\overline{\text{SST}}$ and $\overline{\mathbf{u}_{850}}$

(b) σ_{SST}

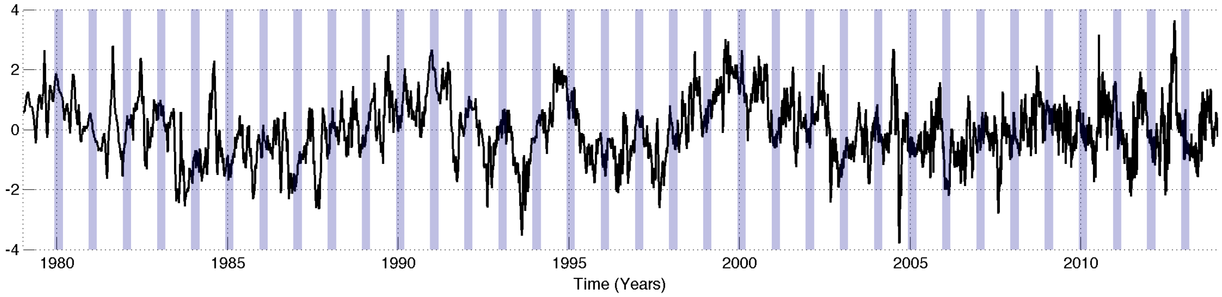
(c) K_{SST} Time Series

Figure 3.1. Climatological values of North Pacific wintertime (DJF) a) SST (contours) and $\vec{u}_{850}$ (vectors) and b) standard deviation of SST (σ_{SST}). The boxed region spans $36°\text{N}-42°\text{N}, 140°\text{E}-171\text{E}°$ and indicates the region used to calculate the K_{SST} index. Units for SST and σ_{SST} are in Kelvin. Units for $\vec{u}$ are in m/s. c) Time series of the standardized K_{SST} index for all days 1979 - 2013. The sections shaded by blue bars denote the DJF periods.

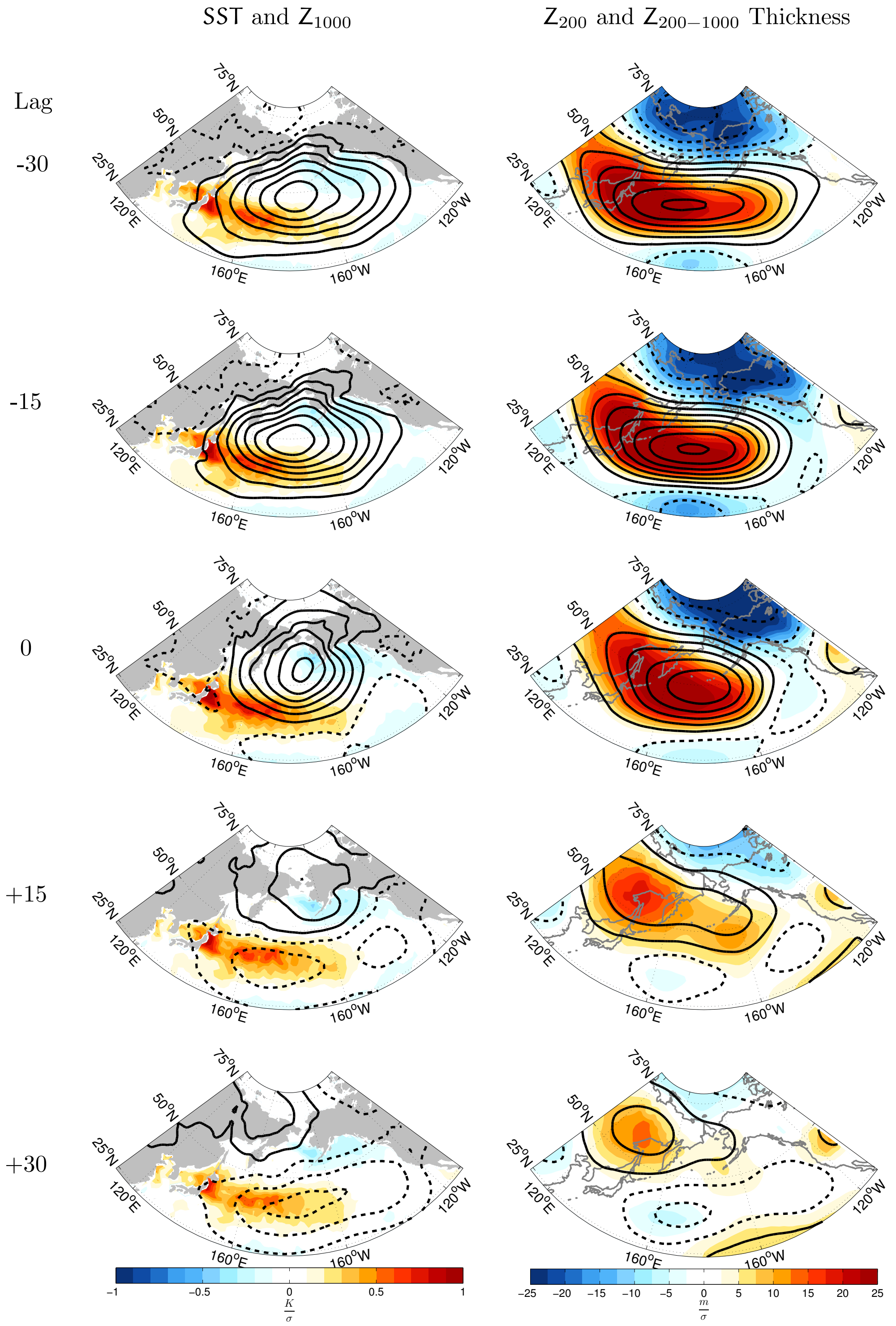

Figure 3.2. Wintertime lag regressions of (left column) Z_{1000} and SST and (right column) Z_{200} and $Z_{200} - Z_{1000}$ thickness onto the standardized K_{SST} index, with negative (positive) lags denoting Z_{1000}/SST and $Z_{200}/Z_{200-1000}$ anomalies leading (lagging) K_{SST}. The SST and $Z_{200-1000}$ thickness fields are indicated in shading, and the Z_{1000} and Z_{200} fields are indicated by contours, where solid (dashed) lines indicate positive (negative) anomalies. Z_{1000} contours are spaced at 4 meters (-6, -2, 2, 6...m) and Z_{200} contours are spaced at 8 meters (-12, -4, 4, 12...m).

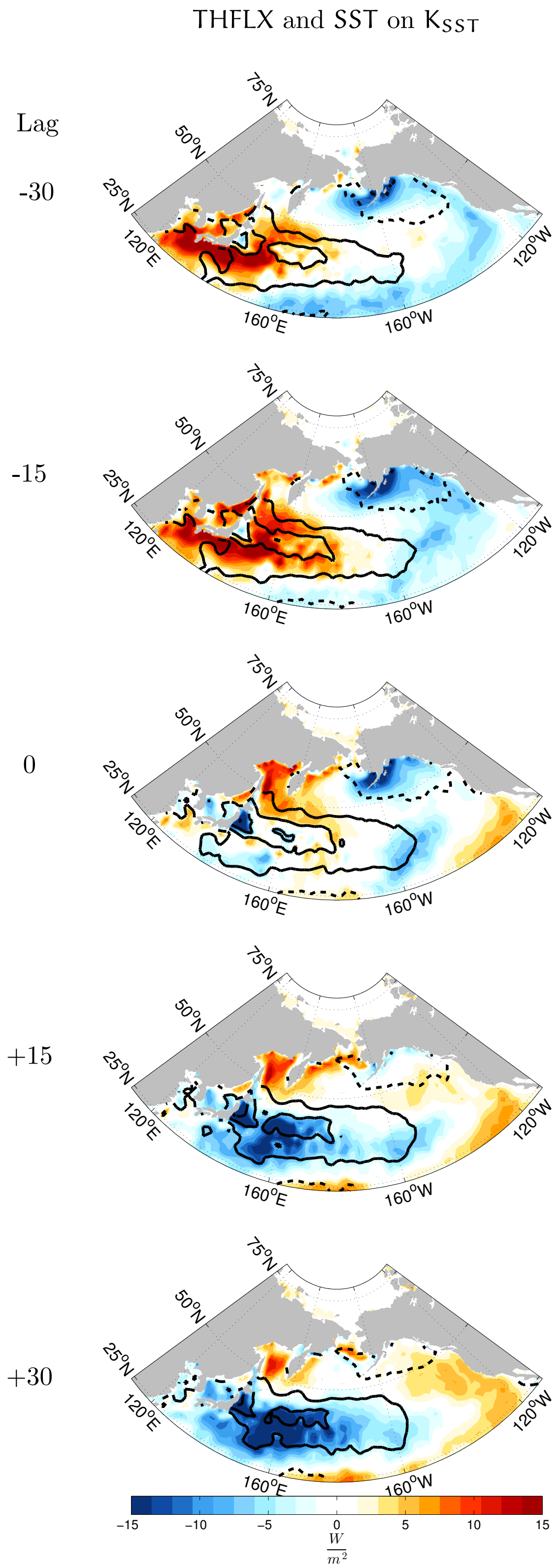
THFLX and SST on K_{SST}

Figure 3.3. Wintertime lag regressions of THFLX (shading) and SST (contours) onto the standardized K_{SST} index. SST contours with solid (dashed) lines represent positive (negative) values at an interval spacing of 0.3 Kelvin (-0.45, -0.15, 0.15, 0.45...K). Note that ERA-Interim THFLX anomalies are positive downward.

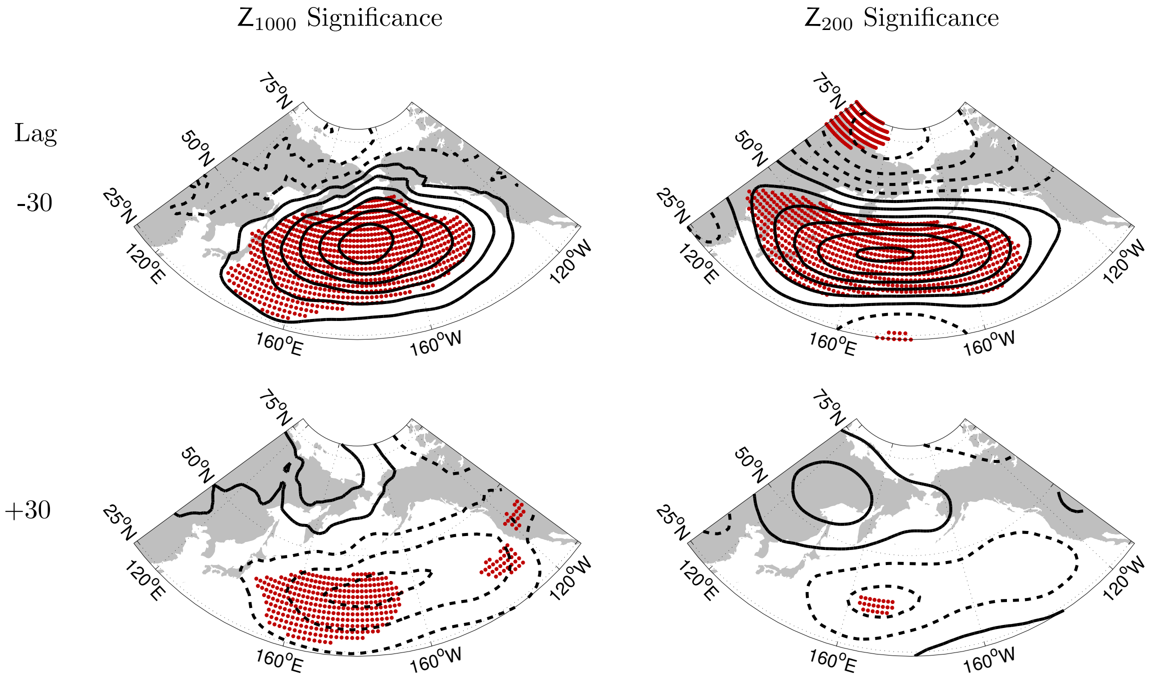

Figure 3.4. Statistical significance of the Z_{1000} (left column) and Z_{200} (right column) anomalies at a lag of (top) -30 days and (bottom) +30 days. Regressions are shown in contours and stippling indicates significance at the 95% confidence level using the two-tailed Student's *t* test. Degrees of freedom are calculated per Eq. (31) from Bretherton et al. [1999].

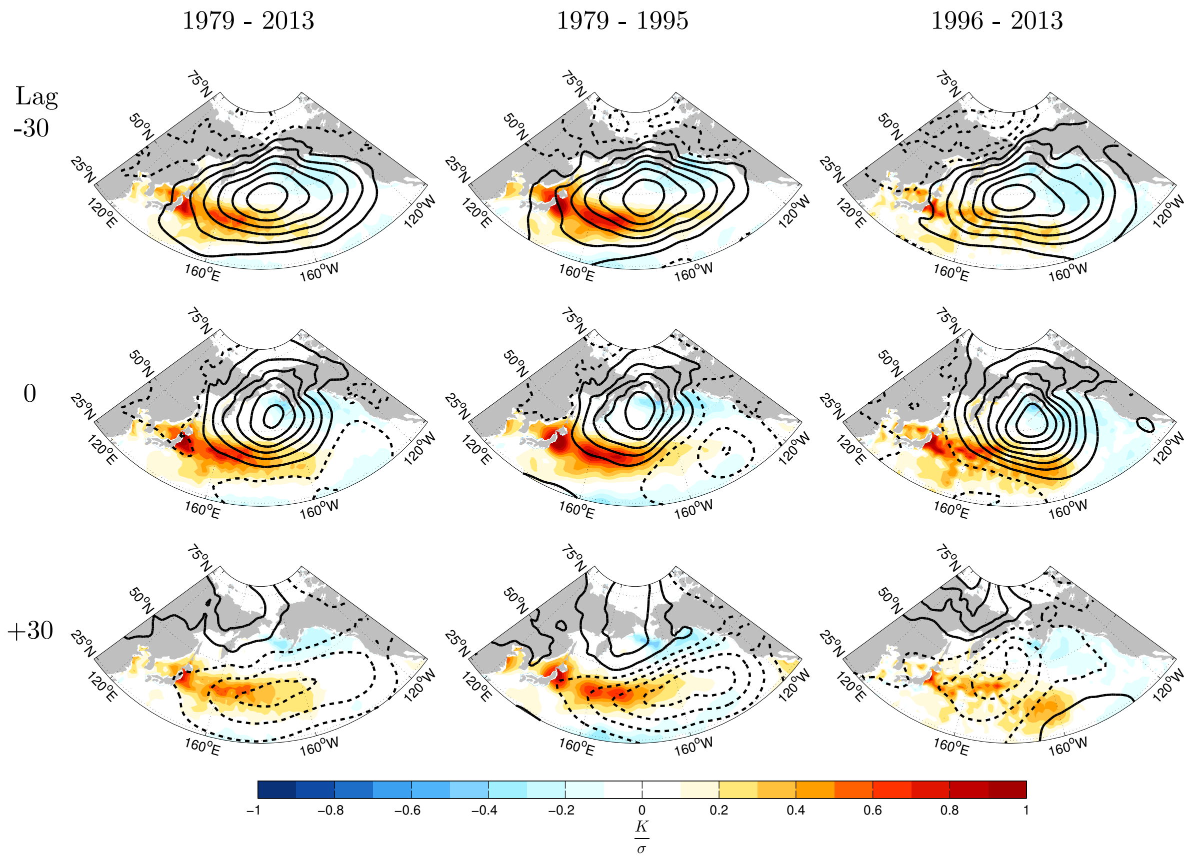

Figure 3.5. Same as in the left column of Fig. 3.2, except the middle and right columns show results of SST (shading) and Z_{1000} (contours) regressed onto K_{SST} for the ERA-Interim time periods of 1979 - 1995 and 1996 - 2013, respectively.

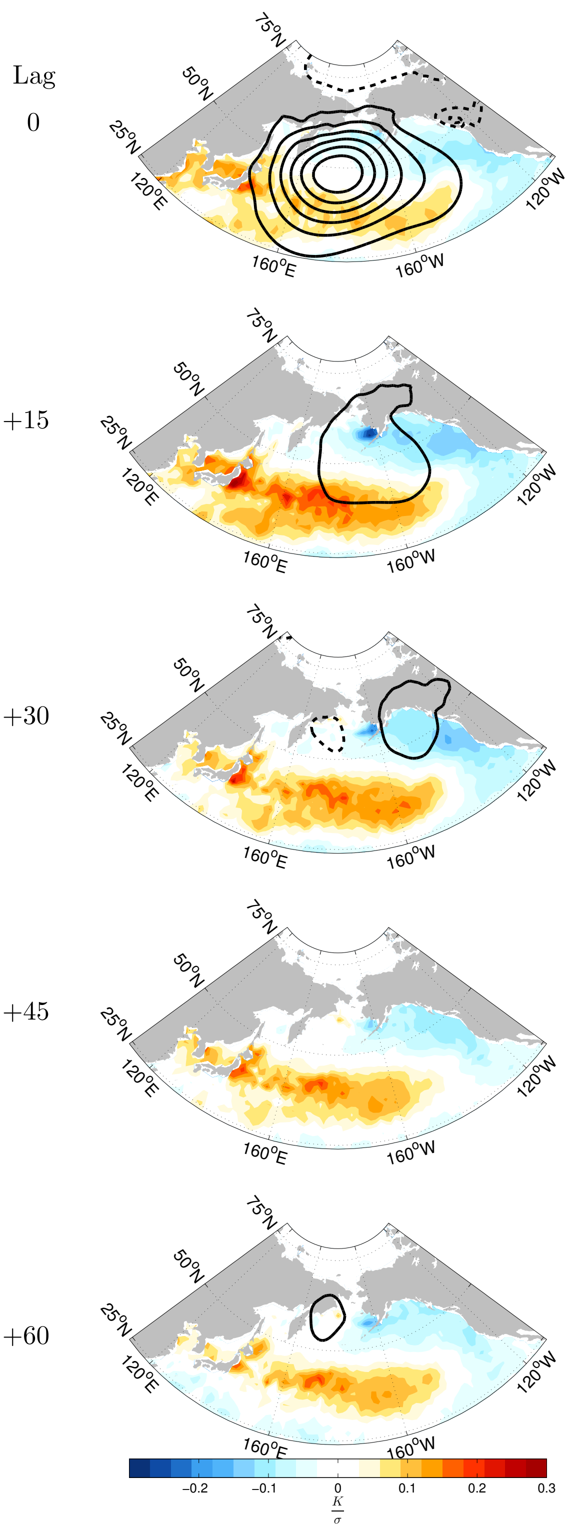

SST and Z_{1000} on K_{ATMO}

Figure 3.6. Daily lag regressions of SST (shading) and Z_{1000} (contours) onto the standardized K_{ATMO} index. Z_{1000} contours with solid (dashed) lines represent positive (negative) values at an interval spacing of 15 meters (-22.5, -7.5, 7.5, 22.5...m). Positive lags indicate the fields lagging the K_{ATMO} index.

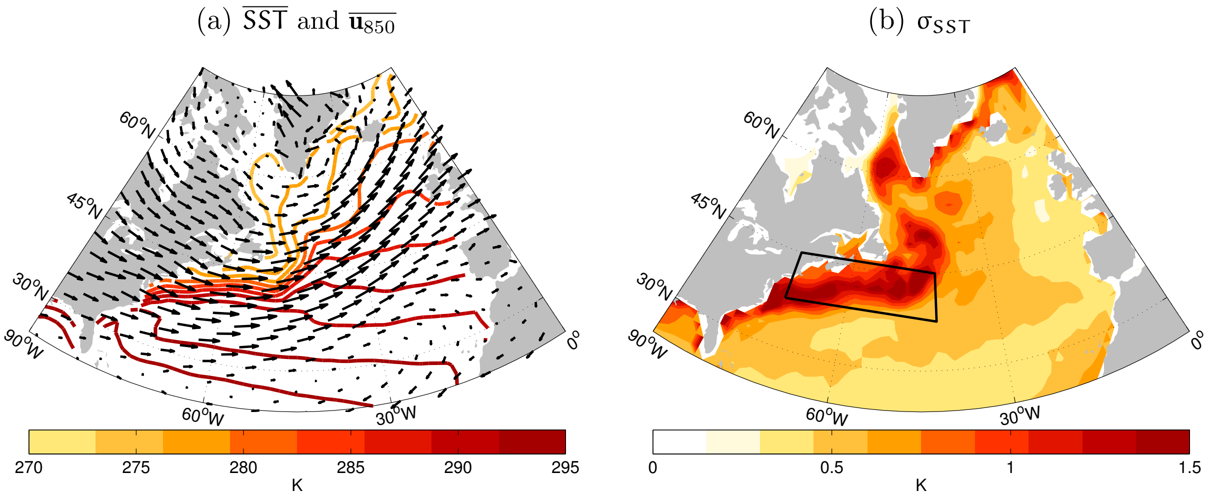

Figure 3.7. North Atlantic wintertime (DJF) a) climatological-mean SST (contours) and $\vec{u}_{850}$ (vectors) and b) standard deviation of SST (σ_{SST}). The boxed region spans $37.5°\mathrm{N} - 45°\mathrm{N}, 72°W - 42°W$ and indicates the region used to calculate the $\mathsf{G}_{\mathsf{SST}}$ index. Units for SST and σ_{SST} are in Kelvin. Units for $\vec{u}$ are in m/s.

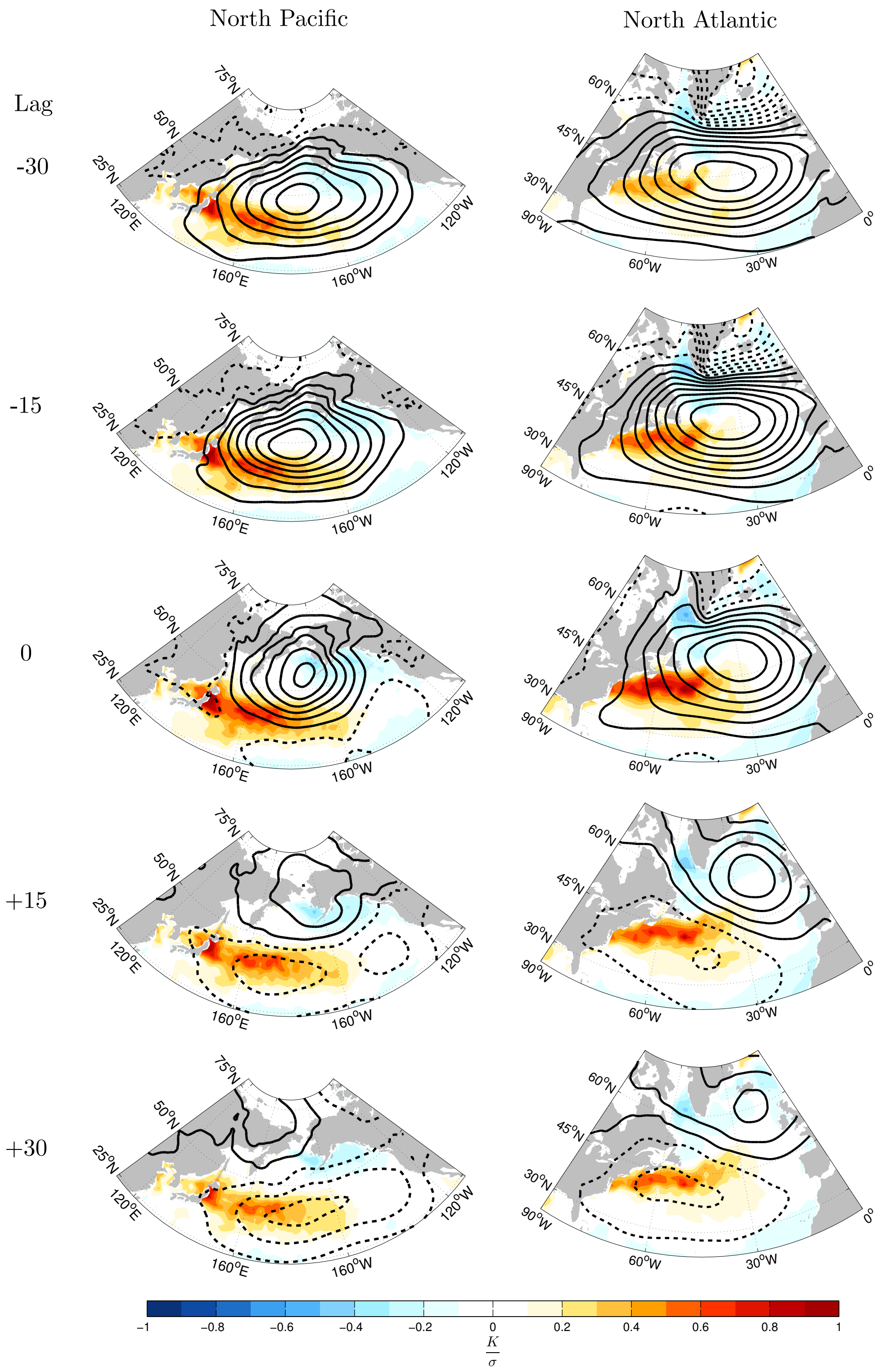

Figure 3.8. Wintertime lag regressions of Z_{1000} and SST onto the standardized (left column) $\mathsf{K}_{\mathsf{SST}}$ index and (right column) $\mathsf{G}_{\mathsf{SST}}$ index. Negative (positive) lags denote the Z_{1000}/SST anomalies leading (lagging) $\mathsf{K}_{\mathsf{SST}}$ and $\mathsf{G}_{\mathsf{SST}}$. The Z_{1000} field is indicated by contours (spaced at 4 meters; -6, -2, 2, 6...m), where solid (dashed) lines indicate positive (negative) anomalies.

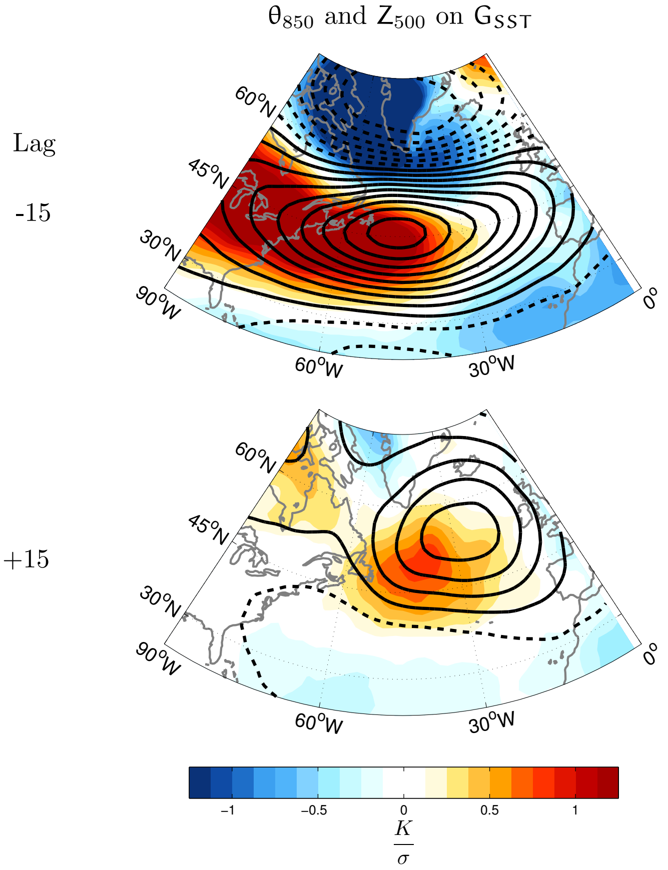

Figure 3.9. As in the right column of Fig. 3.8, except for Z_{500} (contours) and θ_{850} (shading) regressed onto the standardized G_{SST} index at lags of (top) -15 and (bottom) +15 days. Solid (dashed) lines indicate positive (negative) anomalies, and Z_{500} contours are spaced at 6 meter (-9, -3, 3, 9...m) intervals.

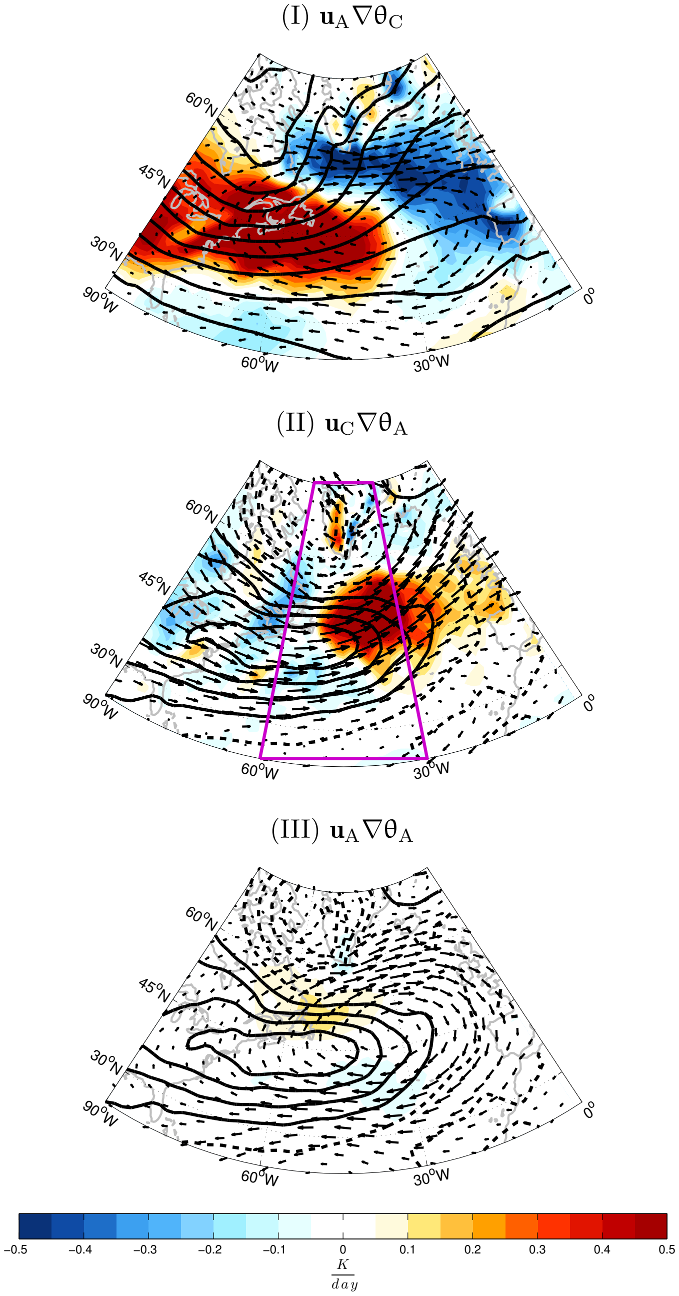

Figure 3.10. The 850-hPa wintertime patterns of anomalous horizontal temperature advection associated with all three terms on the rhs of Eq. 3.1 at lag 0: (I) advection of the climatological-mean temperature gradient by the anomalous flow, (II) advection of the anomalous temperature gradient by the climatological-mean flow, and (III) advection of the anomalous temperature gradient by the anomalous flow. Contours represent the spatial temperature distribution, vectors represent the wind, and shading represents temperature advection. Units for SST, **u**, and temperature advection are in K, m/s, and K/day, respectively. The purple box in (II) indicates the region averaged for the cross section in Fig. 3.11.

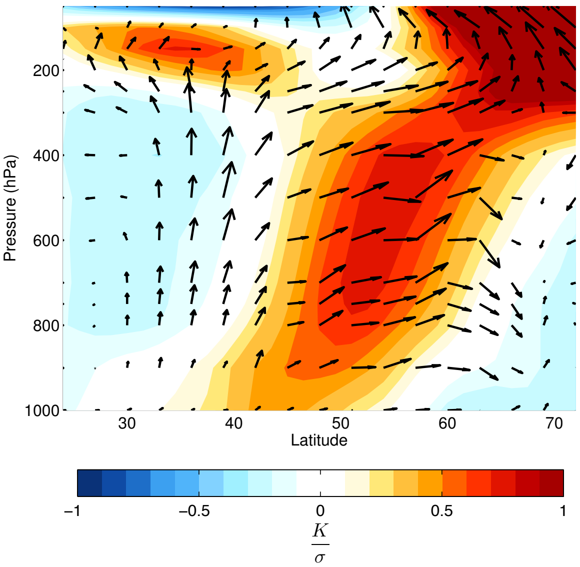

Figure 3.11. The 60°W - 30°W averaged vertical cross section of θ (shading) and v, w (vectors) regressed onto the standardized G_{SST} index at a lag of +20 days. v, w vectors are in units of $\frac{m}{s}$, with w scaled by a factor of 2×10^3 for qualitative comparison.

CHAPTER 4: A SYSTEMATIC INVESTIGATION OF THE ATMOSPHERIC RESPONSE TO SURFACE THERMAL FORCING IN AN IDEALIZED GLOBAL CLIMATE MODEL

To the extent that they are realistic, numerical models serve as helpful tools for testing theories and exploring expected behaviors observed in the climate system, such as the relationships between the ocean and the atmosphere. In the previous chapter, observational analyses based on daily-mean data indicated that a robust pattern of atmospheric circulation anomalies lag anomalously warm SSTs over the Gulf Stream and Kuroshio-Oyashio Extension regions by approximately 2-3 weeks; however, questions remain as to why the observations reveal such a consistent pattern of atmospheric circulation anomalies and if the results can be interpreted as the atmospheric response to the SST field. To address these questions, idealized numerical experiments are performed to explore the tropospheric circulation response to a SST anomaly (or surface thermal forcing) of realistic size and amplitude at varying latitudes between the Equator and the pole. The analyses are based on simulations from an atmosphere-only general circulation model (NCAR CAM5.3, as described in Ch. 2) in which sea surface temperatures are prescribed at the lowest boundary on an aquaplanet surface (i.e., a completely water-covered surface) that remain “fixed”, or unchanging, with time. Hence, the results from the SST perturbation experiments provide a simple context for understanding the atmospheric response to a constant one-way forcing by the ocean.

Such an idealized approach is an important component of the modelling hierarchy, in which models of increasing complexity and experimental configuration provide a framework for evaluating the link between theory, observations, and complex models (e.g., Neale and Hoskins 2000a,b; Blackburn and Hoskins 2013; Williamson et al. 2013). In other words, a simplified model framework allows for a critical view into the processes responsible for the response to climate perturbations. Given the coupled nature of the ocean and atmosphere systems, as well as complicating factors such as land-sea contrast, orography, sea ice, and asymmetric SST distributions, it can be difficult to isolate the direct influence of the ocean on the atmospheric circulation in global climate models (and especially observations). To simplify this problem, some numerical studies have used aquaplanet configurations in global climate models to simulate an idealized climate above a completely water-covered planet with otherwise Earth-like characteristics (e.g., Neale and Hoskins 2000a,b). A key advantage to using this simplified configuration is the ability to generate a realistic and equilibrated climate while eliminating zonal asymmetries and interactions with complex land surfaces in a relatively short simulation (e.g., Medeiros et al. 2015, 2016), thus alleviating limitations due to resource allocations. The following section provides a non-inclusive overview of previous aquaplanet studies with emphasis on the different applications of various aquaplanet configurations.

4.1 A Brief Overview of Previous Aquaplanet Experiments

A variety of aquaplanet configurations have been utilized in idealized numerical experiments to explore the role of the midlatitude ocean in air-sea interaction. For example, configurations with zonally-symmetric SST distributions across the globe (i.e., where only meridional SST gradients exist) have been used to explore the relationships between the atmospheric circulation and variations in the strength and position of midlatitude SST gradients (e.g., Brayshaw et al. 2008; Nakamura et al. 2008; Sampe et al. 2013; Michel and Riviére 2014; Ogawa et al. 2016). As mentioned in the first chapter of this dissertation, experiments by Brayshaw et al. (2008) revealed that increases in the midlatitude SST gradient generally lead to stronger and more poleward shifted storm tracks. However, their results also provided unique insights into the sensitivity of the relationship between the storm track (and associated polar front, or eddy-driven, jet) and the position of the SST gradient anomaly relative to the subtropical jet. In a study by Nakamura et al. (2008), front/no front experiments based on the (idealized) position and strength of the Antarctic Polar Frontal Zone in the Southern Hemisphere indicated that oceanic frontal zones help to maintain the intensity and structure of the eddy-driven annular mode. Similar results were found in front/no front experiments by Sampe et al. (2013), who further suggested that midlatitude oceanic frontal zones play an important role in maintaining the year-round annular mode signal against a wintertime intensification of the subtropical jet. In contrast to front/no front experiments, Ogawa et al. (2016) investigated the sensitivity of the Southern Hemisphere annular mode to the location of an oceanic frontal zone by systematically changing the latitude of the frontal gradient in the SST profile, whereas Michel and Riviére (2014) explored the response of the storm track and eddy-driven jet to various SST profiles defined by piecewise-linear functions of latitude that were designed to study sensitivities to the position, width, and intensity of the midlatitude SST front as well as to tropical SSTs.

In addition to zonally-symmetric SST experiments, studies have utilized aquaplanet configurations with asymmetric SST distributions to explore other topics of air-sea interaction, such as the influence of zonal variations in midlatitude SSTs, local "hot spots" (or anomalous heating) in the ocean, more realistic SST distributions, and zonal asymmetries that mimic land-sea contrasts (e.g., Inatsu et al. 2003; Maloney and Sobel 2007; Brayshaw et al. 2008; Shaw and Voigt 2016). Inatsu et al. (2003) explored the midwinter storm track response to midlatitude SST anomalies of zonal wavenumber-1 structure placed at various (middle) latitudes against a zonally-uniform background SST distribution. Results from their asymmetric SST experiments indicated that, depending on latitude, the net effects of SST on vertical wind shear and precipitation (and the resulting contributions to low-level baroclinicity) either combine to amplify storm activity or cancel out and exert little influence on the storm track. Similar results were found in wavenumber-1 experiments performed by Brayshaw et al. (2008), who also noted that regardless of the sign of the SST anomaly producing the gradient change, intensification/weakening of the storm track and eddy-driven jet by the anomalous SST gradient still occurred. In other applications of aquaplanet experiments, Maloney and

Sobel (2007) incorporated a slab-ocean model to perform highly idealized "hot spot" experiments in which a positive equatorial SST anomaly is imposed on a globally uniform 28°C SST background state to analyze the short-term response of the climate system to tropical heating, and Shaw and Voigt (2016) prescribed zonally-asymmetric subtropical SSTs to mimic land-ocean contrasts in experiments aimed at exploring the mechanisms linking subtropical and extratropical circulation responses to climate change.

4.2 Motivation for Experimental Design

The goals of this chapter are to address outstanding questions raised by key observational results from Ch. 3 and provide a simplified model framework to critically assess the one-way influence of the ocean on the atmosphere at different locations across the globe. To do this, hemispherically-asymmetric SST experiments are designed to explore the local and large-scale time-varying atmospheric response to a sudden "switch-on" of surface thermal forcing imposed on a fixed, zonally-symmetric background SST profile. The key focus of the study is to compare the atmospheric response to a SST anomaly placed at varying latitudes between the Equator and the pole, specifically centered at 0°, 20°N, 45°N, 60°N, and 90°N. Simulations are performed on a relatively new aquaplanet configuration of the Community Atmosphere Model, Version 5.3 (CAM5.3; see Ch. 2 for more details) under perpetual equinox conditions, when there are equal amounts of insolation in the southern and northern hemispheres, thus removing seasonality but retaining the diurnal cycle (e.g., Medeiros et al. 2016). Two sets of experiments are performed to assess the steady-state and transient atmospheric circulation responses to the different SST anomalies.

An aquaplanet configuration is utilized to simplify the experiments by removing complex boundary forcing (i.e., land-sea contrast, orography, zonal asymmetries, etc.) from the simulated climate system that would otherwise complicate the problem. Unfortunately, such an idealized framework is not without its limitations. For example, in the absence of topography (and due to fixed boundary conditions), the model is unable to simulate dry continental air masses or western boundary currents, both of which are prominent features in the observational analyses from Ch. 3. Hence, it is possible that the model is unable to fully resolve some of the observed physical processes, such as the anomalous temperature advection shown in Fig. 3.10. Despite these limitations, the idealized framework provides a platform for uncoupling the two-way interactions between closely-coupled climate systems.

The novelty of the approach is seen in the experimental design, which differs from previous numerical experiments on midlatitude air-sea interaction in the following ways. First, an elliptically-shaped SST anomaly is prescribed to be of realistic size and amplitude, spanning 20° latitude by 40° longitude with a maximum magnitude of 1 Kelvin, as motivated by the observed daily-mean SST anomalies associated with the Gulf Stream and Kuroshio-Oyashio Extensions from Ch. 3 (e.g., Wills et al. 2016; Wills and Thompson 2018). Similar studies have employed much larger perturbations in the extratropical SST field, such as SST anomalies spanning broad scales (e.g., Inatsu et al. 2003; Brayshaw et al. 2008) or multiplied by large factors (e.g., Deser et al. 2004, 2007; Small et al. 2014). While larger SST perturbations can be useful for discerning the direct linear response from internal variability (e.g., Palmer and Sun 1985), they are not typical in nature. The zonally-asymmetric SST experiments also differ from other studies that have investigated changes in the zonally-symmetric meridional SST gradient (e.g., Sampe et al. 2013; Michel and Riviére 2014; Ogawa et al. 2016).

Second, the zonally-symmetric background SST field is defined by a simple analytical function based on the observed 2-meter temperature ($\mathsf{T_{2m}}$) profile during average equinoctial conditions in both hemispheres. As explained in Ch. 2 and illustrated in Fig. 2.1, this profile reduces sea surface temperatures to values below 273 Kelvin poleward of 60° latitude, potentially introducing complications due to sea ice. Such an approach is not unreasonable, as demonstrated by Kang et al. (2008, 2009), who permitted ocean temperatures to drop below freezing (with no sea ice) in idealized slab-ocean experiments to study the influence of extratropical thermal forcing. However, to exclude complications due to sea ice, other aquaplanet studies have set SSTs to 273 Kelvin at all latitudes poleward of 60° or constrained the meridional SST gradient to reach 273 Kelvin at the pole (e.g., Neale and Hoskins 2000a; Brayshaw et al. 2008; Sampe et al. 2013; Williamson et al. 2013; Medeiros et al. 2015, 2016). Nonetheless, the background configuration presented here provides a more realistic representation of the observed near-surface temperature field and retains SST gradients at higher latitudes, which will likely yield better insights for comparing the atmospheric response to SST anomalies across the globe. Indeed, the 10,000-day control appropriately reproduces key features of the observed large-scale atmospheric circulation as seen in Fig. 4.1, which indicates zonal-mean surface easterlies (westerlies) in the tropics (midlatitudes), subtropical jets near 30° latitude, and eddy-driven jets near 45° latitude.

The remainder of this chapter presents results from the steady-state and transient simulations. Note that throughout the chapter, anomalies are defined as differences between a perturbation experiment and the control (perturbation experiment - control), and the five perturbation experiments are referred to as 1KEQ, 1K20N, 1K45N, 1K60N, and 1K90N for a SST anomaly centered at 0°, 20°N, 45°N, 60°N, and 90°N, respectively, as shown in Fig. 4.2. The steady-state results are presented in Section 4.3. In Section 4.4, the results are explored in the context of model internal variability. The transient evolution of the atmospheric response is examined in Section 4.5, and conclusions are provided in Section 4.6.

4.3 Steady-State Atmospheric Response to SST Perturbations

The first set of experiments explores the steady-state atmospheric response to a surface thermal forcing (i.e., a prescribed SST anomaly) imposed at five different latitudes across the model northern hemisphere. Recall from Eq. 2.8 that each SST anomaly is prescribed to be an elliptical shape as a function of latitude and longitude spanning 20° and 40°, respectively, except for the anomaly at 90°N, which is circular and spans all longitudes along a latitude band. By this definition, the relative size of the SST anomaly decreases when the latitude center is shifted poleward, but the surface area of the heating remains proportional to the latitude band (or polar region), as illustrated in Fig. 4.2. For reference, the SST anomalies are labeled by their corresponding experiment names. Also note that 1KEQ is larger in size than 1K20N but appears smaller due to the positioning of the satellite map projection. This section presents the results from the steady-state experiments, first analyzing the large-scale atmospheric circulation response to an anomalous heat source on the equator, and then exploring and comparing the atmospheric responses to SST anomalies situated at different latitudes.

4.3.1 The Atmospheric Response to an Equatorial Heat Source

The left panel of Fig. 4.3 shows the steady-state sea level pressure (SLP; contours) response to a heating imposed at the equator (1KEQ) overlaid on the SST anomalies (shading). Note that the gray contours reflect a different interval spacing to highlight the smaller (but important) SLP anomalies associated with the local tropical response, as described in the caption. The right panel of Fig. 4.3 shows the steady-state turbulent heat flux anomalies (THFLX, defined as the sum of sensible and latent heat flux anomalies; shading) and the 850-hPa horizontal wind anomalies ($\vec{u}_{850}$; vectors) over the Tropics. Note that unlike the THFLX anomalies from ERA-Interim (Ch. 3), the THFLX anomalies generated by CAM5.3 are positive *upward.*

The tropical atmospheric response to anomalous heating on the equator is mostly consistent with that found in Gill (1980), where the local response at the surface (Fig. 4.3, left panel) is characterized by low pressure in the vicinity and to the east of the heat source (indicative of an eastward-moving Kelvin wave) and anomalous upward motion directly above the heat source (Fig. 4.4, contours). Results based on the anomalous 850-hPa horizontal wind field (Fig. 4.3, right panel) reveal the formation of weak low-level low pressure systems on the northwest and southwest flanks of the forcing region. This result is also consistent with the Matsuno-Gill model, in which two cyclones associated with westward-propagating Rossby waves are generated to the west of the forcing region. However, both the Kelvin and Rossby wave responses appear weaker compared to that found in Gill (1980). This damped response may be in part due to competing thermal influences by elevated heating (e.g., Gill 1980) and surface temperature gradients (e.g., Lindzen and Nigam 1987). Previous studies have argued that the relative influences of elevated heating and SST gradients vary across the tropics, with one dominating the circulation response over the other. For example, deep convective heating is largely found to determine the bulk of the surface zonal wind field throughout the tropics, while regions of asymmetric heating associated with tropical SST gradients are found to force low-level convergence of the surface wind field (e.g., Chiang et al. 2001; Back and Bretherton 2009).

The results in Figs. 4.3 - 4.5 provide supporting evidence that there might be competing atmospheric responses to surface temperature gradients and elevated heating in the 1KEQ SST perturbation experiment. Highly positive THFLX anomalies (Fig. 4.3, right panel) indicate that strong fluxes of heat from the surface to the atmosphere occur directly over the forcing region in an attempt to balance the (infinite) equatorial heat source. This result is consistent with the linear theory proposed by Lindzen and Nigam (1987), who noted the importance of differential heating between the sea surface and the boundary layer in modifying boundary layer temperatures that in turn induce changes in the eddy sea level pressure field. In fact, a surface high pressure anomaly to the west of the heating region (Fig. 4.3, left panel) may reflect the atmospheric response to a local boundary layer temperature gradient, where anomalously high pressure forms over relatively cooler air (i.e., relative to the prescribed heating) and anomalously low pressure forms over the warm SST anomaly. This may also explain why the results indicate a weaker Kelvin wave signal to the east of the forcing region, as low pressure anomalies associated with the response to elevated heating are potentially damped by high pressure anomalies associated with the local surface temperature gradient (e.g., Gill 1980; Lindzen and Nigam 1987). Indeed, significance testing reveals that the weak pattern of surface low pressure to the east of the surface heating is barely statistically significant, while the surface high pressure pattern to the west is seemingly robust, as indicated in the lower left panel of Fig. 4.5.

The results shown in vertical cross-sections in Fig. 4.4 further suggest that the anomalous surface pressure gradient (and associated low-level wind convergence) on the western flank of the forcing region leads to anomalous rising motion aloft, consistent with the paradigm in Lindzen and Nigam (1987). The vertical cross-section is averaged over an equatorial band from 5°S - 5°N to isolate the central region of heating and the associated zonal temperature gradients. The contours in Fig. 4.4 represent anomalous vertical velocity, where negative anomalies indicate upward motion. The results show a slight westward tilt in the strongest region of rising motion relative to the location of the thermal forcing. It is possible that the tilt reflects the additional influence of low-level convergence in forcing anomalous rising motion on the western edge of the heating region.

Also consistent with the existing literature, the most robust aspect of the large-scale atmospheric response to anomalous tropical heating manifests through teleconnection patterns throughout the remote tropics and extratropics (e.g., Hoskins and Karoly 1981; Horel and Wallace 1981; Bantzer and Wallace 1996; Alexander et al. 2002; Lintner and Chiang 2006; Maloney and Sobel 2007). The right panel of Fig. 4.4 shows the steady-state response in the potential temperature field (shading) overlaid by the associated changes in vertical motion. There is a clear warming signal that extends throughout the upper tropical troposphere, where a maximum heating occurs in the vicinity of upward rising motion. The anomalous warming is also more uniformly distributed throughout the upper troposphere as it spreads eastward, similar to results found in previous studies (e.g., Bantzer and Wallace 1996; Lintner and Chiang 2006; Maloney and Sobel 2007). The results in the top row of Fig. 4.5 show a planar view of the steady-state potential temperature anomalies in the low (850 hPa), middle (500 hPa), and upper (200 hPa) levels of the troposphere across the globe. Geopotential height anomalies (contours) at 500 hPa and 200 hPa (Fig. 4.5, middle and right, respectively) show raised heights throughout the tropics associated with the middle and upper tropospheric warming patterns. SLP and geopotential height anomalies also highlight robust teleconnection patterns in the extratropics, consistent with the theoretical, steady-state linear response to thermal forcing via atmospheric Rossby wave trains (e.g., Hoskins and Karoly 1981; Horel and Wallace 1981; Alexander et al. 2002). While the results from the 1KEQ perturbation experiments are not exactly new, they provide an interesting insight into the roles of elevated heated versus surface temperature gradients in forcing the tropical atmospheric response to a fixed equatorial heat source. The results also provide confidence in the ability of CAM5.3 to generate a realistic climate response to anomalous tropical SSTs despite the simplistic aquaplanet configuration.

4.3.2 Comparison of the Atmospheric Response to Perturbations at Different Latitudes

This section presents findings for the 1K20N, 1K45N, 1K60N, and 1K90N SST perturbation experiments. Similar to Fig. 4.3, the results in Fig. 4.6 show the steady-state SLP anomalies and associated SST (left column) and THFLX (right column) anomalies for the remaining four experiments. Surprisingly, there is a consistent steady-state SLP response to the imposed thermal forcing at each of the four latitudes, and the anomalous patterns are all of similar sign and amplitude. The pattern appears to be generally zonally-symmetric and is characterized by anomalously high SLP poleward of 60°N, with a weaker band of anomalously low SLP throughout the midlatitudes confined between 30°N - 60°N. The associated THFLX anomalies seen in the right column of Fig. 4.6 indicate that the largest fluxes of heat from the surface to the atmosphere are located in the vicinity of the SST anomaly, which is to be expected given the infinite nature of the heat source. However, it is interesting to note that as the SST anomaly is placed at higher latitudes, the relative amplitude of steady-state THFLX anomalies appears to decrease (becoming very small at the pole), possibly reflecting the decrease in surface area of the SST anomaly with increasing latitude.

While the large-scale pattern of SLP anomalies is broadly similar for the 1K20N, 1K45N, 1K60N, and 1K90N SST perturbation experiments, there are still some small differences in the circulation responses. The pattern of low pressure anomalies is less uniform throughout the midlatitudes in 1K20N (bottom panels of Fig. 4.6), with a smaller locally-confined region of low pressure anomalies coincident with the SST anomaly located to the south of 30°N. The largest difference in the pattern of high SLP anomalies between the experiments occurs in 1K45N, where the center of action is more displaced from the pole compared to the other responses, seemingly due to a region of low pressure anomalies that extend past 60°N. The results from 1K60N show that the SST anomaly is coincident with the node of the pressure dipole, rather than anchoring a more local "thermal low" consistent with a hydrostatic pressure adjustment. Furthermore, the center of the anomalous high pressure pattern is closest to the SST anomaly in 1K90N, suggesting that the simulated atmospheric response is not dependent on the relative latitude of the SST anomaly.

The dipole pattern is also evident in the steady-state geopotential height anomalies found at middle and upper levels of the troposphere, as shown in Fig. 4.7. The results in the left column of Fig. 4.7 are the same as in the left column of Fig. 4.6, while the middle and right columns show the steady-state responses in the geopotential height field at 500 hPa (Z_{500}) and 200 hPa (Z_{200}), respectively. In all four SST perturbation experiments, the low/high pressure patterns indicate an equivalent barotropic atmospheric response, where the circulation anomalies are vertically stacked and increase in strength with height. However, there appears to be large variability in the geopotential height response at 500 hPa (where the response is also least zonally-symmetric) between the experiments, especially in 1K20N and 1K45N. The weakest signature of the dipole pattern occurs in 1K20N (Fig. 4.6, bottom middle), where the Z_{500} anomalies are mostly confined to the centers of action seen at the surface (Fig. 4.6, bottom left). In contrast, positive Z_{500} anomalies develop over the anomalous surface low pressure coincident with the SST anomaly region. Positive Z_{500} anomalies also appear to extend over the region of SST anomalies in 1K45N, but the overall dipole pattern is still largely apparent throughout the 500 hPa level.

Figure 4.8 shows the same results as in Fig. 4.7, except stippling is added to indicate where the SLP and geopotential height anomalies are statistically significant at the 95% confidence level (see caption for details). While the anomalous dipole pattern is broadly zonally-symmetric and robust across the different SST perturbation experiments, the statistically significant features are mainly confined to the centers of action where the anomalies in SLP and geopotential height are the strongest. Results from the 1K20N, 1K60N, and 1K90N experiments also indicate a statistically significant band of weak Z_{500} and Z_{200} anomalies in regions of the subtropics and tropics, while a similar band of statistically significant SLP anomalies appears in 1K20N. Overall, the significance testing shown in Fig. 4.8 suggests that the equivalent barotropic "zonally-symmetric" dipole structure is the most robust feature of the steady-state atmospheric circulation response to fixed surface thermal forcing, regardless of the latitude of the SST anomaly. However, it is unclear as to *why* this robust and consistent response occurs. The next section explores a possible relationship between the model's internal variability and the anomalous circulation pattern described here.

4.4 The Role of Internal Variability

As noted in the previous section, the dipolar structure of the anomalous zonal-mean geopotential height field is the most robust and interesting aspect of the simulated atmospheric responses to fixed SST anomalies imposed throughout the model's northern hemisphere. In particular, the hemispheric scale and zonally-symmetric features of the response pattern are reminiscent of the leading modes of atmospheric variability, or the annular modes, which exist year round and exhibit a similar dipolar structure (e.g., Kidson

1988; Thompson and Wallace 1998, 2000; Limpasuvan and Hartmann 1999). To better understand the steady-state atmospheric response to a prescribed SST anomaly in the 1K20N, 1K45N, 1K60N, and 1K90N perturbation experiments, the following analyses explore the zonally-symmetric components of the anomalous dipole pattern.

4.4.1 The Leading Mode of Model Atmospheric Variability

Empirical Orthogonal Function (EOF) analysis was performed on the SLP, Z_{500}, and Z_{200} fields from the 10,000-day control simulation to identify the leading pattern (defined by EOF1) of atmospheric variability in the model's northern and southern hemispheres. The EOFs were calculated using monthly-mean output over the northern and southern hemispheres separately, and the time mean was removed. Given that the simulations were performed under perpetual equinox conditions, there was no need to remove the seasonal cycle. Additional details on the method of EOF analysis can be found in Section 2.2.2.3. Figure 4.9 shows the leading (or dominant) pattern of internal variability in the SLP (top), Z_{500} (middle), and Z_{200} (bottom) fields for the model's northern (left column) and southern (right column) hemispheres. The results are shown as regressions of the SLP and geopotential height anomalies (from the control) onto the respective principal component time series (PC1) associated with EOF1 and hence are expressed in physical units. The percentages denote the amount of variance explained by the EOF1 pattern at its respective level.

The similarities between the leading modes of internal variability over the northern hemisphere (Fig. 4.9, left column) and the atmospheric response patterns (Fig. 4.7) at each level are immediately obvious. The EOFs in Fig. 4.9 are characterized by pressure anomalies of opposite sign between the polar region poleward of 60°N and the midlatitude region between 30°N - 60°N, similar to the results found for 1K20N, 1K45N, 1K60N, and 1K90N (Fig. 4.7). Note that the leading mode of geopotential height at 500 hPa (Fig. 4.9, middle) explains the least amount of variance compared to the leading modes at the surface (Fig. 4.9, top) and 200 hPa (Fig. 4.9, bottom). This result appears consistent with the weaker signatures found in the response patterns in the geopotential height field in the middle troposphere (Fig. 4.7, middle column). Given that previous studies have found similar relationships (e.g, Hoerling et al. 2004; Deser et al. 2004, 2007; Nakamura et al. 2008; Ogawa et al. 2016; Seo et al. 2017), it is not entirely unexpected that the atmospheric response to anomalous ocean forcing projects onto the leading internal modes of variability. *However, it is unexpected that the atmospheric circulation response is seemingly independent of the latitudinal placement of the SST anomaly.*

In numerical experiments by Deser et al. (2004, 2007), the authors found that the total response to SST anomalies in the North Atlantic could be decomposed into two separate response patterns: an indirect response that projects onto the leading mode of internal variability and a direct response defined as the residual from the projection. Results from their transient experiments suggested that the latter response relates to an initial baroclinic adjustment of the linear response to SST and sea ice anomalies in the North Atlantic, while the other relates to the stronger, barotropic equilibrium response that resembles the NAM/NAO pattern (e.g., Deser et al. 2007). In the following sections, a similar approach is applied to the idealized results found here, by decomposing the steady-state atmospheric response patterns to analyze the signature of internal variability as well as any signature of a direct response that might arise in the evolution of the local atmospheric circulation to a sudden "switch-on" of heating.

4.4.2 Decomposing the Steady-State Atmospheric Response

A spatial linear decomposition is applied to identify the features of the steady-state atmospheric response from the 1K20N, 1K45N, 1K60N, and 1K90N perturbation experiments that are linearly associated with the leading mode of model (atmospheric) internal variability. To do this, a cosine-weighted projection of the steady-state response pattern onto EOF1 is performed to calculate a "spatial" regression coefficient, as explained in more detail in

Section 2.2.2.4. Essentially, with this method, the part of the atmospheric response in each perturbation experiment that is linearly associated with the leading mode of internal variability is constrained to be identical in structure to EOF1, only varying in amplitude between the experiments. The residual response is then calculated as the remainder of the full response pattern. Thus, the spatial linear decomposition can be viewed as isolating the component of the total response field that is linearly congruent with the pattern of leading internal variability and the residual component.

The decomposition is performed for the anomalous SLP and Z_{200} fields, as seen in Figures 4.10 and 4.11, respectively. The middle column of Fig. 4.10 shows the projections of the anomalous SLP patterns onto the associated EOF1 pattern. At a glance, it is clear that the signature of the steady-state SLP response associated with the leading mode of internal variability has the same amplitude for all experiments, with a slightly higher amplitude found for 1K20N. A similar result is seen for the Z_{200} projection patterns in the middle column of Fig. 4.11, where the amplitudes are only slightly higher for 1K45N and 1K60N. The right columns of Figs. 4.10 and 4.11 show the residual component of the response that is linearly unrelated to the EOF structure. Based on the residual responses for each perturbation experiment, it is evident that the most prominent and consistent feature associated with the leading mode of atmospheric variability in the lower and upper levels of the troposphere is the pattern of high pressure anomalies over the polar region.

The residual response patterns in Figs. 4.10 and 4.11 appear to resemble remaining atmospheric noise that was otherwise damped by the strong barotropic signal. But at closer inspection, there are some interesting features that were not prominent prior to removing the linearly congruent component. For example, the displaced high pressure feature seen in the full 1K45N response (left column of Figs. 4.10 and 4.11) is confined to the northeast of the SST anomaly in the residual 1K45N response (right column). The residual 1K90N SLP response (Fig. 4.10, top right) also indicates a locally-confined region of low pressure coincident with the SST anomaly at the pole, which is more consistent with the theoretical linear response to diabatic heating (e.g., Hoskins and Karoly 1981). However, without investigating the transient atmospheric response to a sudden "switch-on" of heating, it is difficult to say if the residual responses are reminiscent of a direct linear response, as found by Deser et al. (2004, 2007). Nonetheless, the most robust aspect of the total atmospheric response (i.e., the pattern of circulation anomalies that resemble the leading mode of model internal variability) is generally consistent with the indirect, or equilibrium, response found in their experiments.

4.4.3 Investigating the Steady-State Extratropical Atmospheric Response

As noted in the previous section, numerical simulations from idealized aquaplanet experiments reveal a consistent, equivalent barotropic dipolar pressure response of the same sign and amplitude to extratropical SST anomalies imposed at 20°N, 45°N, 60°N, and 90°N. The results indicate that regardless of the latitude of the forcing, the atmospheric circulation response projects onto the model's leading mode of (atmospheric) internal variability, which resembles the low polarity index of an annular mode (e.g., Kidson 1988; Thompson and Wallace 1998, 2000; Limpasuvan and Hartmann 1999; Lorenz and Hartmann 2001). Previous studies have found similar sensitivity in the characteristics of the observed leading modes of variability (such as the annular modes and the NAO/PNA patterns) to variations in the location and strength of SST fronts (e.g., Nakamura et al. 2008; Frankignoul et al. 2011; Taguchi et al. 2012; Ogawa et al. 2016; Seo et al. 2017). It is argued that anomalous SST gradients (i.e., associated with a SST anomaly) lead to changes in lower-tropospheric baroclinicity that in turn influences the strength and position of the midlatitude storm track and eddy-driven jet (e.g., Brayshaw et al. 2008; Michel and Riviére 2014). Meridional shifts in the location of the eddy-driven jet, or the maximum of midlatitude westerlies, can then excite changes in the polarity of the annular mode.

Figure 4.12 shows the prescribed SST anomalies (contours) superposed onto the climatological-mean zonal wind at 700 hPa (shading) over the model northern hemisphere.

The results indicate that the maximum midlatitude westerlies (and the climatological-mean baroclinic zone) are located approximately around 45°N. Based on the argument presented above, it is expected that heating on the poleward side of the climatological-mean baroclinic zone reduces lower tropospheric baroclinicity, leading to an equatorward shift of the eddy-driven jet. Heating on the equatorward side of the climatological-mean baroclinic zone is expected to enhance the lower tropospheric baroclinicity, leading to a poleward shift of the eddy-driven jet (e.g., Brayshaw et al. 2008; Nakamura et al. 2008; Michel and Riviére 2014; Baker et al. 2017). However, this does not appear to be the case for the 1K20N SST perturbation experiment. In fact, despite the location of thermal forcing relative to the eddy-driven jet, the results in Fig. 4.13 indicate a general equatorward shift of the midlatitude westerlies for all extratropical SST perturbations. While the equatorward shift of the midlatitude westerlies is consistent with the low polarity phase of the annular mode response (i.e., Fig. 4.7), it is unclear as to why the *sign* of the atmospheric circulation response is insensitive to the latitude of heating in the extratropical experiments.

Earlier studies suggest that the large-scale atmospheric response is highly sensitive to the position of SST anomalies (and their gradients) relative to both the subtropical and eddy-driven jets (e.g., Brayshaw et al. 2008; Nakamura et al. 2008; Michel and Riviére 2014; Baker et al. 2017). In particular, eddy-driven jet variability is largest when anomalous heating occurs inside and on the equatorward flank of the jet core (e.g., Baker et al. 2017). In addition to the expected changes in lower tropospheric baroclinicity, Brayshaw et al. (2008) found that when the location of the SST gradient anomaly is very close to the subtropical jet, the Hadley cell and subtropical jet strengthen, but the midlatitude storm track and eddy-driven jet shift equatorward. While the 1K20N SST anomaly is located very close to the latitude of the simulated subtropical jet (~25° in each hemisphere; see Fig. 4.1), the results in the bottom panel of Fig. 4.14 indicate a weakening of the northern Hadley cell and subtropical jet in response to thermal forcing at 20°N. In contrast, the 1K45N, 1K60N, and 1K90N experiments all indicate a strengthening of the tropically-driven component of the Hadley cell and subtropical jet in the northern hemisphere. Hence, it is possible that different mechanisms are responsible for the equatorward shift in the eddy-driven jet, which in turn excites the low index annular mode response.

Given that the prescribed extratropical SST anomalies preferentially (and infinitely) heat one hemisphere, it is possible that the consistent sign of the atmospheric circulation response occurs as the atmosphere adjusts to correct the energy imbalance between the model's northern and southern hemispheres. Studies have found that an energy imbalance between the two hemispheres requires a shift in heat transport across the equator to maintain energy balance, typically leading to a cross-equatorial shift in the Intertropical Convergence Zone (ITCZ) (e.g., Kang et al. 2008, 2009; White et al. 2018). In aquaplanet experiments coupled to a slab ocean by Kang et al. (2008, 2009), hemispherically-asymmetric heating of the extratropics between the cooled northern hemisphere and warmed southern hemisphere resulted in a shift of the ITCZ towards the warmed hemisphere, leading to a strengthening (weakening) of the northern (southern) Hadley cell. The authors postulate that the Hadley circulation responds to transport energy northward (i.e., toward the cooled hemisphere) and balance the total energy flux near the edge of the tropics in both hemispheres, as seen in the schematic in Fig. 4.15 reproduced from Kang et al. (2009). It is hypothesized that equatorward eddy energy fluxes in the warmed hemisphere act to cool and warm the southern extratropics and subtropics, respectively, leading to a northward distribution of warming by the anomalous Hadley circulation. The equatorward eddy energy fluxes would also act to shift the storm track and eddy-driven jet equatorward, leading to a low index annular mode response in the warmed hemisphere. The opposite response occurs in the cooled hemisphere, where poleward eddy energy fluxes act to warm the northern extratropics and shift the storm track and eddy-driven jet poleward, leading to a high index annular mode response.

Figure 4.16 shows the simulated steady-state atmospheric response over the southern hemisphere for the 1K20N, 1K45N, 1K60N, and 1K90N experiments. Following the energy imbalance argument presented by Kang et al. (2008, 2009), the large-scale atmospheric circulation response to hemispherically-asymmetric extratropical heating should display signatures in both hemispheres due to a cross-equatorial shift of the Hadley circulation. While the results indicate a large-scale circulation response to thermal forcing imposed in the northern hemisphere, the anomalous circulation pattern in the southern hemisphere is generally reminiscent of the low polarity phase of the annular mode. The results in Fig. 4.14 also suggest that there is no cross-equatorial shift of the Hadley circulation to balance the hemispherically-asymmetric heating. These discrepancies are likely due to differences in experimental design, as the present aquaplanet experiments are not coupled to a slab ocean, preferentially heat one hemisphere, and do not include a net area-averaged heating anomaly. Given these differences, the following (modified) hypothesis is proposed:

1. In the absence of an ocean circulation, equatorward eddy energy fluxes in the northern (i.e, warmed) hemisphere act to cool the northern extratropics, warming the edge of the northern subtropics.
2. To balance the warming in the northern hemisphere, equatorward eddy energy fluxes in the southern (i.e., neutral) hemisphere act to cool the southern extratropics, warming the edge of the southern subtropics.
3. Anomalous warming on the edge of the subtropics is distributed throughout the tropics, enhancing the tropically-driven component of the Hadley cell and strengthening the ITCZ along the equator.

A strengthening, rather than a cross-equatorial shift, of the ITCZ is found to occur for the 1K45N, 1K60N, and 1K90N SST experiments (e.g., Fig. 4.17), consistent with the above hypothesis. Unfortunately, the ITCZ results from the 1K20N SST experiment are less clear, as the steady-state precipitation response in the bottom right panel of Fig. 4.17 indicates locally-confined regions of increased and decreased precipitation coincident with and equatorward of the heating at 20°N, respectively. While the 1K20N results warrant further investigation, it appears that the consistent sign of the atmospheric circulation response for all extratropical SST experiments is associated with an equatorward shift of the midlatitude westerlies in both hemispheres, leading to the consistent annular mode response.

4.5 Transient Evolution of the Atmospheric Response to SST Perturbations

The second set of numerical experiments explores the transient evolution of the atmospheric circulation response to a sudden "switch-on" of surface heating in CAM5.3. The motivation for the transient experiments stems from the observational results presented in Chapter 3, which reveal a consistent pattern of atmospheric circulation anomalies that lag anomalously warm SSTs over the major Northern Hemisphere western boundary currents by ~2 - 3 weeks (e.g., Wills et al. 2016; Wills and Thompson 2018). Given that linear regression does not prove causality, the question remains as to whether or not this observed relationship can be interpreted as the atmospheric response to the midlatitude SST field. Hence, the goal of the transient experiments is to provide a simplified framework for investigating the short-term atmospheric response to SST anomalies across the globe.

As described in Ch. 2, for each SST perturbation experiment, a 100-member ensemble of 100-day integrations was performed using initial conditions derived from the same 10,000-day control simulation. The atmospheric conditions used to initialize each ensemble member are identical across the 1KEQ, 1K20N, 1K45N, 1K60N, and 1K90N perturbation experiments, so that the differences between the simulated climates can only be attributed to the imposition of anomalous heating. Differences are calculated for each "pair" of integrations between the perturbation experiment and the control, thus yielding 100 different realizations of the evolution of the atmospheric circulation response. The ensemble-mean is then calculated by averaging the 100 different realizations on each day of the integration.

Figures 4.18 and 4.19 compare the time-mean ensemble-mean (left columns) anomalies in SLP and Z_{200}, respectively, to those generated by the steady-state experiments (right columns). The time-mean is calculated as the average over days 61 - 100, and the average is considered to represent the quasi-equilibrium state. The results in Figs. 4.18 and 4.19 indicate that the ensemble-mean simulations broadly reproduce the robust large-scale features found in the steady-state simulations for each SST perturbation experiment, with the closest similarities seen in the atmospheric responses to an equatorial SST anomaly (top rows of Figs. 4.18 and 4.19). For the extratropical SST experiments, it is particularly interesting that both the quasi-equilibrium and steady-state results indicate the same sign annular mode response. However, there are some obvious differences in the atmospheric responses. For example, there is a noticeable increase in the amplitudes of the ensemble-mean responses relative to the steady-state responses, and there are apparent structural differences between the ensemble-mean and steady-state circulation responses for 1K45N (to be discussed). Aside from these differences, the equilibrium ensemble-mean SLP and Z_{200} anomalies for 1K20N, 1K45N, 1K60N, and 1K90N indicate an equivalent barotropic hemispheric scale dipole pattern, characterized by positive pressure and geopotential height anomalies over the polar region and negative anomalies over the midlatitudes. Except for 1K45N, the dipolar structure is generally zonally-symmetric.

Given the consistent results between the equilibrium-state and steady-state, it is reasonable to assume that the 100-day ensemble-mean integration can be applied to evaluate the transient evolution of the atmospheric response to the sudden "switch-on" of a SST anomaly. The following sections explore the first 30-day period of the atmospheric responses in each SST perturbation experiment, and additional discussion regarding the 1K45N results is presented. The next section provides an overview of the transient 1KEQ results, followed in the subsequent section by a comparison of the transient 1K20N, 1K45N, 1K60N, and 1K90N results.

4.5.1 Transient Atmospheric Response to an Equatorial Heat Source

The time-varying circulation response to an imposed equatorial heat source is shown in Fig. 4.20, where consecutive 10-day averages of SLP and Z_{200} anomalies are in the top and bottom rows, respectively. Given the simplicity of the aquaplanet configuration, there is a rapid atmospheric adjustment to the input of surface heating, and the remote teleconnection patterns begin to emerge after the first 10 days. During the initial 10-day period, low surface pressure anomalies develop in the vicinity of the forcing region (Fig. 4.20, top left), with a similarly located region of high Z_{200} anomalies (Fig. 4.20, bottom left). These results are consistent with the analytical solutions presented in Heckley and Gill (1984) to the problem of a sudden "switch-on" of equatorial heating. Although the map projection in Fig. 4.20 slightly distorts the pattern, the response resembles the solution to symmetric heating in the presence of dissipative processes, as seen in Fig. 1.2 from Ch.1 of the dissertation. Comparing the top left and top middle panels of Fig. 4.20, the changing patterns of low pressure anomalies indicate a fast, eastward-moving Kelvin wave response to the east of the heating region, in addition to slower, westward-moving Rossby waves to the west of the heating region, as evident in the steady-state results of the 1KEQ perturbation experiment (Fig. 4.3). The Z_{200} anomalies in the bottom right panel of Fig. 4.20 suggest that by the end of the first 30 days, Rossby wave trains have largely developed and propagated away from the forcing region toward the extratropics, following an expected ray path that bends east around the pole (e.g., Hoskins and Karoly 1981; Horel and Wallace 1981).

Figure 4.21 shows the same time-varying circulation anomalies as in Fig. 4.20, but also indicates the associated time-varying THFLX (top row) and 200 hPa temperature (T_{200}; bottom row) anomaly fields (shading). Positive (upward) THFLX anomalies appear in the first 10 days (top left panel of Fig. 4.21), indicating a rapid flux of heat from the surface to the overlying atmosphere in response to the equatorial SST anomaly. Similarly, positive T_{200} anomalies during the first 10 days (bottom left panel of Fig. 4.21) suggest an almost immediate communication of warming from the surface to the upper tropical troposphere through enhanced convective heating above the SST anomaly. As earlier noted in Fig. 4.4 (right panel), the T_{200} anomalies begin to spread remotely to the east of the heat source by the end of the 30-day period, consistent with results from previous studies (Bantzer and Wallace 1996; Lintner and Chiang 2006; Maloney and Sobel 2007).

4.5.2 Comparison of the Transient Atmospheric Response to Heating at Different Latitudes

Unlike the 1KEQ perturbation experiment, the transient evolution of the local atmospheric response was less clear in the 100-member ensemble 1K20N, 1K45N, 1K60N, and 1K90N perturbation experiments, possibly indicating that the transient analyses require a larger sample size of ensemble members for the prescribed 1K extratropical SST anomaly. In fact, similar studies by Ferreira and Frankignoul (2005) and Deser et al. (2007), who explored the transient atmospheric response to SST anomalies in the North Atlantic, performed experiments with 400-member and 240-member ensembles, respectively. While their experiments were performed on slightly to moderately more complex global climate models compared to CAM5.3, the studies also employed SST anomalies that were 3x - 5x larger in amplitude to obtain robust statistics. Despite the simplicity of the aquaplanet model, additional analyses may require a larger sample of ensemble members to discern a statistically significant transient atmospheric response (if any) to the much smaller extratropical SST anomalies used here. Indeed, given the high degree of variability in the extratropical circulation on synoptic time scales, the time-varying results for 1K20N, 1K45N, 1K60N, and 1K90N display large amounts of atmospheric noise, making it difficult to discern any significant direct linear response to the prescribed 1K SST anomalies. Nonetheless, the results presented in Figures 4.22 - 4.25 lend some interesting insights into the transient atmospheric adjustment to a sudden “switch-on” of anomalous surface heating.

Figure 4.22 shows the 30-day evolution of SLP (top row) and Z_{200} (bottom row) anomalies in consecutive 10-day average increments in response to a SST anomaly prescribed at 20°N. Note that the gray contours in the left column (as in all Figs. 4.22 - 4.25) reflect a smaller contour spacing to highlight the features associated with the initial atmospheric adjustment. Similar to the findings in Deser et al. (2007), and consistent with the theoretical linear response to diabatic heating (e.g., Hoskins and Karoly 1981), the results in Fig. 4.22 indicate the development of an initial local baroclinic circulation, with low SLP anomalies coincident with the region of anomalously warm SSTs and high Z_{200} anomalies situated slightly to the northeast. A similar baroclinic adjustment is also seen in the initial 10-day average response to diabatic heating at 45°N, as shown in the left column of Fig. 4.23. In fact, the atmospheric circulation response maintains a seemingly baroclinic structure for the longest period of time compared to 1K20N, 1K60N, and 1K90N (e.g., Figs. 4.22, 4.24 - 4.25). While there is also a slight indication of an initial baroclinic response in the 1K60N perturbation experiment, both 1K60N and 1K90N (Figs. 4.24 and 4.25, respectively) displayed the weakest transient circulation anomalies in the first 10 days following the the "switch-on" of surface heating.

The more salient and consistent feature of the transient atmospheric evolution in all four extratropical SST experiments is characterized by the progressive development of equivalent barotropic circulation anomalies that extend in size and amplitude across the model northern and southern (not shown) hemispheres. This barotropic adjustment is consistent with the indirect/equilibrium response found by Deser et al. (2004, 2007) and the remote extratropical circulation response found in similar experiments on Indian Ocean warming by Hoerling et al. (2004). Even with the amount of background noise, the equilibrium pattern associated with the leading mode of internal variability begins to emerge by the end of the 30-day period, obtaining a quasi-equilibrium state after ~ 2 months (e.g., Figs 4.18 and 4.19) for all experiments except 1K45N, which displays a more Rossby wave-like response. The following section focuses on the results from the 1K45N SST experiments, and a possible link to the observed relationships found in Chapter 3 is discussed.

4.5.3 Investigating the 1K45N Experiments

While the extratropical SST perturbation experiments reveal a consistent, equivalent-barotropic large-scale atmospheric response to surface thermal forcing, the 1K45N results are particularly interesting given 1) the location of the SST anomaly relative to the core of the westerly jet (e.g., Fig. 4.12), 2) the difference between the equilibrium ensemble-mean and steady-state circulation responses (e.g., Figs 4.18 and 4.19), and 3) the seemingly persistent initial baroclinic response to a sudden "switch-on" of surface heating (e.g, Fig. 4.23). As mentioned earlier, previous studies have found that the large-scale atmospheric response is highly sensitive to the position of SST anomalies relative to the location of the subtropical and eddy-driven jets, especially when anomalous heating occurs inside the jet core (e.g., Brayshaw et al. 2008; Baker et al. 2017). Noting that the prescribed heating at 45°N is roughly coincident with the simulated core of the westerly jet (e.g., Fig. 4.12), the discrepancy between the Rossby wave-like equilibrium pattern and the zonally-symmetric steady-state pattern may be due to large variability in the response of the eddy-driven jet.

Given the different time scales between the equilibrium and steady-state averages, it is possible that the "zonally-symmetric" result from the steady-state 1K45N experiment reflects 1) the atmospheric adjustment to hemispherically-asymmetric heating and/or 2) an average of short-term, longitudinally-varying Rossby wave responses. To test the latter hypothesis, 100 individual composite members were taken from the 10,000-day output for 1K45N to assess the variability of the long-term atmospheric response. Each composite member is averaged over a 50-day period, and consecutive members are separated by a time span of 50 days. Based on the results in Figure 4.26, which highlight SLP anomalies for a select set of 25 composite members (i.e., every fourth member), it is evident that the "individual" atmospheric responses display a more chaotic and wave-like pattern on shorter time scales. Hence, it appears that the 1K45N ensemble-mean equilibrium pattern may reflect a more local and transient atmospheric response to surface thermal forcing at 45°N that otherwise averages (or damps) out in the long-term mean.

There are also apparent similarities between the simulated ensemble-mean atmospheric response and the observed relationships over the North Atlantic (e.g., Wills et al. 2016) in Ch. 3. The top row of Fig. 4.27 highlights the ensemble-mean atmospheric response in the vicinity of the 1K45N SST anomaly. The results in the top left panel of Fig. 4.27 display a similar dipolar SLP structure as that found lagging anomalously warm SSTs over the Gulf Stream Extension by a few weeks (e.g., Fig. 3.8, bottom right panels). While the low SLP anomalies are centered to the west of the prescribed heating in the ensemble-mean, the transient simulations are able to reproduce the more robust, downstream high SLP feature found in observations. The results in the top right panel of Fig. 4.27, which show the anomalous θ_{850} (shading) and Z_{500} (contours) fields, also indicate the development of a downstream, equivalent barotropic high pressure feature similar to that found over the North Atlantic (e.g., Fig. 3.9, bottom). Based on these similarities, it is possible that the transient 1K45N results have some bearing on the observed relationships between SST anomalies in the Gulf Stream Extension region and the overlying atmospheric circulation.

The bottom panel of Fig. 4.27 shows the zonal-mean potential temperature (shading), zonal wind (contours), and meridional and vertical wind (vectors) anomalies averaged over the cross-section 30°W - 30°E for the 1K45N ensemble-mean experiment. Similar to the North Atlantic observations in Fig. 3.11, the transient results indicate that following the sudden "switch-on" of anomalous surface heating, positive temperature anomalies extend vertically into the upper levels of the free troposphere. The positive temperature anomalies are accompanied by anomalous upward and poleward motion to the north of the heat source, also consistent with the observational results presented in Fig. 3.11. Interestingly, the ensemble-mean zonal wind anomalies found in Fig. 4.27 suggest both a strengthening and poleward shift of the eddy-driven jet in response to the prescribed heating at 45°N. This result is in contrast to the 1K45N steady-state results, which indicate an equatorward shift of the eddy-driven jet in response to the anomalous heat source (e.g., Fig. 4.13, bottom left panel). While the differences between the transient and steady-state atmospheric circulation results likely reflect large variability in the eddy-driven jet response (e.g., Brayshaw et al. 2008; Michel and Riviére 2014; Baker et al. 2017), it is possible that different physical processes dominate the atmospheric response on shorter versus longer timescales.

4.6 Conclusions

A series of idealized numerical experiments were performed on the NCAR Community Atmosphere Model (CAM5.3) using a simple aquaplanet configuration to explore the role of ocean forcing on the atmospheric circulation across the globe. Fixed SSTs were applied to the atmosphere-only model, meaning that the SST field prescribed at the lower boundary of the model is unchanging in time (i.e., an infinite heat source), eliminating feedbacks from the atmosphere to the ocean layer. Steady-state and ensemble-mean experiments were performed to evaluate both the time-mean and evolution of the atmospheric circulation response to a sudden "switch-on" of anomalous surface heating at varying latitudes across the model northern hemisphere. Five SST perturbation experiments were designed in which the fixed SST anomaly (or infinite heat source) was imposed onto a zonally-symmetric background SST profile and placed at latitudes of 0°, 20°N, 45°N, 60°N, and 90°N (i.e., the 1KEQ, 1K20N, 1K45N, 1K60N, and 1K90N perturbation experiments, respectively).

Beginning with results from the 1KEQ perturbation experiment, the aquaplanet model generated a robust tropical atmospheric circulation and remote teleconnections in response to an equatorial SST anomaly that is consistent with linear theory (e.g., Gill 1980; Hoskins and Karoly 1981; Horel and Wallace 1981; Lindzen and Nigam 1987; Chiang et al. 2001; Alexander et al. 2002; Back and Bretherton 2009). While the results largely reproduced the expected key features, they also provided insight into the potentially combined and/or competing roles of elevated heating and surface temperature gradients in forcing the local steady-state atmospheric response to an infinite heat source on the equator. Results from the transient experiments were largely consistent with the analytical solutions found by

Heckley and Gill (1984), in which the problem of a sudden "switch-on" of heating is solved by the development of a fast-moving, eastward-propagating Kelvin wave, which in turn acts to quickly redistribute the anomalous warming throughout the upper tropical troposphere (e.g., Bantzer and Wallace 1996; Lintner and Chiang 2006; Maloney and Sobel 2007).

Numerical analyses of the steady-state and transient 1K20N, 1K45N, 1K60N, and 1K90N perturbation experiments also yielded key results, where the steady-state and equilibrium atmospheric circulation response to an imposed SST anomaly projected onto the leading mode of the model's internal variability. EOF analyses on the model northern and southern hemispheres revealed a leading mode of variability reminiscent of an annular mode, as observed in the real climate of the Earth. In fact, given the reduced amount of land in the Southern Hemisphere on Earth, there are some interesting similarities in the characteristic structures of variability found in the aquaplanet simulations and the Southern Annular Mode (SAM) (e.g., Kidson 1988; Thompson and Wallace 2000; Lorenz and Hartmann 2001). These results are consistent with previous numerical studies that suggest variations in the strength and position of oceanic frontal zones (associated with SST gradients) can indirectly impact variations in the annular modes, such as the NAM and the SAM, as well as the more regional modes of atmospheric variability, such as the NPO (North Pacific Oscillation), NAO, and PNA, through their influence on the strength and position of the atmospheric storm tracks and eddy-driven jets (e.g., Nakamura et al. 2008; Frankignoul et al. 2011; Taguchi et al. 2012; Ogawa et al. 2016; O'Reilly et al. 2017; Seo et al. 2017). Similar transient experiments by Deser et al. (2007) and Hoerling et al. (2004) also indicated that the extratropical atmospheric response to SST anomalies in the North Atlantic and Indian Oceans, respectively, project onto a pattern reminiscent of the NAO.

The unexpected result from the steady-state experiments presented here is the seemingly consistent, hemispheric-scale equivalent barotropic response to a realistically sized SST anomaly at each of the four extratropical latitudes (i.e., 20°N, 45°N, 60°N, and

90°N). As noted in this chapter, the response projects onto the low polarity index of the leading mode of atmospheric variability, which is characterized by a zonally-symmetric out-of-phase dipole pattern of high pressure over polar latitudes and low pressure over midlatitudes (e.g., Fig. 4.9). The similar sign and amplitude of the atmospheric response for all extratropical experiments (e.g., Figs. 4.10 - 4.11) is inconsistent with findings from previous studies that suggest anomalous heating on the equatorward side of the midlatitude storm track (i.e., 1K20N) leads to a poleward shift of the eddy-driven jet (e.g., Brayshaw et al. 2008; Nakamura et al. 2008; Michel and Riviére 2014; Baker et al. 2017); a poleward shift of the eddy-driven jet is associated with the high polarity index of the annular mode response (e.g., Kidson 1998; Thompson and Wallace 1998, 2000; Limpasuvan and Hartmann 1999). However, the numerical results suggest that, at least in a highly idealized environment, there is no apparent dependence on the latitude of the SST anomaly. As discussed in Section 4.4.3, it is possible that the extratropical steady-state results reflect the large-scale atmospheric circulation adjustment to an energy imbalance between the northern and southern hemispheres (e.g., Kang et al. 2008, 2009; White et al. 2018). Given that the extratropical SST experiments preferentially and infinitely heat the model's northern hemisphere, hemispherically-asymmetric heating potentially leads changes in the Hadley and Ferrel Cells (e.g., Figs. 4.14 - 4.15) that are seemingly associated with an equatorward shift of the eddy-driven jet in both hemispheres, resulting in the consistent low polarity annular mode response (e.g., Figs. 4.7 and 4.16).

Unlike the other extratropical SST perturbation experiments, the 1K45N ensemble-mean results yielded a more Rossby wave-like atmospheric response pattern compared to the steady-state results (e.g., Figs. 4.18 - 4.19). The differences between the equilibrium and steady-state atmospheric responses may be due to the location of the anomalous surface heating relative to the core of the simulated eddy-driven jet, which is roughly coincident with the forcing prescribed at 45°N (e.g., Fig. 4.12). Previous studies suggest that variability of the eddy-driven jet response is largest for anomalous heating within the core and on the equatorward flank of the eddy-driven jet (e.g., Brayshaw et al. 2008; Michel and Riviére 2014; Baker et al. 2017). It is possible that the contrasting results between the steady-state and transient 1K45N experiments simply reflect large variability of the eddy-driven jet response to thermal forcing at 45°N. However, there are some interesting similarities between the transient 1K45N results and the lagged atmospheric circulation response found in observational analyses for the North Atlantic sector. For example, the numerical results reproduce the local, downstream equivalent-barotropic high pressure feature that lags anomalously warm SSTs over the Gulf Stream Extension region by a few weeks (e.g., Figs. 3.8 - 3.9, 4.27). In addition, the 1K45N equilibrium response indicates a strengthening and poleward shift of the eddy-driven jet, consistent with findings from previous studies (e.g., Brayshaw et al. 2008; Nakamura et al. 2008; Sampe et al. 2010). Hence, it is likely that the ensemble-mean results reflect a more local and transient atmospheric circulation response to SST anomalies located near the storm track and eddy-driven jet, while the steady-state results may reflect the long-term atmospheric circulation adjustment to balance hemispherically-asymmetric heating.

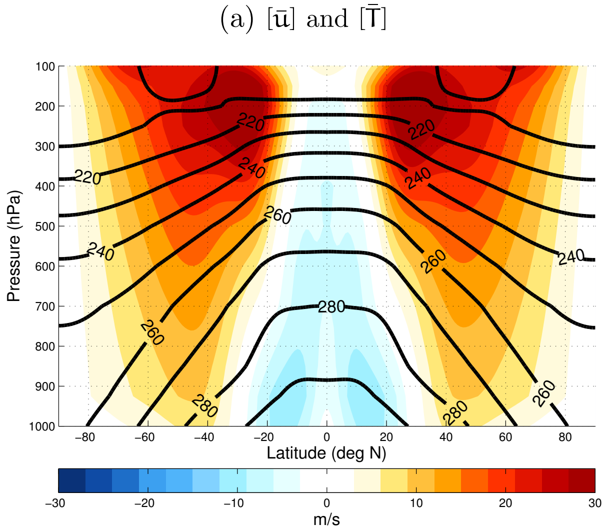

(a) $[\bar{u}]$ and $[\bar{T}]$

Figure 4.1. Steady-state zonal-mean zonal wind ($[\bar{u}]$; shading) and temperature ($[\bar{T}]$; contours) from the 10,000-day control run. Note that contour labels are in units of Kelvin.

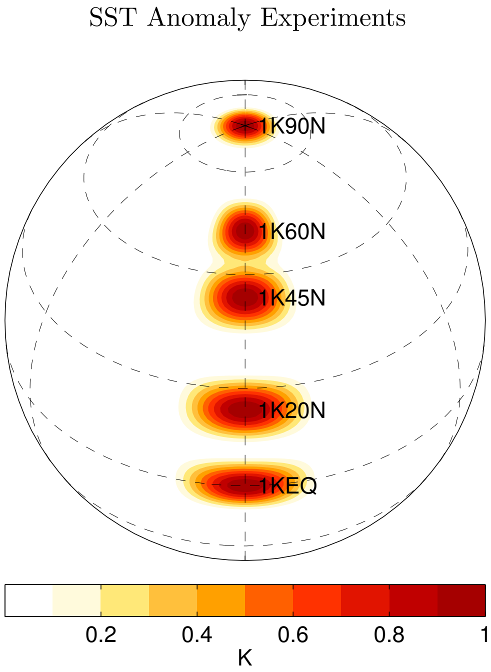
SST Anomaly Experiments

Figure 4.2. Prescribed 1K SST anomalies for the five perturbation experiments. The fixed SST anomalies are imposed at latitudes of 0°, 20°N, 45°N, 60°N, and 90°N, as labeled.

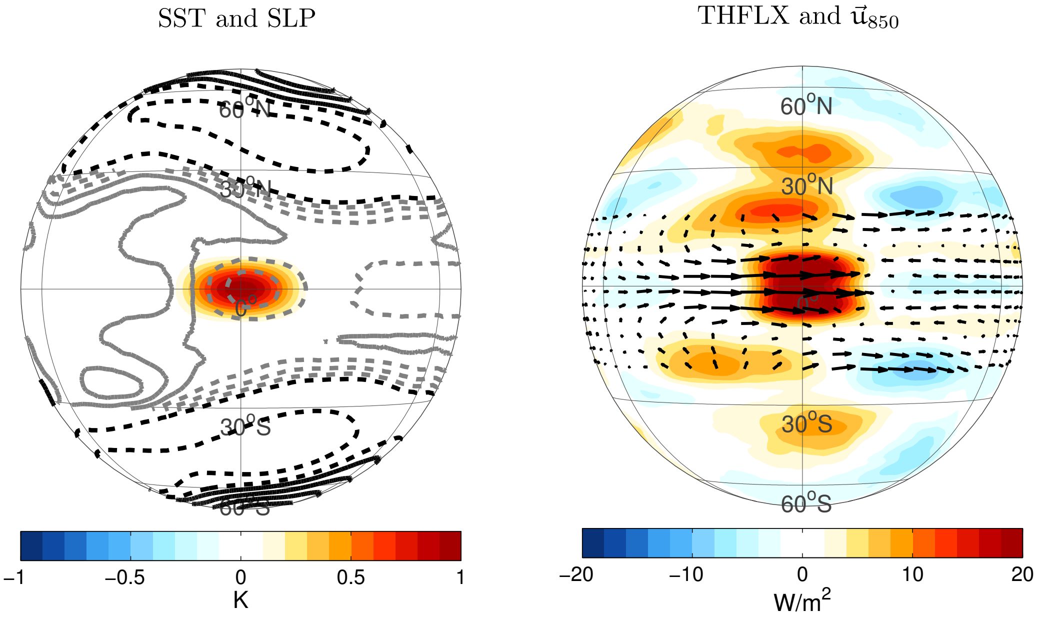

Figure 4.3. Steady-state differences in left) SLP (contours), SST (shading), and right) THFLX (shading) and $\vec{u}_{850}$ (vectors) for the 1KEQ perturbation experiment. Solid (dashed) lines indicate positive (negative) values, and black contours are spaced at 1 hPa. Additional SLP contours (gray lines) are inserted between 30°S - 30°N at an interval spacing of 0.1 hPa (-0.15, -0.05, 0.05, 0.15...hPa), and the contour succession is (...$|0.15|, |0.25|, |0.35|, |1.35|$...hPa), with the first black contour at the separation between gray and black contours corresponding to $|0.35|$ hPa. Note that THFLX output is positive upward.

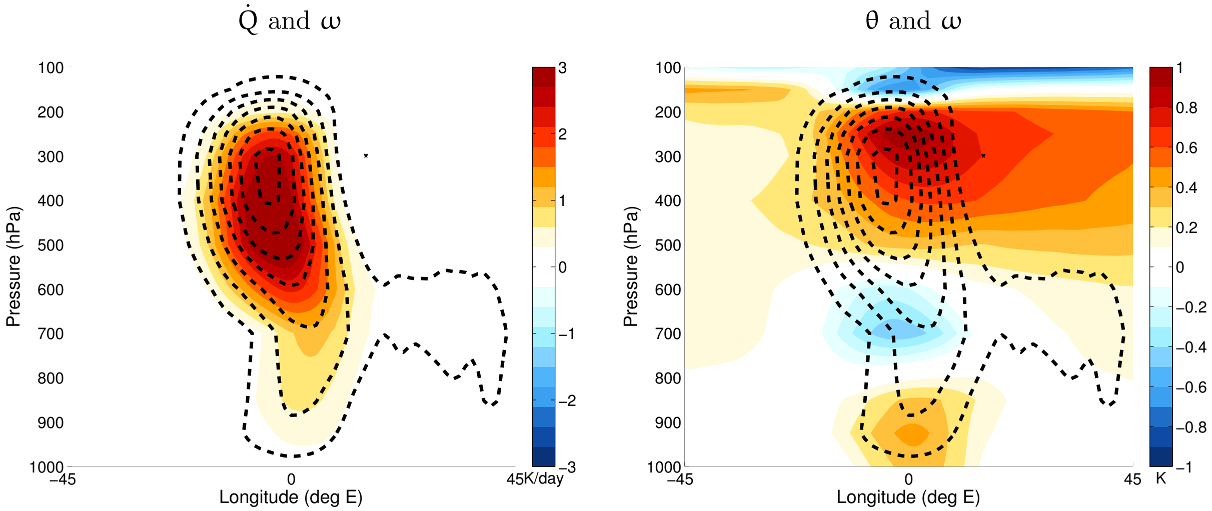

Figure 4.4. Vertical cross-sections of the steady-state differences in vertical velocity (contours; hPa/day) and (left) diabatic heating ($\dot{Q}$; shading) and (right) potential temperature (θ; shading) averaged over 5°S - 5°N. Solid (dashed) lines indicate positive (negative) values, and contours are spaced at 10 hPa/day (-15, -5, 5, 15...hPa/day).

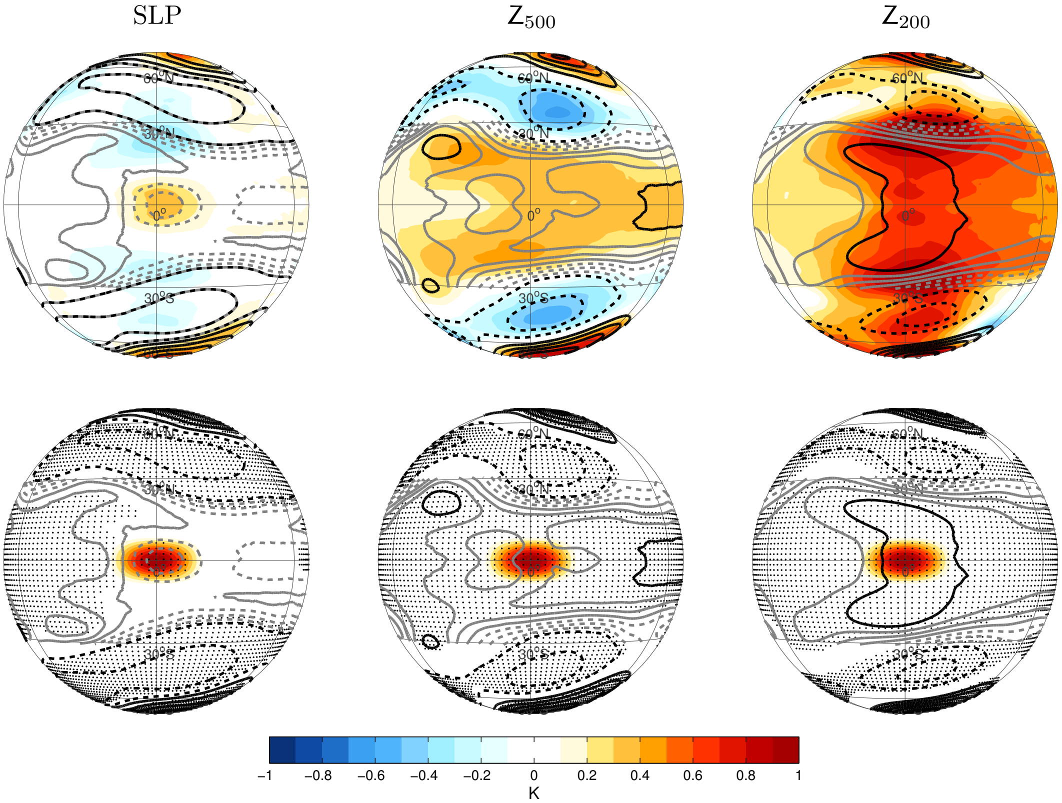

Figure 4.5. (top row) Steady-state differences in (left) θ_{850} (shading) and SLP (contours), (middle) θ_{500} (shading) and Z_{500} (contours), and (right) θ_{200} (shading) and Z_{200} (contours) for the 1KEQ perturbation experiment. Solid (dashed) lines indicate positive (negative) values. SLP contours are the same as in Fig. 4.3; the black Z_{500} and Z_{200} contours are spaced at 4 and 8 meter intervals, respectively. Additional Z_{500} and Z_{200} contours (gray lines) are inserted between 30°S - 30°N at 1 meter (-1.5, -0.5, 0.5, 1.5...m) and 4 meter (-6, -2, 2, 6...m) intervals with contour successions of $(\ldots|1.5|, |2.5|, |3.5|, |7.5|\ldots\text{m})$ and $(\ldots|6|, |10|, |14|, |22|\ldots\text{m})$, respectively. The first black Z_{500} (Z_{200}) contour at the separation between gray and black contours corresponds to $|3.5|$ ($|14|$) meters. (bottom row) Same circulation anomalies as in the top row, but overlaid on SST anomalies with stippling added where the average SLP, Z_{500}, and Z_{200} differences are statistically significant at the 95% confidence level using a two-tailed Student's *t* test. Degrees of freedom are calculated per Eq. (31) from Bretherton et al. (1999), as described in the methods section.

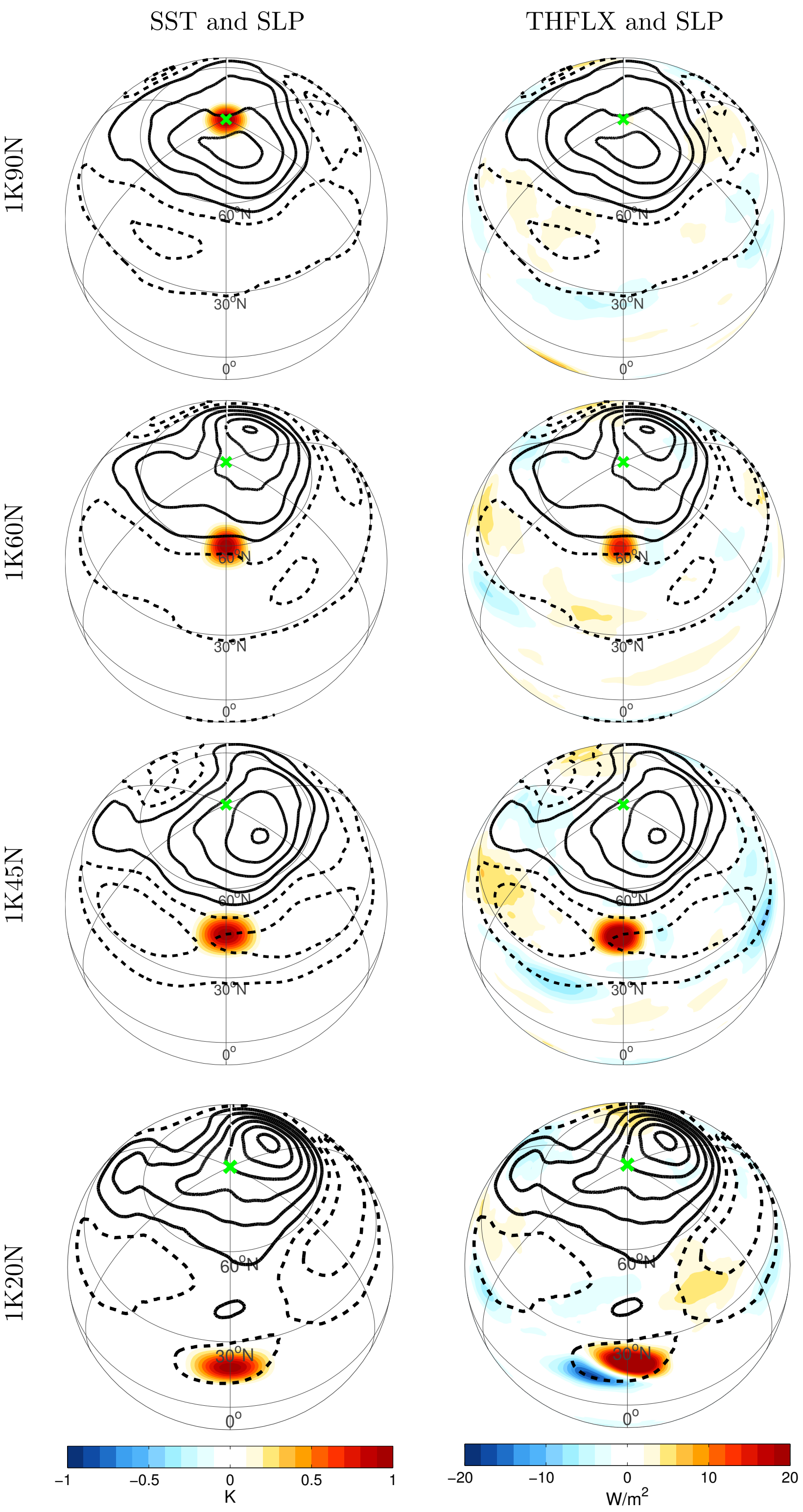

Figure 4.6. Steady-state differences in SLP (contours; both columns), SST (shading; left column), and THFLX (shading; right column) for the 1K20N, 1K45N, 1K60N, and 1K90N perturbation experiments. Solid (dashed) lines indicate positive (negative) values, and black contours are spaced at 0.5 hPa (-0.75, -0.25, 0.25, 0.75...hPa) for all experiments. The green X denotes the location of the northern pole on each grid.

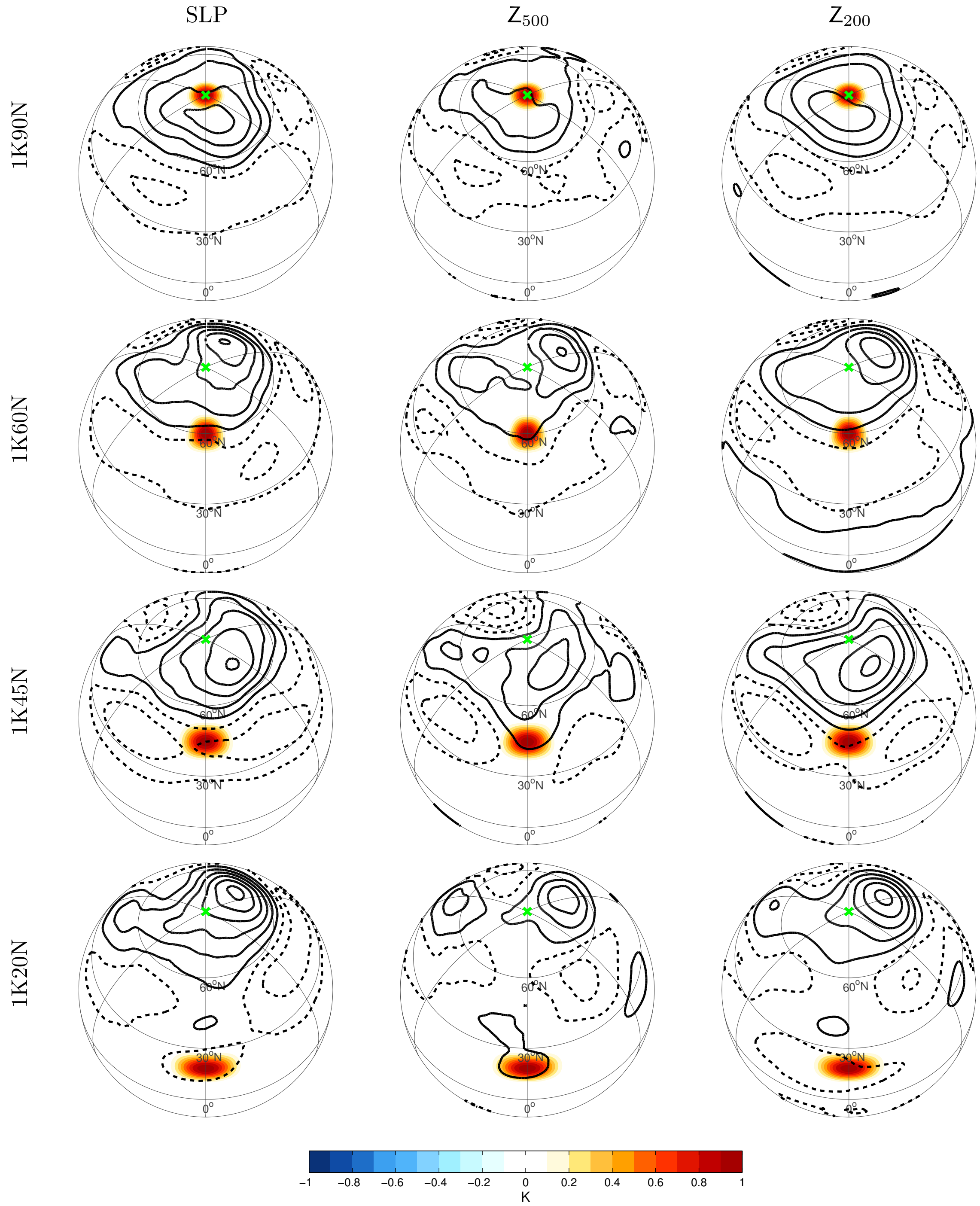

Figure 4.7. Steady-state differences in SST (shading; all columns), SLP (contours; left column), Z_{500} (contours; middle column), and Z_{200} (contours; right column) for the 1K20N, 1K45N, 1K60N, and 1K90N perturbation experiments. Solid (dashed) lines indicate positive (negative) values. SLP contours are the same as in Fig. 4.6; Z_{500} and Z_{200} contours are in 3 meter (-4.5, -1.5, 1.5, 4.5...m) and 6 meter (-9, -3, 3, 9...m) intervals, respectively, for all experiments. The green X denotes the location of the pole on each grid.

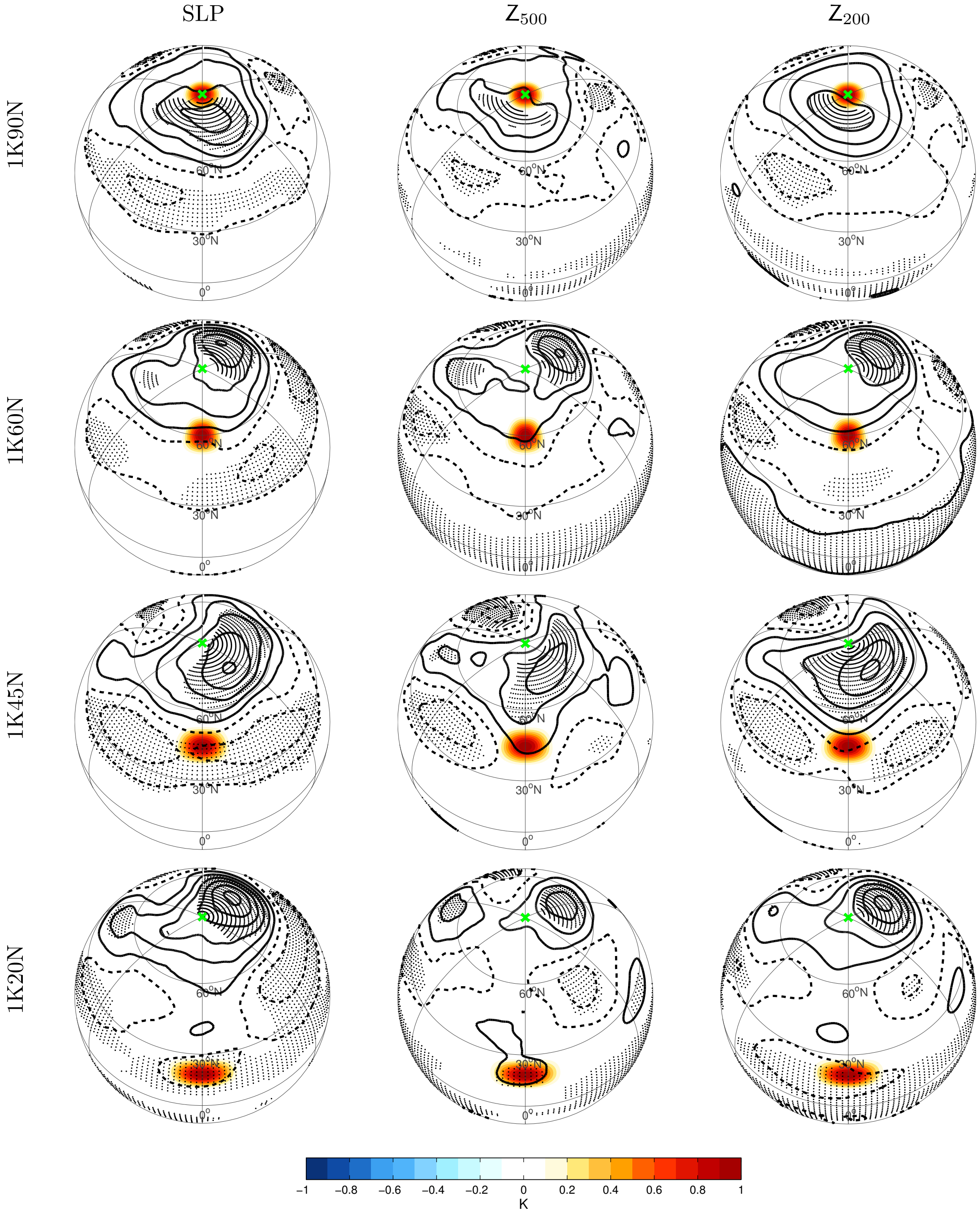

Figure 4.8. Same as in Fig. 4.7, except stippling is added where the average SLP (left column), Z_{500} (middle column), and Z_{200} (right column) differences are statistically significant at the 95% confidence level using a two-tailed Student's *t* test. Degrees of freedom are calculated per Eq. (31) from Bretherton et al. (1999), as described in the methods section. The green X denotes the location of the pole on each grid.

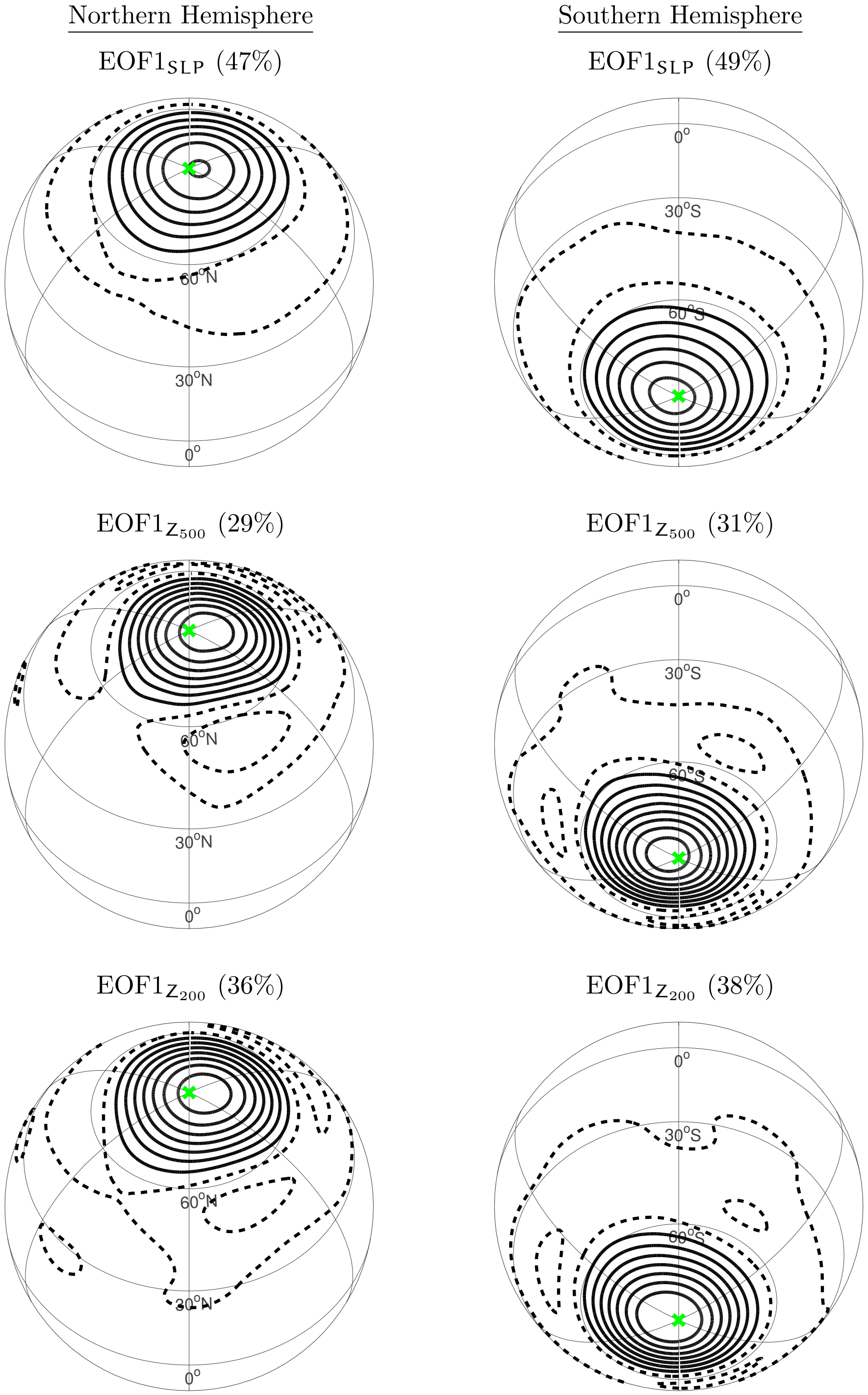
Northern Hemisphere

Southern Hemisphere

EOF1$_{\mathsf{SLP}}$ (47%)

EOF1$_{\mathsf{SLP}}$ (49%)

EOF1$_{\mathsf{Z}_{500}}$ (29%)

EOF1$_{\mathsf{Z}_{500}}$ (31%)

EOF1$_{\mathsf{Z}_{200}}$ (36%)

EOF1$_{\mathsf{Z}_{200}}$ (38%)

Figure 4.9. The leading EOF (or EOF1) of monthly-mean averaged SLP (top), Z_{500} (middle), and Z_{200} (bottom) anomalies in the 10,000-day control simulation over the Northern (left column) and Southern (right column) Hemispheres. Solid (dashed) lines indicate positive (negative) values. SLP contours are spaced at 2 hPa (-3, -1, 1, 3...hPa) intervals, Z_{500} contours are spaced at 6 meter (-9, -3, 3, 9...m) intervals, and Z_{200} contours are spaced at 15 meter (-22.5, -7.5, 7.5, 22.5...m) intervals. The first principal component is computed for each variable separately and accounts for approximately 25%−45% of the variance depending on level. The green X denotes the location of the pole on each grid.

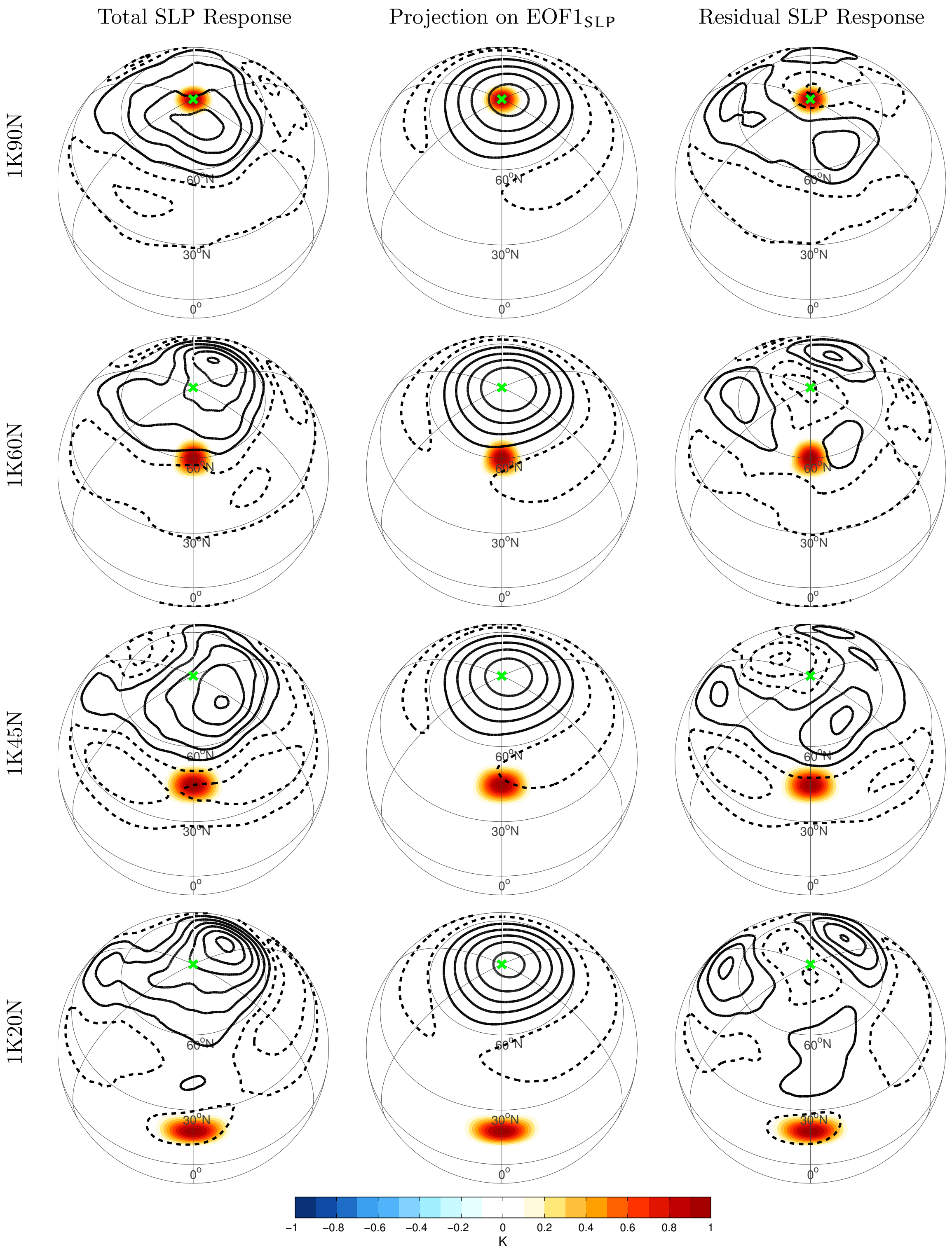

Figure 4.10. (left column) Steady-state differences in SLP, (middle column) linear fit of the total SLP response to EOF1$_{SLP}$ (i.e., the model's leading mode of atmospheric variability), and (right column) the residual SLP response for the 1K90N, 1K60N, 1K45N, and 1K20N perturbation experiments. The total SST difference (shading) for each perturbation experiment is shown in all columns. Solid (dashed) lines indicate positive (negative) values, and black contours are spaced at 0.5 hPa (-0.75, -0.25, 0.25, 0.75...hPa) for all experiments. The green X denotes the location of the northern pole on each grid.

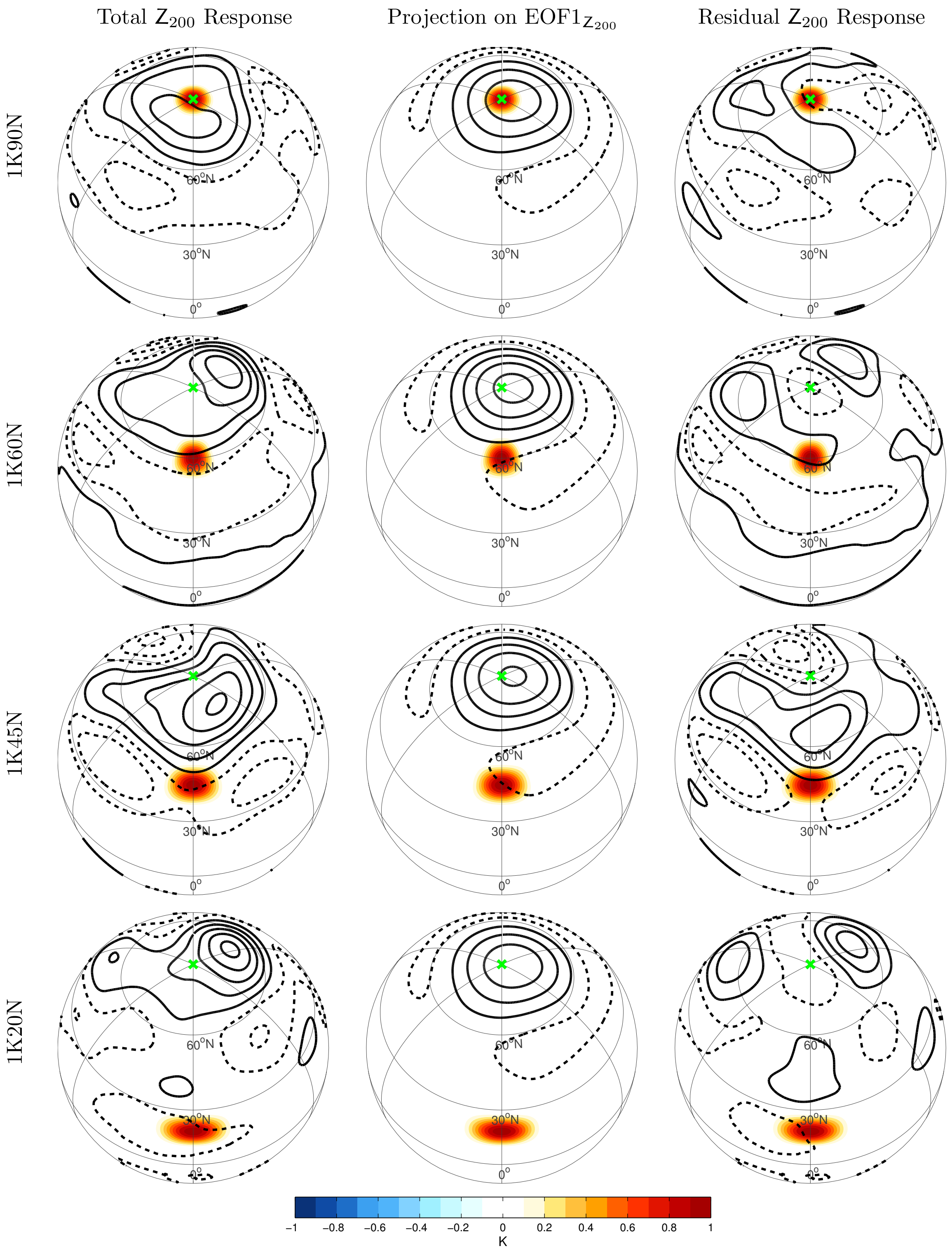

Figure 4.11. (left column) Steady-state differences in Z_{200}, (middle column) linear fit of the total Z_{200} response to $EOF1_{Z_{200}}$, and (right column) residual Z_{200} response for the 1K90N, 1K60N, 1K45N, and 1K20N perturbation experiments. The total SST difference (shading) for each perturbation experiment is shown in all columns. Solid (dashed) lines indicate positive (negative) values, and black contours are spaced at 6 meters (-9, -3, 3, 9...m) for all experiments. The green X denotes the location of the northern pole on each grid.

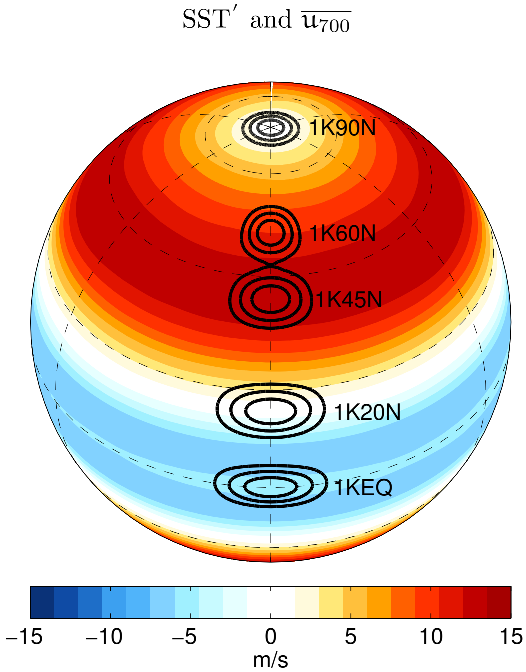

Figure 4.12. Prescribed 1K SST anomalies for the five perturbation experiments overlaid on the climatological-mean zonal wind at 700 hPa ($\overline{u_{700}}$). The fixed SST anomalies are imposed at latitudes of 0°, 20°N, 45°N, 60°N, and 90°N, as labeled.

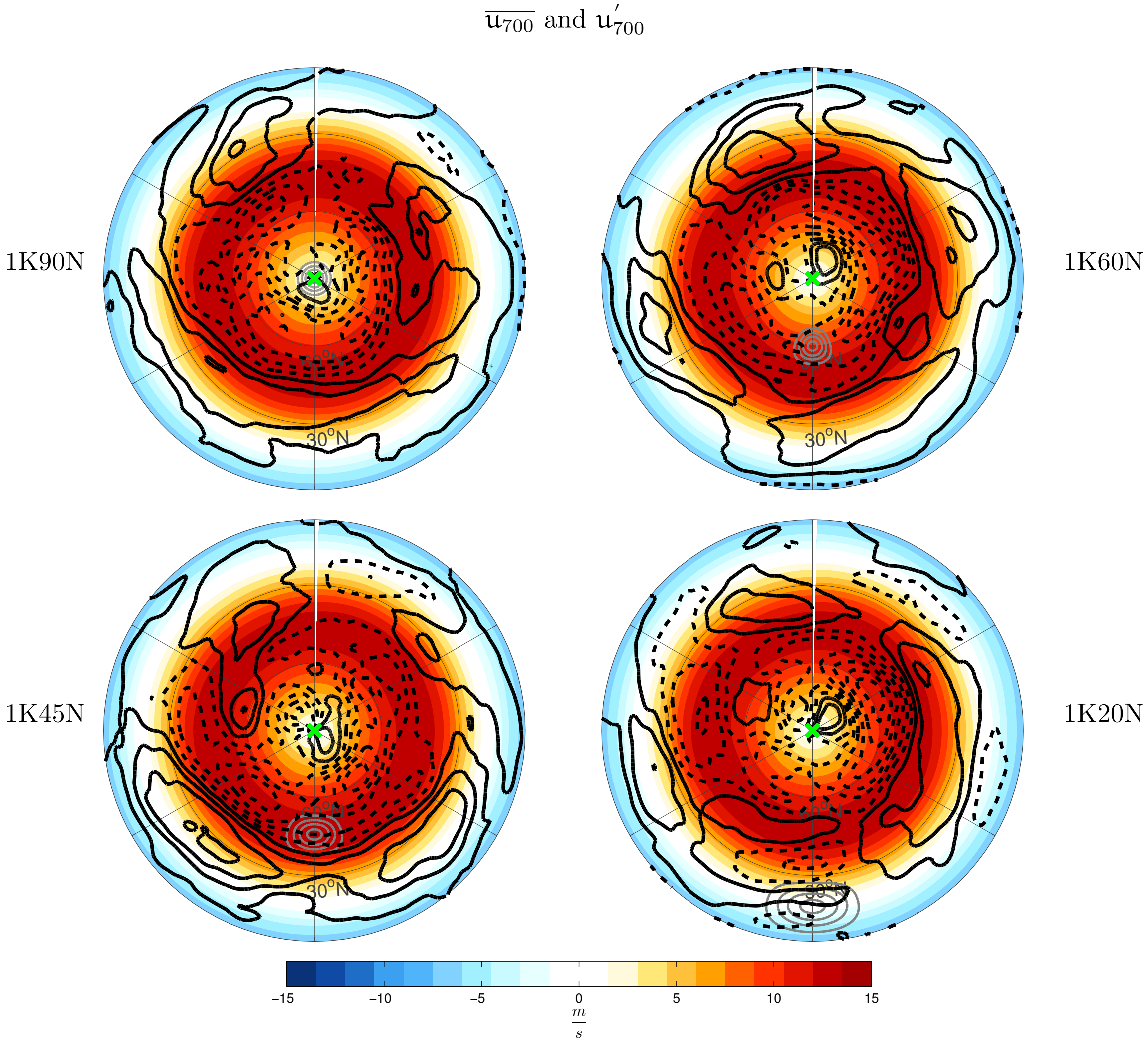

Figure 4.13. Climatological-mean (shading) and steady-state differences (contours) of zonal wind at 700 hPa (u_{700}) for the 1K20N, 1K45N, 1K60N, and 1K90N SST perturbation experiments. Solid (dashed) lines indicate positive (negative) values, and black contours are spaced at 0.2 m/s (-0.3, -0.1, 0.1, 0.3...m/s) for all experiments. The solid gray contours denote the 1K SST anomaly for each experiment. The green X denotes the location of the northern pole on each grid.

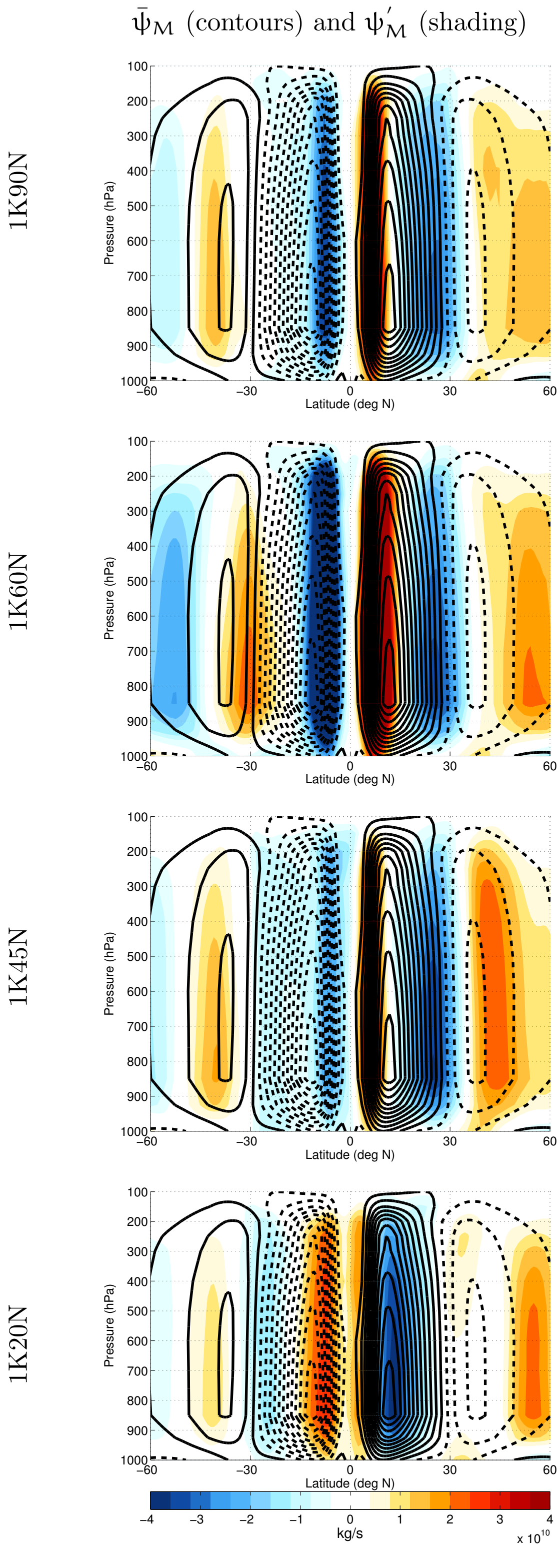

Figure 4.14. Steady-state climatological-mean (contours) and differences (shading) of meridional mass streamfunction for the 1K20N, 1K45N, 1K60N, and 1K90N perturbation experiments. ψ_M contours are spaced at 20×10^{10} kg/s (-30, -10, 10, 30...$\times10^{10}$ kg/s), where solid (dashed) lines indicate positive (negative) values. Note that positive (negative) ψ_M values correspond to clockwise (counterclockwise) motion.

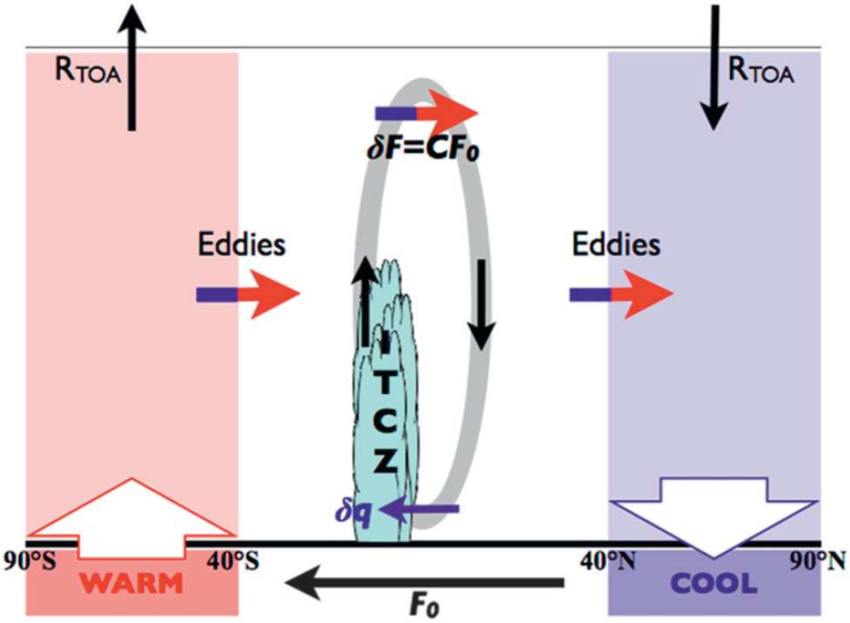

Figure 4.15. From Kang et al. (2009). Schematic of the mechanism that determines the degree of compensation between the resulting response in the atmospheric energy transport and the implied oceanic flux, F_o. The gray oval indicates the anomalous Hadley circulation, of which the direction is denoted with black arrows. The blue (red) part of the arrow, which represents changes in atmospheric energy transports mostly be eddies at the edge of the tropics and by the Hadley circulation within the tropics, indicates cooling (warming). The clockwise anomalous Hadley circulation transports energy northward to cool (warm) the southern (northern) subtropics where it is warmed (cooled) by eddies. Hence, the compensation in the tropics is determined by the response of the total energy fluxes near the edge of the tropics (~$20 - 30°$N or S).

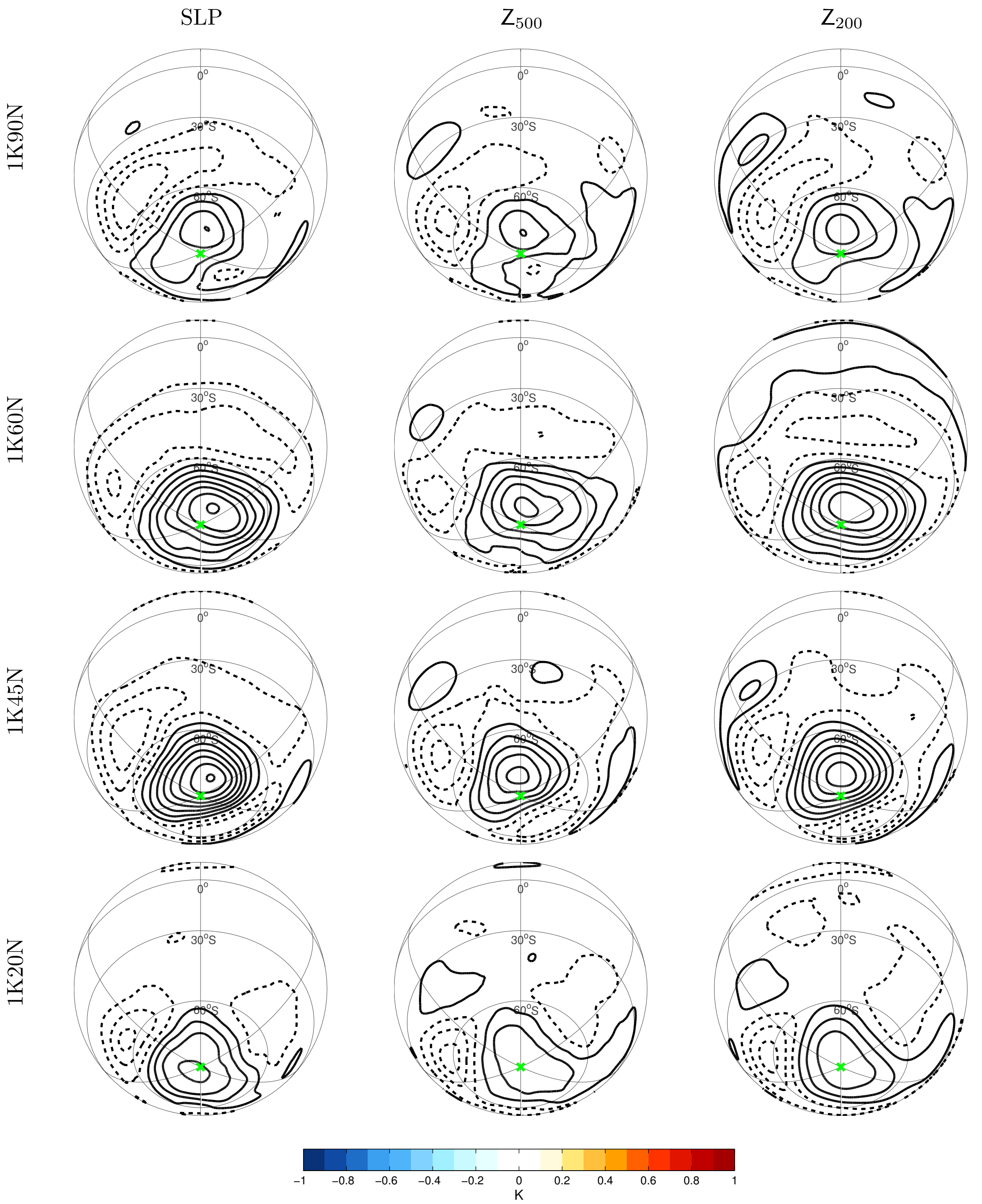

Figure 4.16. Same as in Fig. 4.7, except for steady-state differences in SLP (contours; left column), Z_{500} (contours; middle column), and Z_{200} (contours; right column) over the model's Southern Hemisphere. Solid (dashed) lines indicate positive (negative) values. SLP contours are in 0.5 hPa (-0.75, -0.25, 0.25, 0.75...hPa) intervals for all experiments; Z_{500} and Z_{200} contours are in 3 meter (-4.5, -1.5, 1.5, 4.5...m) and 6 meter (-9, -3, 3, 9...m) intervals, respectively, for all experiments. The green X denotes the location of the southern pole on each grid.

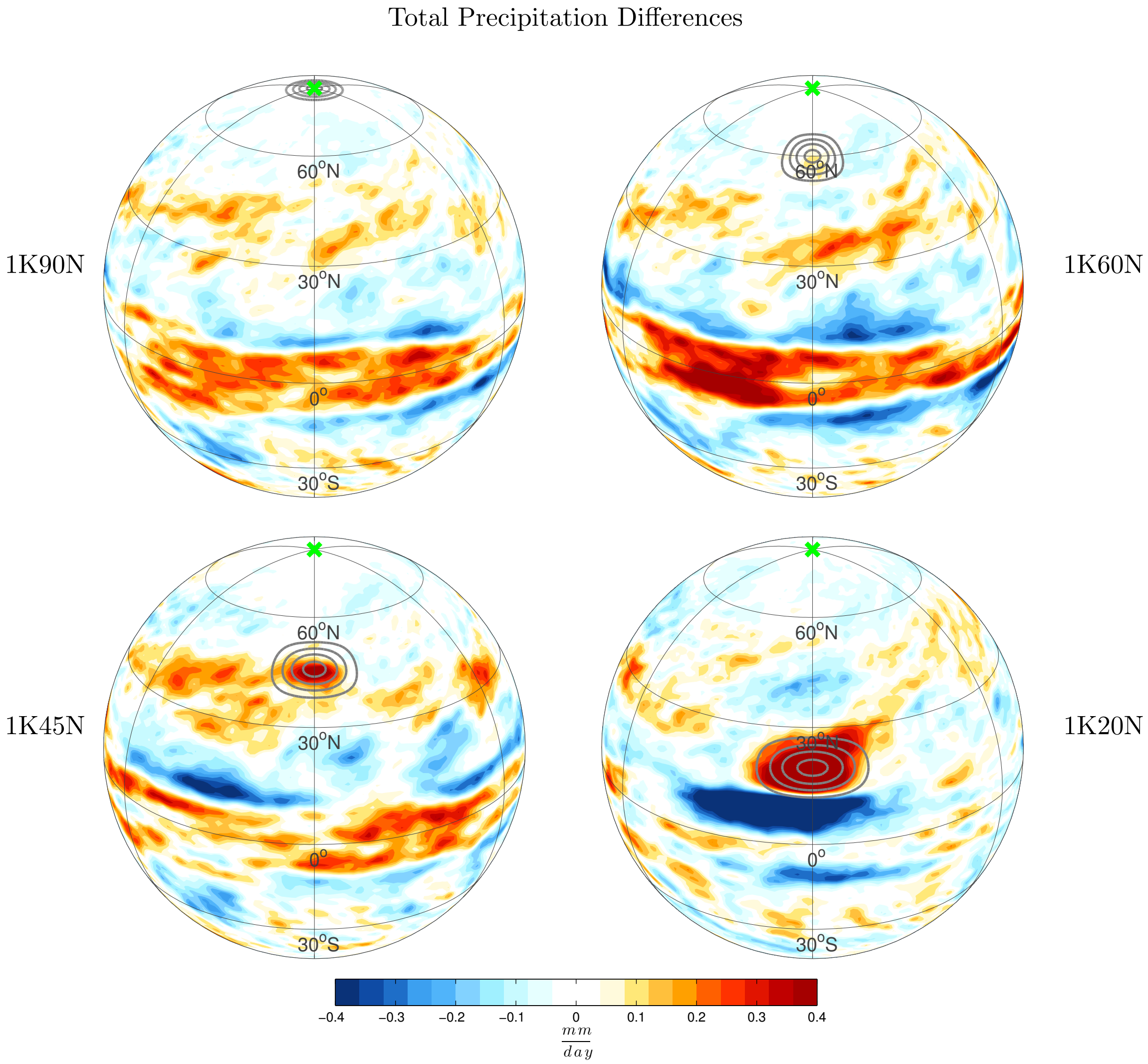

Figure 4.17. Steady-state differences (shading) of total precipitation for the 1K20N, 1K45N, 1K60N, and 1K90N SST perturbation experiments. The solid gray contours denote the 1K SST anomaly for each experiment.

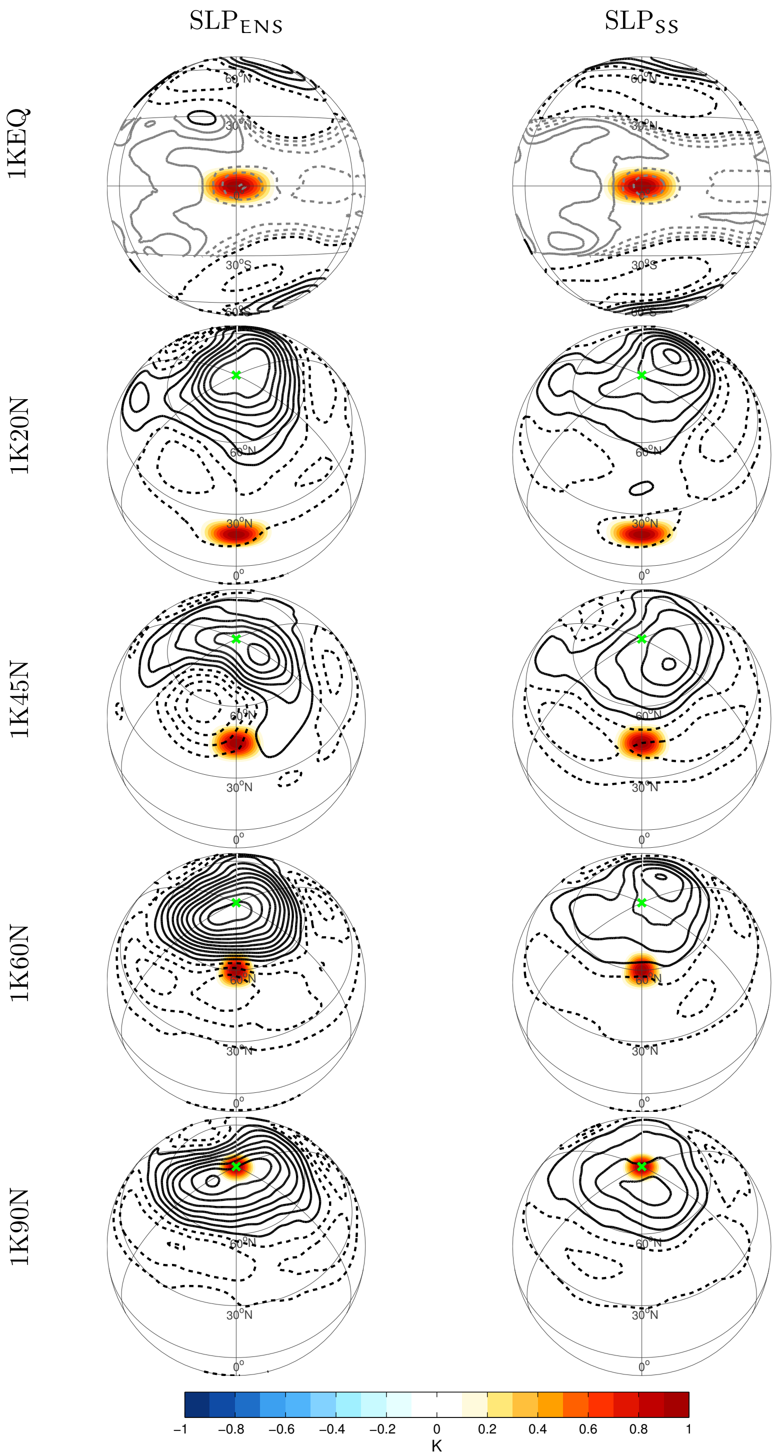

Figure 4.18. Ensemble-mean (left column) and steady-state (right column) differences in SST (shading) and SLP (contours) for the 1KEQ, 1K20N, 1K45N, 1K60N, and 1K90N perturbation experiments. Ensemble-means are averaged for days 61-100 over all 100 ensemble members. Solid (dashed) lines indicate positive (negative) values, and black contours are spaced at 0.5 hPa (-0.75, -0.25, 0.25, 0.75...hPa) intervals for all experiments except 1KEQ, which are spaced at 1 hPa. Additional contours (gray lines) for 1KEQ are inserted between 30°S - 30°N at an interval spacing of 0.1 hPa (-0.15, -0.05, 0.05, 0.15...hPa), and the contour succession is (...|0.15|, |0.25|, |0.35|, |1.35|...hPa), with the first black contour at the separation between gray and black contours corresponding to |0.35| hPa. The green X denotes the location of the pole on each grid.

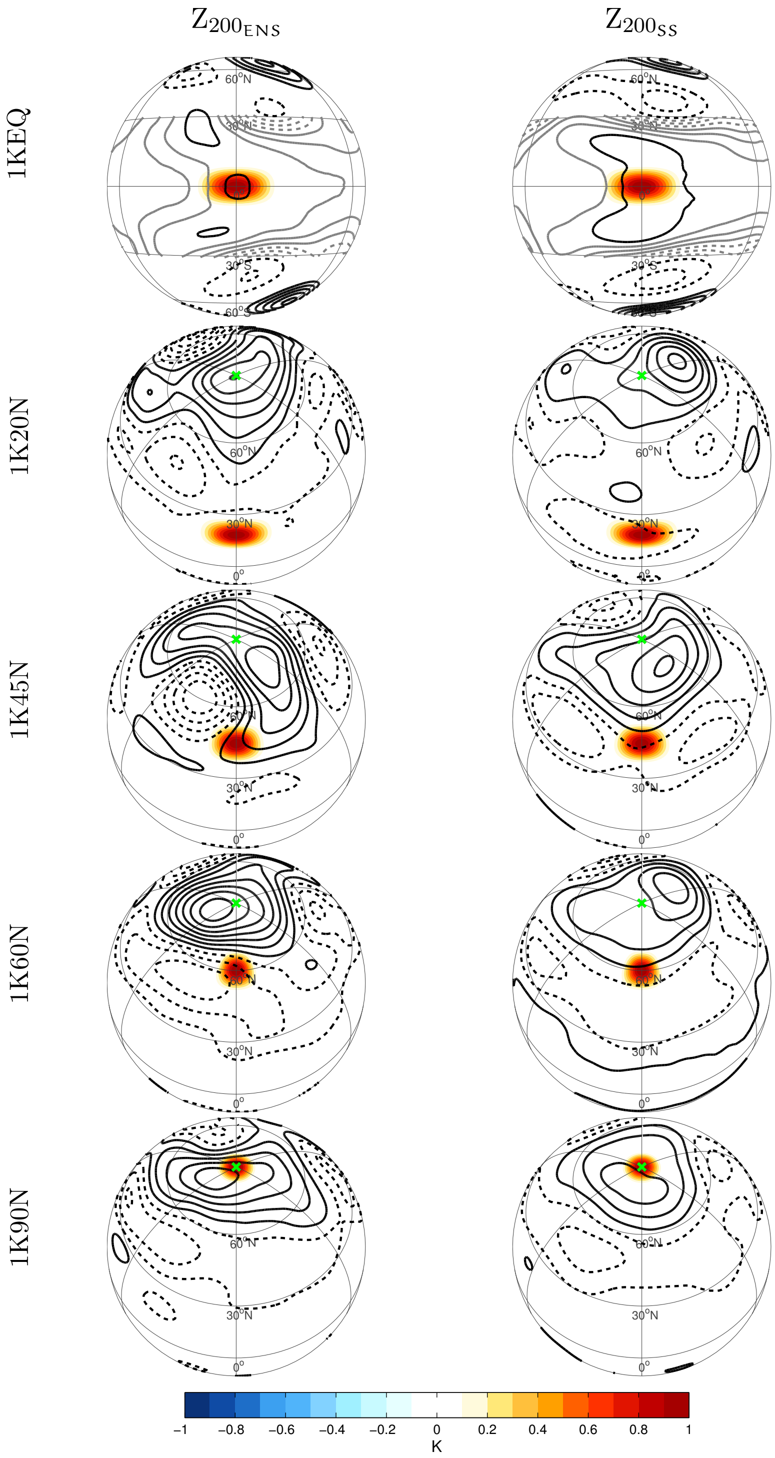

Figure 4.19. Same as in Fig. 4.18, except for ensemble-mean (left column) and steady-state (right column) differences in SST (shading) and Z_{200} (contours). Solid (dashed) lines indicate positive (negative) values, and black contours are spaced at 6 meter (-9, -3, 3, 9...m) intervals for all experiments except 1KEQ, which are spaced at 8 meters. Additional contours (gray lines) for 1KEQ are inserted between 30°S - 30°N at an interval spacing of 4 meter (-6, -2, 2, 6...m), and the contour succession is (...|6|, |10|, |14|, |22|...m), with the first black contour at the separation between gray and black contours corresponding to |14| meters. The green X denotes the location of the pole on each grid.

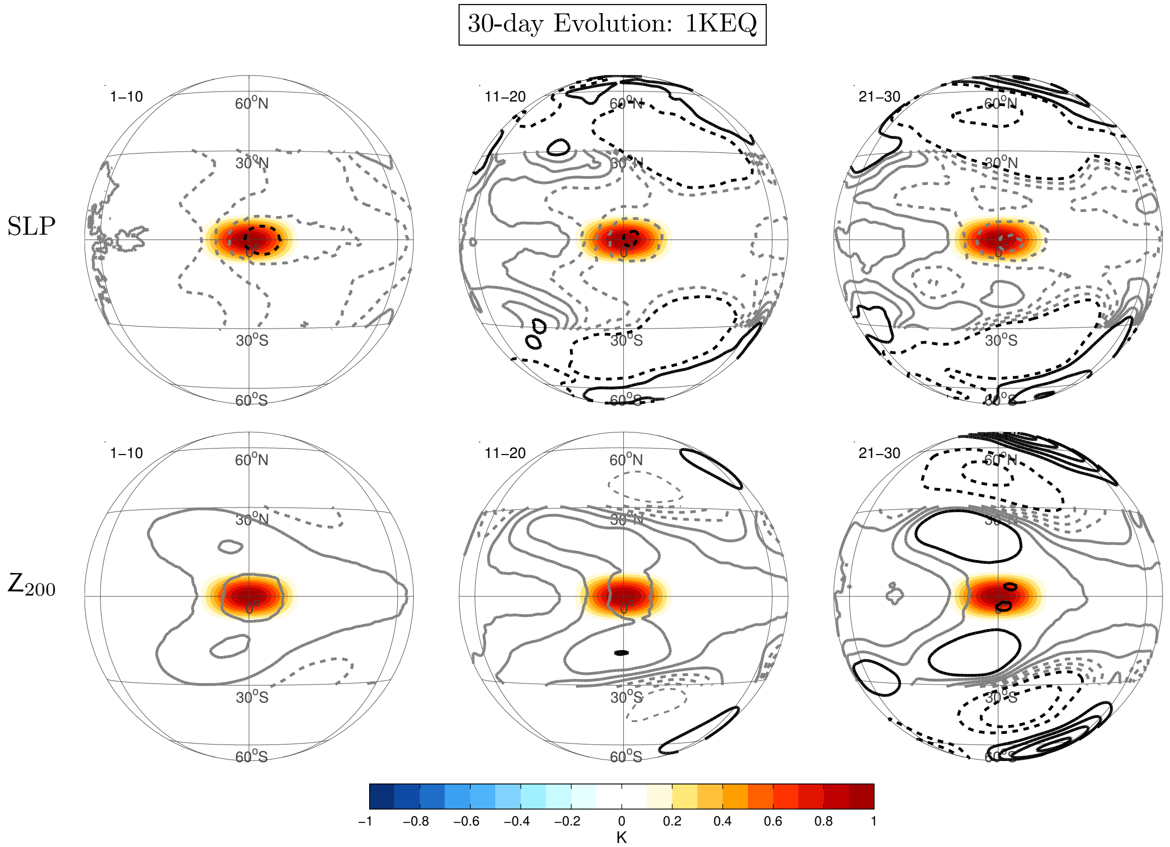

Figure 4.20. Transient ensemble-mean differences in (top row) SLP and (bottom row) Z_{200} for the 1KEQ perturbation experiment. The evolution is shown in consecutive 10-day average increments for the first 30 days. Solid (dashed) lines indicate positive (negative) values, and the black SLP and Z_{200} contours are spaced at 2 hPa and 12 meter intervals, respectively. Additional SLP and Z_{200} contours (gray lines) are inserted between 30°S - 30°N at 0.1 hPa (-0.15, -0.05, 0.05, 0.15...hPa) and 4 meter (-6, -2, 2, 6...m) intervals with contour successions of (...|0.15|, |0.25|, |0.35|, |2.35|...hPa) and (...|6|, |10|, |14|, |26|...m), respectively. The first black SLP (Z_{200}) contour at the separation between gray and black contours corresponds to |0.35| hPa (|14| meters).

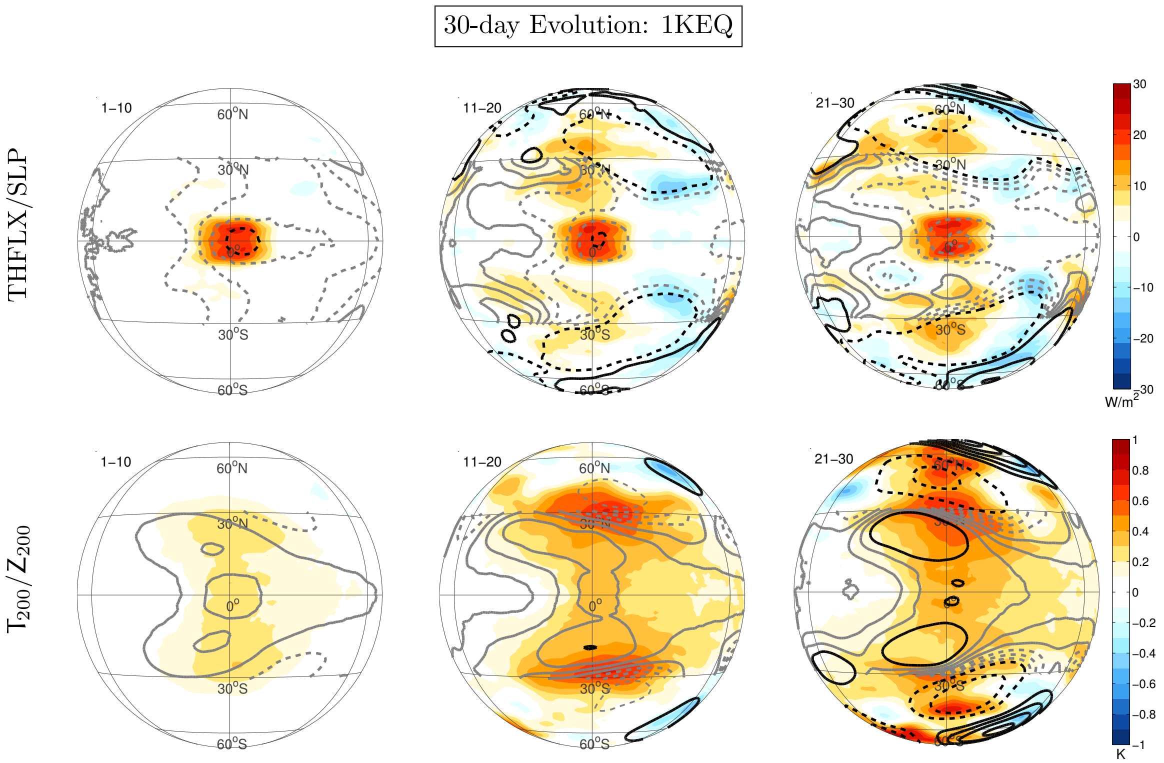

Figure 4.21. Same as in Fig. 4.20, except differences are shown for (top row) SLP and THFLX and (bottom row) Z_{200} and T_{200}.

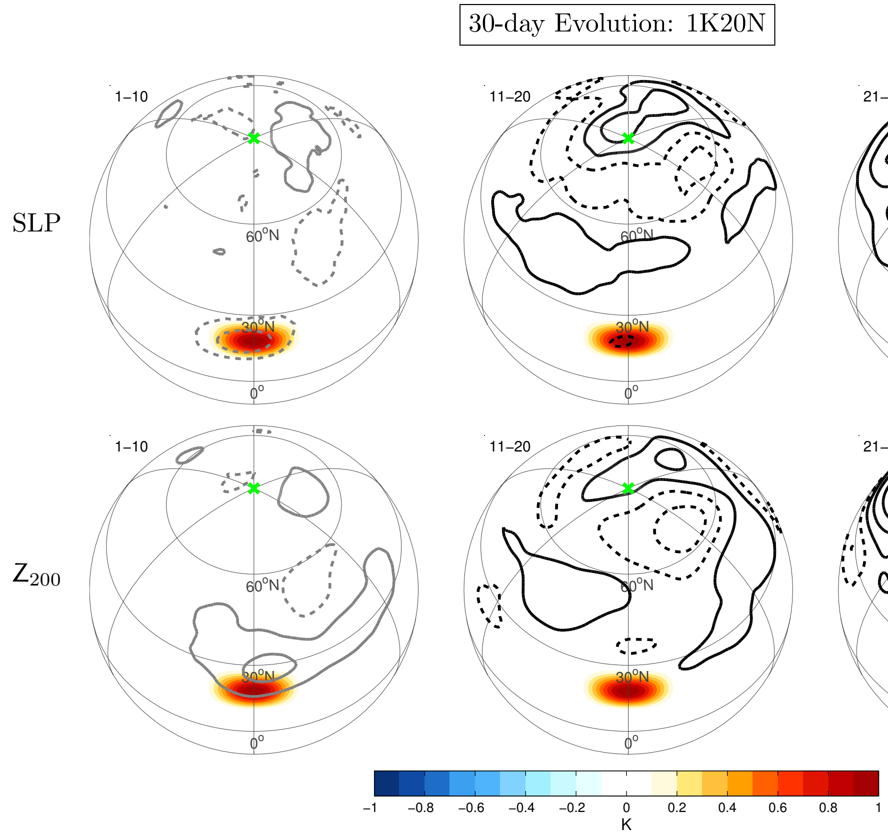

Figure 4.22. Same as in Fig. 4.20, except for the transient ensemble-mean differences for the 1K20N perturbation experiment. Solid (dashed) lines indicate positive (negative) values, and the black SLP and Z_{200} contours are spaced at 1 hPa (-1.5 -0.5, 0.5, 1.5...hPa) and 10 meter (-15, -5, 5, 15...m) intervals, respectively. The gray SLP and Z_{200} contours in the left column (days 1-10) are spaced at 0.2 hPa (-0.3, -0.1, 0.1, 0.3...hPa) and 2 meter (-3, -1, 1, 3...m) intervals, respectively. The green X denotes the location of the pole on each grid.

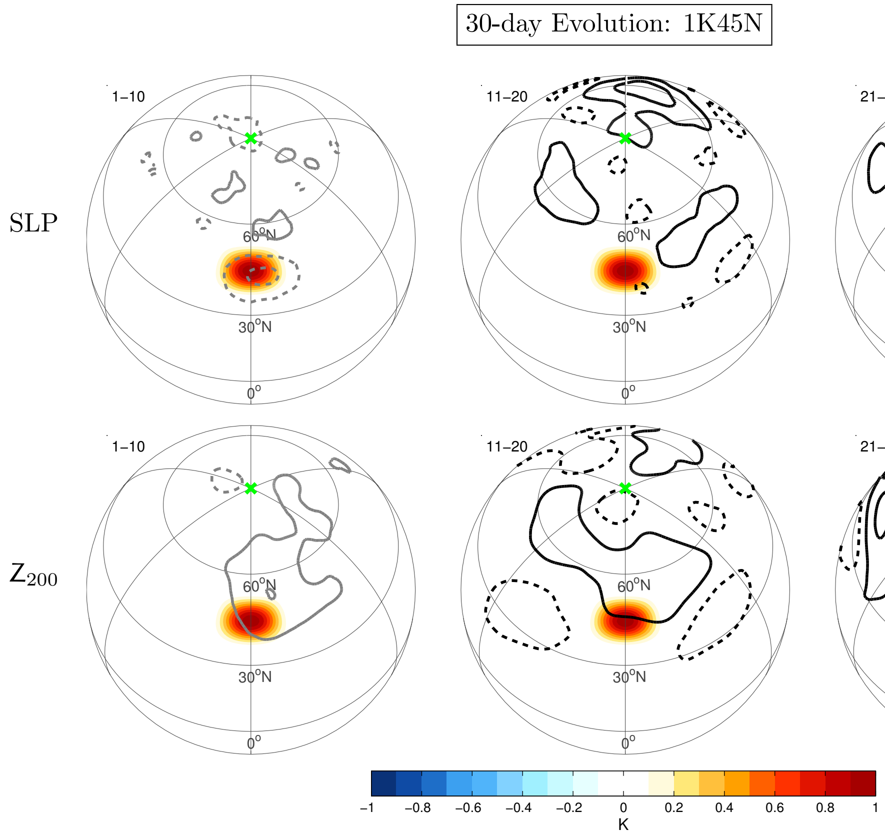

Figure 4.23. Same as in Fig. 4.20, except for the transient ensemble-mean differences for the 1K45N perturbation experiment. Solid (dashed) lines indicate positive (negative) values, and the black SLP and Z_{200} contours are spaced at 1 hPa (-1.5 -0.5, 0.5, 1.5...hPa) and 10 meter (-15, -5, 5, 15...m) intervals, respectively. The gray SLP and Z_{200} contours in the left column (days 1-10) are spaced at 0.2 hPa (-0.3, -0.1, 0.1, 0.3...hPa) and 2 meter (-3, -1, 1, 3...m) intervals, respectively. The green X denotes the location of the pole on each grid.

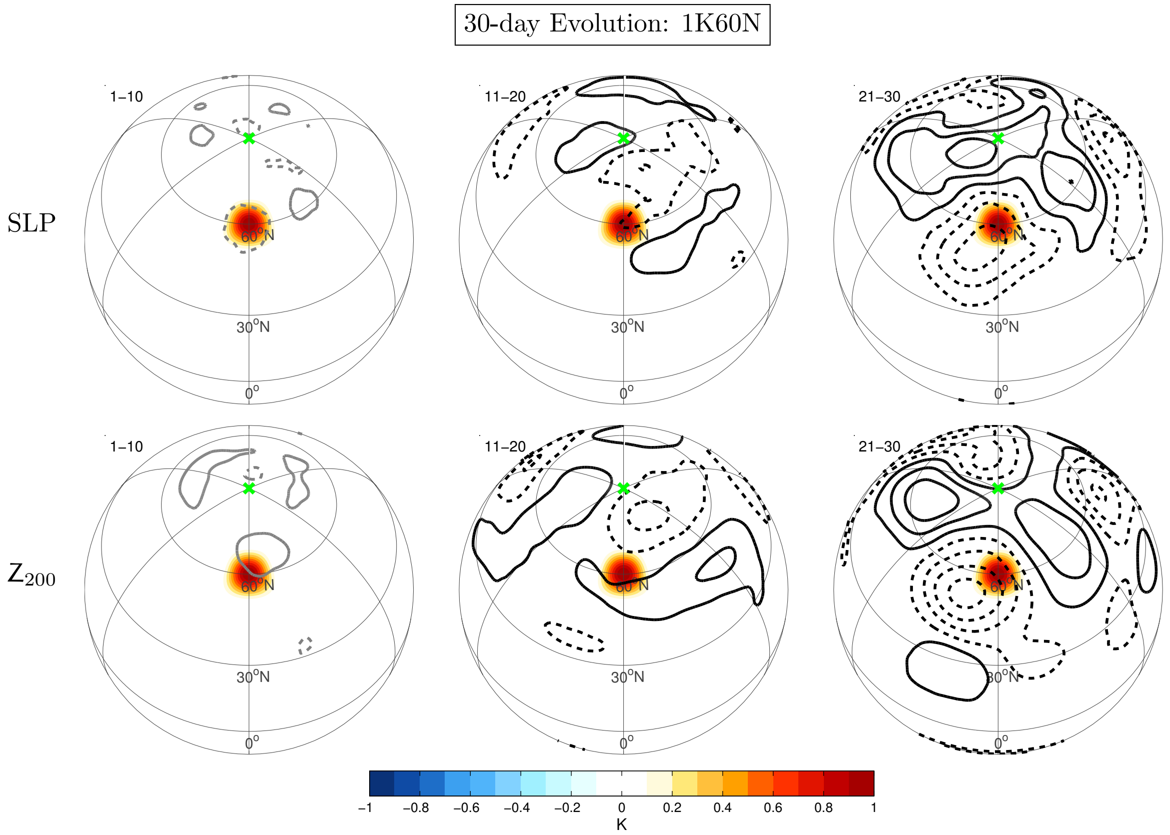

Figure 4.24. Same as in Fig. 4.20, except for the transient ensemble-mean differences for the 1K60N perturbation experiment. Solid (dashed) lines indicate positive (negative) values, and the black SLP and Z_{200} contours are spaced at 1 hPa (-1.5 -0.5, 0.5, 1.5...hPa) and 10 meter (-15, -5, 5, 15...m) intervals, respectively. The gray SLP and Z_{200} contours in the left column (days 1-10) are spaced at 0.2 hPa (-0.3, -0.1, 0.1, 0.3...hPa) and 2 meter (-3, -1, 1, 3...m) intervals, respectively. The green X denotes the location of the pole on each grid.

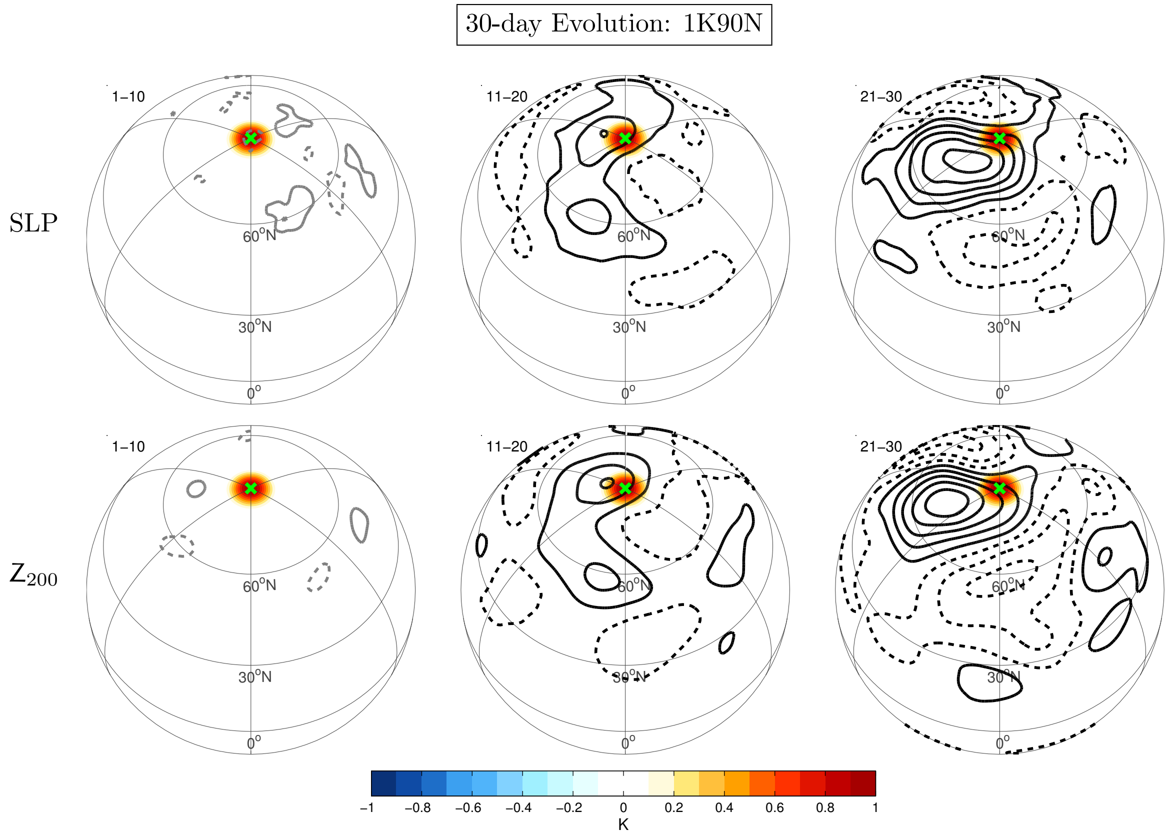

Figure 4.25. Same as in Fig. 4.20, except for the transient ensemble-mean differences for the 1K90N perturbation experiment. Solid (dashed) lines indicate positive (negative) values, and the black SLP and Z_{200} contours are spaced at 1 hPa (-1.5 -0.5, 0.5, 1.5...hPa) and 10 meter (-15, -5, 5, 15...m) intervals, respectively. The gray SLP and Z_{200} contours in the left column (days 1-10) are spaced at 0.2 hPa (-0.3, -0.1, 0.1, 0.3...hPa) and 2 meter (-3, -1, 1, 3...m) intervals, respectively. The green X denotes the location of the pole on each grid.

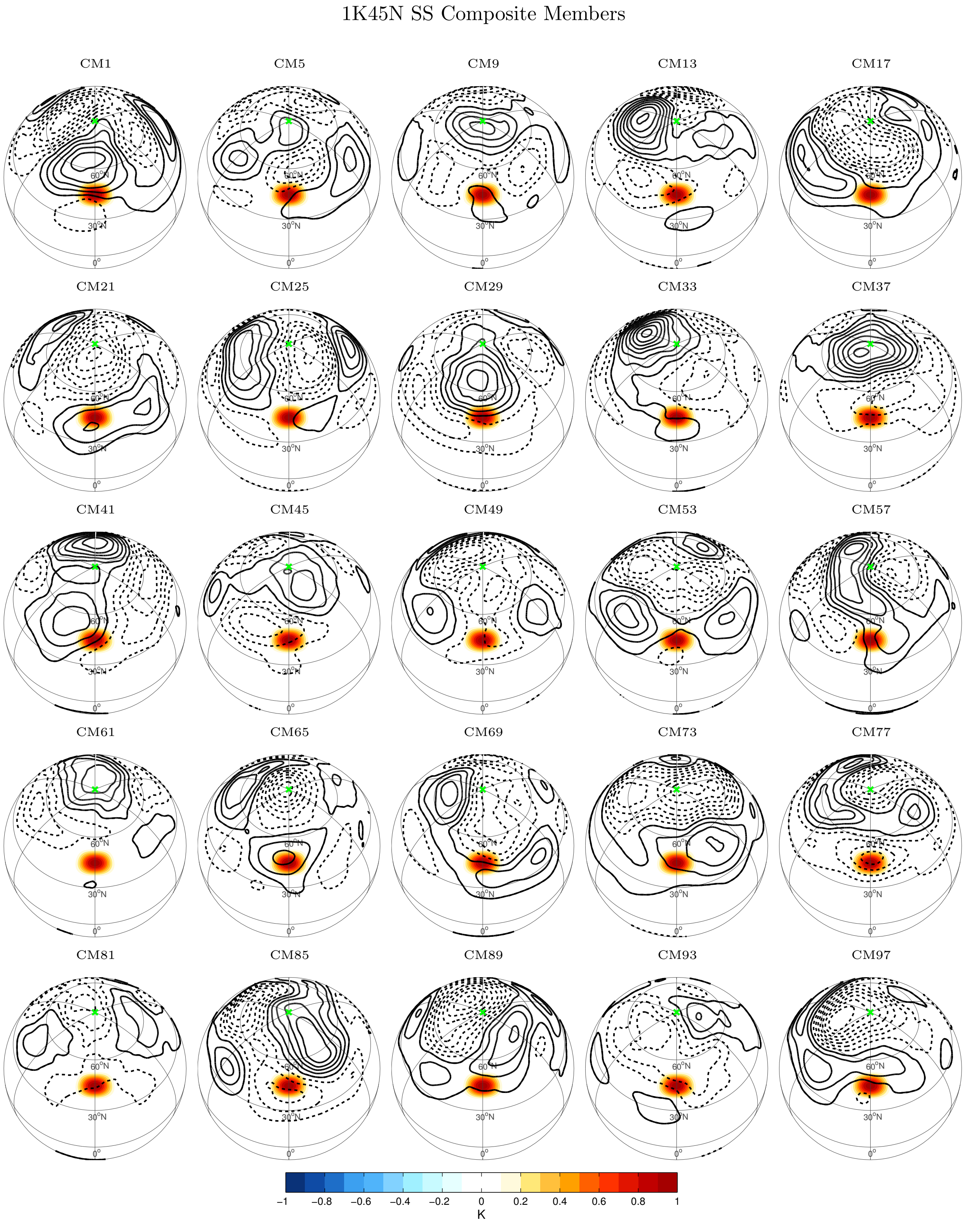

Figure 4.26. Individual composite members (CM) of the steady-state differences in SST (shading) and SLP (contours) for the 1K45N perturbation experiment. Solid (dashed) lines indicate positive (negative) values, and SLP contours are spaced at intervals of 4 hPa (-6, -2, 2, 6...hPa). The green X denotes the location of the pole on each grid.

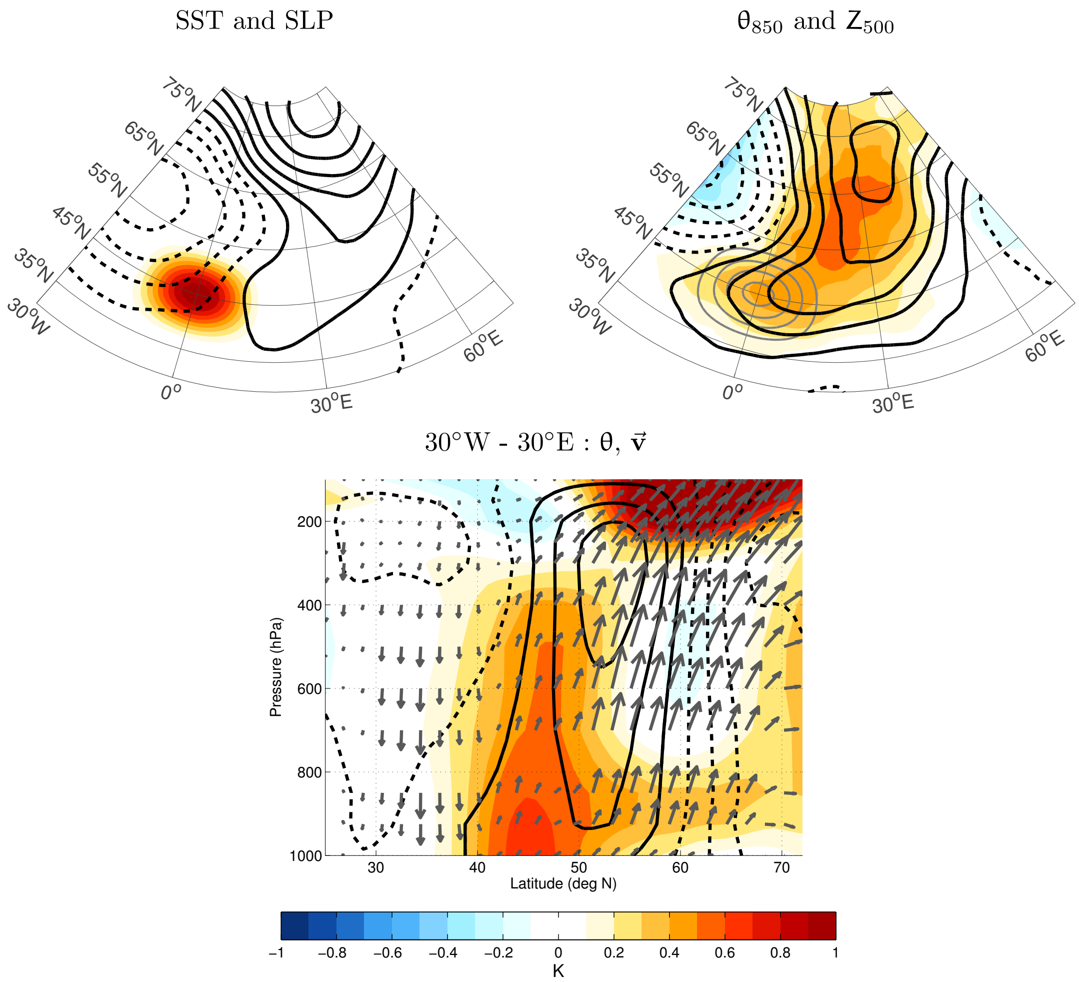

Figure 4.27. (Top row) Ensemble-mean differences of left) SST (shading) and SLP (contours) and right) θ_{850} (shading) and Z_{500} (contours) for the 1K45N experiment. Solid (dashed) lines indicate positive (negative) values, and SLP and Z_{500} contours are spaced at intervals of 0.5 hPa (-0.75, -0.25, 0.25, 0.75...hPa) and 3 meters (-4.5, -1.5, 1.5, 4.5...m), respectively. (Bottom) Vertical cross-section of ensemble-mean zonal-mean differences of θ (shading) and $\vec{v}$ (contours, vectors) averaged over 30°W - 30°E. Zonal wind anomalies are shown in contours at a spacing of 0.3 m/s (-0.45, -0.15, 0.15, 0.45...m/s). Meridional and vertical wind anomalies are shown in vectors in units of m/s, with vertical wind scaled by a factor of 2×10^3 for qualitative comparison.

CHAPTER 5: CONCLUSIONS

5.1 Summary and Discussion

The ocean plays an integral role in the Earth's complex climate system, and its closely coupled relationship with the atmosphere has wide-ranging implications for weather and climate patterns from one region of the globe to another. The atmospheric response to variations in tropical sea surface temperatures (SST) is robust in both models and observations, and the influence of the tropical ocean on the large-scale atmospheric circulation is generally well-understood. Improvements in the resolution of satellite observations and numerical models over the past decade have also led to a series of advances in understanding the role of the ocean in extratropical air-sea interaction and climate variability. While the influence of the midlatitude ocean can be relatively subtle and difficult to detect, recent observational and numerical studies have provided a growing body of evidence suggesting that the midlatitude ocean has a potentially more important influence on the atmospheric circulation on a range of different time scales than previously thought.

5.1.1 Observed Air-Sea Interaction on Subseasonal Timescales

In the first theme of this dissertation, observational analyses exploit daily-mean output from the ERA-Interim Reanalyses dataset to re-examine the evidence for midlatitude air-sea interaction over the Kuroshio-Oyashio Extension (KOE) region on subseasonal timescales, while also drawing important comparisons to a previous companion study over the Gulf Stream Extension region (e.g., Wills et al. 2016). Results indicate that during the cold season, SST anomalies in both the Gulf Stream and Kuroshio-Oyashio Extension regions are associated with distinct patterns of atmospheric variability that precede and follow peak amplitude in the SST field (Fig. 3.8). Prior to the onset of the largest SST anomalies, both basins exhibit similar "atmospheric forcing" patterns resulting from temperature advection due to the anomalous flow acting on the climatological-mean SST gradient (Fig. 3.8, upper panels). After the onset of peak SST anomalies, both basins exhibit a distinct "atmospheric response" pattern of low pressure anomalies that do not notably amplify with height and are centered over and to the east of anomalously warm SSTs in the western boundary currents (Fig. 3.8, lower panels).

The "atmospheric forcing" pattern is consistent with the primary direction of atmosphere-to-ocean forcing in the midlatitudes (e.g., Davis 1976, 1978; Deser and Timlin 1997; Kushnir et al. 2002), and the broad characteristics of the "atmospheric response" pattern are consistent with the theoretical linear response to midlatitude SST anomalies (e.g., Hoskins and Karoly 1981). However, it is interesting that there are very similar spatial and temporal relationships between atmospheric forcing and wintertime SST variability in both the Kuroshio-Oyashio and Gulf Stream Extensions on daily-mean time scales, considering that the North Atlantic and North Pacific sectors are subject to different patterns of climate variability, proximity to land barriers, and internal ocean processes. Given that wintertime variations in SSTs in the Kuroshio-Oyashio Extension region can also be forced by variations in subtropical mode water volume, changes in the path and transport of the western boundary current, anomalous oceanic temperature advection, remote teleconnections, and other factors (e.g., Kelly et al. 2010; Kwon et al. 2010; Frankignoul et al. 2011; Kwon and Joyce 2013; Smirnov et al. 2015), the North Pacific results have potentially important implications for understanding the atmospheric response to internal ocean dynamics in the Kuroshio-Oyashio Extension region.

The one notable difference in the lagged patterns of pressure anomalies between the two ocean basins seen in the bottom panels of Fig. 3.8 is the inconsistent position of surface high pressure anomalies relative to the location of warm SST anomalies. While this feature is not statistically significant and confined to the surface in the North Pacific, it is actually a very robust feature in the North Atlantic and appears to have a unique relationship to SST variations in the Gulf Stream Extension. For example, the pattern is statistically significant (not shown), amplifies with height (Fig. 3.9, bottom), and appears dependent on the downstream advection of positive lower-tropospheric temperature anomalies over the Gulf Stream by the climatological-mean flow (Fig. 3.10, middle). Importantly, the anomalous warming to the northeast of the Gulf Stream Extension coincides with anomalous upward motion (Fig. 3.11), suggesting that heating associated with the extratropical SST anomalies can be viewed as forcing changes in vertical motion and thus communicating with the upper-tropospheric circulation.

5.1.2 Re-evaluating the Role of the Ocean in an Idealized Framework

The second theme of this dissertation is partially motivated by the results from the observational analyses, which suggest that extratropical SST anomalies on subseasonal timescales are capable of forcing significant changes in the large-scale atmospheric circulation through the transfer of heat from the ocean to the atmosphere. To explore the observed behavior of atmospheric forcing due to extratropical ocean heating, idealized numerical experiments were designed to analyze the atmospheric response to a one-way (ocean-to-atmosphere) forcing where anomalous surface heating is placed at different latitudes on the globe. An aquaplanet configuration is used to provide a simplified model framework to critically assess the influence of the ocean on the atmosphere. Simulations were performed on a relatively new aquaplanet configuration of the NCAR Community Atmosphere Model, Version 5.3 (CAM5.3), in which the atmosphere-only model simulates an idealized climate above a completely water-covered planet with otherwise Earth-like characteristics (e.g., Neale and Hoskins 2000a,b; Medeiros et al. 2016), under perpetual equinox conditions. Two sets of fixed SST experiments were performed to analyze the steady-state and transient atmospheric responses to imposed SST anomalies placed at 0°, 20°N, 45°N, 60°N, and 90°N.

The aquaplanet model generated a robust tropical atmospheric circulation and remote teleconnections in response to an equatorial heat source in both the steady-state (Figs. 4.3

- 4.5) and transient (Figs. 4.20 - 4.21) experiments, and the results are consistent with the theoretical linear response to a tropical SST anomaly (e.g., Gill 1980; Hoskins and Karoly 1981; Horel and Wallace 1981; Heckley and Gill 1984; Lindzen and Nigam 1987). The results also show a rapid communication of surface warming to the upper tropical troposphere that spreads uniformly throughout the remote tropics, as found in previous studies (e.g., Bantzer and Wallace 1996; Lintner and Chiang 2006; Maloney and Sobel 2007). While the results of the transient experiments for the extratropical SST perturbations were less insightful (except for the 1K45N experiment), the steady-state experiments revealed an interesting and unexpected result, as discussed below.

Results for the steady-state 1K20N, 1K45N, 1K60N, and 1K90N perturbation experiments indicated a similar, robust atmospheric circulation response to an imposed heating at each of the latitudes (Figs. 4.7 - 4.8). The response pattern resembles the leading mode of model internal variability (Fig. 4.9), characterized by a zonally-symmetric dipole structure with strongly positive SLP and geopotential height anomalies over the polar latitudes (poleward of 60°N) and weaker negative SLP and geopotential height anomalies over the midlatitudes (30°N - 60°N). There are interesting similarities in the characteristics of the leading mode structure in the aquaplanet model and the observed leading modes of extratropical variability in the Northern and Southern Hemispheres, or the Northern and Southern Annular Modes, respectively (e.g., Kidson 1988; Thompson and Wallace 2000; Lorenz and Hartmann 2001). Previous studies have indicated that variations in midlatitude SST fronts in both hemispheres can indirectly impact the leading modes of atmospheric variability (such as the annular modes) through their influence on the strength and position of the atmospheric storm tracks and eddy-driven jets (e.g, Nakamura et al. 2008; Frankignoul et al. 2011; Taguchi et al. 2012; Ogawa et al. 2016; O'Reilly et al. 2017; Seo et al. 2017).

While it is not entirely unexpected that the atmospheric response to anomalous ocean forcing projects onto the leading internal modes of variability, *it is unexpected* that the atmospheric circulation response is seemingly independent of the latitudinal placement of the SST anomaly. Unlike the 1K45N, 1K60N, and 1K90N experiments, the 1K20N SST perturbation would strengthen the midlatitude surface temperature gradient (and hence the low-level baroclinicity), resulting in a poleward shift of both the storm track and eddy-driven jet (e.g., Brayshaw et al. 2008; Michel and Riviére 2014; Baker et al. 2017). However, there appears to be an equatorward shift of the eddy-driven jet in response to extratropical thermal forcing in all experiments (e.g., Fig. 4.13). One possible explanation can be inferred from the preferential and infinite heating of the model's northern hemisphere, which would lead to an energy imbalance on longer time scales. Studies suggest that such an energy imbalance leads to anomalous meridional eddy energy fluxes that force changes in the Hadley and Ferrel circulations (e.g., Kang et al. 2008, 2009; White et al. 2018), thus shifting the location of the midlatitude storm track and eddy-driven jet. These results are worth exploring in future analyses.

The transient experiments also yielded a low polarity annular mode response to surface thermal forcing for all extratropical latitudes except 45°N, which indicated a more Rossby wave-like response compared to the "zonally-symmetric" steady-state response. Composite analysis of the 10,000-day 1K45N simulation indicated that there is large variability in the atmospheric response, likely due to the location of the anomalous heating relative to the core of the eddy-driven jet (e.g., Fig. 4.12). While the steady-state 1K45N results may reflect an average of individual Rossby wave responses to the anomalous heat source, it is possible that different physical mechanisms are responsible for the contrasting atmospheric responses on shorter versus longer timescales. Interestingly, the ensemble-mean 1K45N results bear a resemblance to the observed atmospheric "response" pattern that lags anomalously warm SSTs over the Gulf Stream Extension region by a few weeks (e.g., Figs. 3.8 - 3.9, 4.27). Specifically, the ensemble-mean results reproduced the robust, downstream high pressure feature associated with anomalous upward and poleward motion over the North Atlantic (e.g., Fig. 3.11). Additional analyses on the 1K45N SST perturbation experiments may provide clearer insights for interpreting the atmospheric "response" to midlatitude SST anomalies in the real climate system.

5.2 Future Work

The analyses presented in this dissertation provide new insights into the role of the ocean in extratropical air-sea interaction and climate variability on intraseasonal and climatological-mean time scales. The following avenues of future research outline additional experiments that would expand on the results from the idealized model framework.

5.2.1 Transient Atmospheric Response to Extratropical Heating: Part II

As noted at the end of Ch. 4, the idealized transient numerical experiments yielded inconclusive results based on the 100-member ensemble used in the analyses. However, the numerical results from the 1K45N SST perturbation experiments yielded interesting insight into the transient versus steady-state atmospheric response to thermal forcing, with potentially important implications for interpreting the observed atmospheric "response" pattern presented in Ch. 3. Given large variability in the eddy-driven jet response to anomalous heating near the jet core, it is possible that a larger sample of ensemble members would provide a better evaluation of the short-term atmospheric response to a midlatitude SST anomaly located at 45°N. For example, transient experiments by Deser et al. (2007) and Ferreira and Frankignoul (2005), who explored the transient atmospheric response to SST anomalies associated with the North Atlantic SST tripole, were performed with 240-member and 400-member ensembles, respectively. While their experiments were performed on slightly to moderately more complex global climate models compared to CAM5.3, the studies also employed SST anomalies that were 3x - 5x larger in amplitude than the observed anomalies in order to obtain robust statistics. It would seem that despite the simplicity of the aquaplanet model, a larger sample of ensemble members would be necessary to explore the atmospheric response to a smaller and more realistic SST anomaly. To do this, additional ensemble members can be generated from the same 10,000-day control run to supplement the existing sample of ensemble simulations, and the same analyses can be repeated using the full output to calculate the updated 1K45N ensemble-mean results.

5.2.2 Sensitivity Studies

Sensitivity studies are an important component of the modelling hierarchy, in which models of increasing complexity and experimental design provide a framework for systematically evaluating the link between theory, observations, and models (e.g., Neale and Hoskins 2000a,b; Blackburn and Hoskins 2013; Williamson et al. 2013). The numerical analyses presented in the dissertation can be expanded by performing simple sensitivity studies to critically assess the processes responsible for the key features of the steady-state atmospheric circulation response. Using the aquaplanet configuration of CAM5.3, it would be computationally inexpensive to perform a variety of different sensitivity experiments to contribute to the idealized framework and gain a better understanding on the relative role of the midlatitude ocean and its influence on the large-scale atmospheric circulation.

Given the "base" set of results from the experiments in the dissertation, the first step of the sensitivity study is already complete, where the "base" results can now serve as the baseline of comparison to test different objectives. Furthermore, the model set-up is also complete, so this avenue of future research will be easy to begin. Future sensitivity studies could explore changes in the characteristics of the SST anomaly itself, such as different forcing amplitudes or variations in the strength of the SST gradients on the edges of the SST anomaly. Additionally, future SST anomaly experiments would benefit from exploring the linearity of the atmospheric response to negative thermal forcing at different latitudes. It would also be interesting to repeat the "base" set of experiments with a different background surface temperature profile to explore sensitivities in the atmospheric response to the same SST anomalies in the context of a different background state. By incorporating different background states, the idealized model framework could be used to compare the atmospheric response to extratropical SST anomalies for other seasons, asymmetric SST distributions, and varying locations of the midlatitude storm track and eddy-driven jet.

REFERENCES

Alexander, M.A., 1992: Midlatitude Atmosphere-Ocean Interaction during El Niño. Part I: The North Pacific Ocean. *J. Climate*, **5**, 944 - 958.

Alexander, M.A., I. Bladé, M. Newman, J.R. Lanzante, N.-C. Lau, J.D. Scott, 2002: The Atmospheric Bridge: The Influence of ENSO Teleconnections on Air-Sea Interaction over the Global Oceans. *J. Climate*, **15**, 2205 - 2231.

Back, L.E., and C.S. Bretherton, 2009: On the Relationships between SST Gradients, Boundary Layer Winds, and Covergence over the Tropical Oceans. *J. Climate*, **22**, 4182 - 4196.

Baker, H.S., T. Woolings, and C. Mbengue, 2017: Eddy-Driven Jet Sensitivity to Diabatic Heating in an Idealized GCM. *J. Climate*, **30**, 6413 - 6431.

Bantzer, C.H., and J.M. Wallace, 1996: Intraseasonal Variability in Tropical Mean Temperature and Precipitation and Their Relation to the Tropical 40 - 50 Day Oscillation. *J. Atmos. Sci*, **53**, 3032 - 3045.

Barsugli, J.J., and D.S. Battisti, 1998: The Basic Effects of Atmosphere-Ocean Thermal Coupling on Midlatitude Variability. *J. Atmos. Sci.*, **55**, 477 - 493.

Blackburn, M., and B.J. Hoskins, 2013: Context and Aims of the Aqua-Planet Experiment. *J. Met. Soc. Jap.*, **91A**, 1 - 15.

Brayshaw, D.J., B. Hoskins, and M. Blackburn, 2008: The Storm-Track Response to Idealized SST Perturbations in an Aquaplanet GCM. *J. Atmos. Sci.*, **65**, 2842 - 2860.

Bretherton, C.S., M. Widmann, V.P. Dymnikov, J.M. Wallace, and I. Bladé, 1999: The Effective Number of Spatial Degrees of Freedom of a Time-Varying Field. *J. Climate*, **12**, 1990 - 2009.

Cayan, D.R., 1992: Latent and Sensible Heat Flux Anomalies over the Northern Oceans: Driving the Sea Surface Temperature. *J. Phys. Oceanogr.*, **22**, 859 - 881.

Chelton, D.B., S.K. Esbensen, M.G. Schlax, N. Thum, M.H. Freilich, F.J. Wentz, C.L. Gentemann, M.J. McPhaden, and P.S. Schopf, 2001: Observations of Coupling between Surface Wind Stress and Sea Surface Temperature in the Eastern Tropical Pacific. *J. Climate*, **14**, 1479 - 1498.

Chelton, D.B., M.G. Schlax, M.H. Freilich, and R.F. Milliff, 2004: Satellite Measurements Reveal Persistent Small-Scale Features in Ocean Winds. *Science*, **303**, 978 - 983.

Chelton, D.B., and S.-P. Xie, 2010: Coupled ocean-atmosphere interaction at oceanic mesoscales. *Oceanography*, **23**, 52 - 69.

Chiang, J.C.H., S.E. Zebiak, M.A. Cane, 2001: Relative Roles of Elevated Heating and Surface Temperature Gradients in Anomalous Surface Winds over Tropical Oceans. *J. Atmos. Sci.*, **58**, 1371 - 1394.

Chiang, J.C.H, and A.H. Sobel, 2002: Tropical Tropospheric Temperature Variations Caused by ENSO and Their Influence on the Remote Tropical Climate. *J. Climate*, **15**, 2616 - 2631.

Ciasto, L.M., and D.W.J. Thompson, 2004: North Atlantic Atmosphere-Ocean Interaction on Intraseasonal Time Scales. *J. Climate*, **17**, 1617 - 1621.

Czaja, A., and N. Blunt, 2011: A new mechanism for ocean-atmosphere coupling in midlatitudes. *Q. J. R. Meteorol. Soc.*, **137**, 1095 - 1101.

Davis, R.E., 1976: Predictability of Sea Surface Temperature and Sea Level Pressure Anomalies over the North Pacific Ocean. *J. Phys. Oceanogr.*, **6**, 249 - 266.

Davis, R.E., 1978: Predictability of Sea Level Pressure Anomalies Over the North Pacific Ocean. *J. Phys. Oceanogr.*, **8**, 233 - 246.

Dee, D.P., S.M. Uppala, A.J. Simmons, P. Berrisford, P. Poli, S. Kobayashi, U. Andrae, M.A. Balmaseda, G. Balsamo, P. Bauer, P. Bechtold, A.C.M. Beljaars, L. van de Berg, J. Bidlot, N. Bormann, C. Delsol, R. Dragani, M. Fuentes, A.J. Geer, L. Haimberger, S.B. Healy, H. Hersbach, E.V. Holm, L. Isaksen, P. Kallberg, M. Kohler, M. Matricardi, A.P. McNally, B.M. Monge-Sanz, J.-J. Morcrette, B.-K. Park, C. Peubey, P. de Rosnay, C. Tavolato, J.-N. Thepaut, and F. Vitart, 2011: The ERA-Interim reanalysis: configuration and performance of the data assimilation system. *Q. J. R. Meteorol. Soc.*, **137**, 553 - 597.

Deremble, B., G. Lapeyre, and M. Ghil, 2012: Atmospheric Dynamics Triggered by an Oceanic SST Front in a Moist Quasigeostrophic Model. *J. Atmos. Sci.*, **69**, 1617 - 1632.

Deser, C., and M.S. Timlin, 1997: Atmosphere-Ocean Interaction on Weekly Timescales in the North Atlantic and Pacific. *J. Climate*, **10**, 393 - 408.

Deser, C., G. Magnusdottir, R. Saravanan, and A. Phillips, 2004: The Effects of North Atlantic SST and Sea Ice Anomalies on the Winter Circulation in CCM3. Part II: Direct and Indirect Components of the Response. *J. Climate*, **17**, 877 - 889.

Deser, C., R.A. Tomas, and S. Peng, 2007: The Transient Atmospheric Circulation Response to North Atlantic SST and Sea Ice Anomalies. *J. Climate*, **20**, 4751 - 4767.

Deser, C., M.A. Alexander, S.-P. Xie, and A.S. Phillips, 2010: Sea Surface Temperature Variability: Patterns and Mechanisms. *Annu. Rev. Mar. Sci.*, **2**, 115 - 143.

Diaz, H.F., M.P. Hoerling, and J.K. Eischeid, 2001: ENSO Variability, Teleconnections and Climate Change. *Int. J. Climatol.*, **21**, 1845 - 1862.

Ferreira, D., and C. Frankignoul, 2005: The Transient Atmospheric Response to Midlatitude SST Anomalies. *J. Climate*, **18**, 1049 - 1067.

Frankignoul, C., and R.W. Reynolds, 1983: Testing a Dynamical Model for Mid-Latitude Sea Surface Temperature Anomalies. *J. Phys. Oceanogr.*, **13**, 1131 - 1145.

Frankignoul, C., N. Sennechael, Y-O. Kwon, and M.A. Alexander, 2011: Influence of the Meridional Shifts of the Kuroshio and the Oyashio Extensions on the Atmospheric Circulation. *J. Climate*, **24**, 762 - 777.

Gill, A.E., 1980: Some simple solutions for heat-induced tropical circulation. *Quart. J. R. Met. Soc.*, **106**, 447 - 462.

Heckley, W.A., and A.E. Gill, 1984: Some simple analytical solutions to the problem of forced equatorial long waves. *Quart. J. R. Met. Soc.*, **110**, 203 - 217.

Hoerling, M.P., J.W. Hurrel, T. Xu, G.T. Bates, and A.S. Phillips, 2004: Twentieth century North Atlantic climate change. Part II: Understanding the effect of Indian Ocean warming. *Clim. Dyn.*, **23**, 391 - 405.

Horel, J.D., and J.M. Wallace, 1981: Planetary-Scale Atmospheric Phenomena Associated with the Southern Oscillation. *Mon. Wea. Rev.*, **109**, 813 - 829.

Hoskins, B.J., and D.J. Karoly, 1981: The Steady Linear Response of a Spherical Atmosphere to Thermal and Orographic Forcing. *J. Atmos. Sci.*, **38**, 1179 - 1196.

Hoskins, B.J, and P.J. Valdes, 1990: On the Existence of Storm-Tracks. *J. Atmos. Sci*, **47**, 1854 - 1864.

Hurrel, J.W., 1995: Decadal Trends in the North Atlantic Oscillation: Regional Temperatures and Precipitation. *Science, New Ser.*, **269**, 676 - 679.

Inatsu, M., H. Mukougawa, and S.-P. Xie, 2003: Atmospheric Response to Zonal Variations in Midlatitude SST: Transient and Stationary Eddies and Their Feedback. *J. Climate*, **16**, 3314 - 3329.

Kang, S.M., I.M. Held, D.M.W. Frierson, and M. Zhao, 2008: The Response of the ITCZ to Extratropical Thermal Forcing: Idealized Slab-Ocean Experiments with a GCM. *J. Climate*, **21**, 3521 - 3532.

Kang, S.M., D.M.W. Frierson, and I.M. Held, 2009: The Tropical Response to Extratropical Thermal Forcing in an Idealized GCM: The Importance of Radiative Feedbacks and Convective Parameterization. *J. Atmos. Sci.*, **66**, 2812 - 2827.

Kelly, K.A., R.J. Small, R.M. Samelson, B. Qiu, T.M. Joyce, Y.-O. Kwon, and M.F. Cronin, 2010: Western Boundary Currents and Frontal Air-Sea Interaction: Gulf Stream and Kuroshio Extension. *J. Climate*, **23**, 5644 - 5667.

Kidson, J.W., 1988: Interannual Variations in the Southern Hemisphere Circulation. *J. Climate*, **1**, 1177 - 1198.

Kilpatrick, T.J., N. Schneider, and B. Qiu, 2016: Atmospheric Response to a Midlatitude SST Front: Along front winds. *J. Atmos. Sci.*, **73**, 3489 - 3509.

Kushnir, Y., W.A. Robinson, I. Blade, N.M.J. Hall, S. Peng, and R. Sutton, 2002: Atmospheric GCM Response to Extratropical SST anomalies: Synthesis and Evaluation. *J. Climate*, **15**, 2233 - 2256.

Kwon, Y.-O., M.A. Alexander, N.A. Bond, C. Frankignoul, H. Nakamura, B. Qiu, and L. Thompson, 2010: Role of the Gulf Stream and Kuroshio-Oyashio Systems in Large-Scale Atmosphere-Ocean Interaction: A Review. *J. Climate*, **23**, 3249 - 3281.

Kwon, Y.-O., and T. M. Joyce, 2013: Northern Hemsiphere Winter Atmospheric Transient Eddy Heat Fluxes and the Gulf Stream and Kuroshio-Oyashio Extension Variability. *J. Climate*, **26**, 9839 - 9859.

Limpasuvan, V., and D.L. Hartmann, 1999: Wave-Maintained Annular Modes of Climate Variability. *J. Climate*, **13**, 4414 - 4429.

Lindzen, R.S., and S. Nigam, 1987: On the Role of Sea Surface Temperature Gradients in Forcing Low-Level Winds and Convergence in the Tropics. *J. Atmos. Sci.*, **44**, 2418 - 2436.

Lintner, B.R., and J.C.H. Chiang, 2006: Adjustment of the Remote Tropical Climate to El Niño Conditions. *J. Climate*, **20**, 2544 - 2557.

Lorenz, D.J., and D.L. Hartmann, 2001: Eddy-Zonal Flow Feedback in the Southern Hemsiphere. *J. Atmos. Sci.*, **58**, 3312 - 3327.

Lorenz, D.J., and D.L. Hartmann, 2003: Eddy-Zonal Flow Feedback in the Northern Hemisphere Winter. *J. Climate*, **16**, 1212 - 1227.

Madden, R.A., and P.R. Julian, 1994: Observations of the 40 - 50 Day Tropical Oscillation - A Review. *Mon. Wea. Rev.*, **122**, 814 - 837.

Maloney, E.D., and A.H. Sobel, 2007: Idealized Hot Spot Experiments with a General Circulation Model. *J. Climate*, **20**, 908 - 925.

Mantua, N.J., S.R. Hare, Y. Zhang, J.M. Wallace, and R.C. Francis, 1997: A Pacific Interdecadal Climate Oscillation with Impacts on Salmon Production. *Bull. Amer. Meteor. Soc.*, **78**, 1069 - 1079.

Masunaga, R., H. Nakamura, T. Miyasaka, K. Nishii, and Y. Tanimoto, 2015: Separation of Climatological Imprints of the Kuroshio Extension and Oyashio Fronts on the Wintertime Atmospheric Boundary Layer: Their Sensitivity to SST Resolution Prescribed for Atmospheric Reanalysis. *J. Climate*, **28**, 1764 - 1787.

Masunaga, R., H. Nakamura, T. Miyasaka, K. Nishii, and B. Qiu, 2016: Interannual modulations of oceanic imprints on the wintertime atmospheric boundary layer under the changing dynamical regimes of the Kuroshio Extension. *J. Climate*, **29**, 3273 - 3296.

Medeiros, B., B. Stevens, S. Bony, 2015: Using aquaplanets to understand the robust responses of comprehensive climate models to forcing. *Clim. Dyn.*, **44**, 1957 - 1977.

Medeiros, B., D.L. Williamson, and J.G. Olson, 2016: Reference aquaplanet climate in the Community Atmosphere Model, Version 5. *J. Adv. Model. Earth Syst.*, **8**, 406 - 424.

Michel, C. and G. Rivieré, 2014: Sensitivity of the Position and Variability of the Eddy-Driven Jet to Different SST Profiles in an Aquaplanet General Circulation Model. *J. Atmos. Sci.*, **71**, 349 - 371.

Minobe, S., A. Kuwano-Yoshida, N. Komori, S-P. Xie, and R.J. Small, 2008: Influence of the Gulf Stream on the troposphere. *Nature*, **452**, 206 - 210.

Minobe, S., M. Miyashita, A. Kuwano-Yoshida, H. Tokinaga, and S-P. Xie, 2010: Atmospheric Response to the Gulf Stream: Seasonal Variations. *J. Climate*, **23**, 3699 - 3719.

Nakamura, H., G. Lin, and T. Yamagata, 1997: Decadal Climate Variability in the North Pacific during the Recent Decades. *Bull. Amer. Meteor. Soc.*, **78**, 2215 - 2225.

Nakamura, H., T. Sampe, Y. Tanimoto, and A. Shimpo, 2004: Observed Associations Among Storm Tracks, Jet Streams and Midlatitude Oceanic Fronts. *Geophys. Mono.*, **147**, 329 - 346.

Nakamura, H., T. Sampe, A. Goto, W. Ohfuchi, and S-P. Xie, 2008: On the importance of midlatitude oceanic frontal zones for the mean state and dominant variability in the tropospheric circulation. *Geophys. Res. Lett.*, **35**, L15709, doi:10.1029/2008GL034010.

Nakamura, M. and S. Yamane, 2010: Dominant Anomaly Patterns in the Near-Surface Baroclinicity and Accompanying Anomalies in the Atmosphere and Oceans. Part II: North Pacific Basin. *J. Climate*, **23**, 6445 - 6467.

Neale, R.B., and B.J. Hoskins, 2000a: A standard test for AGCMs including their physical parameterizations: I: The proposal. *Atmos. Sci. Lett.*, **1**, doi:10.1006/asle.2000.0019.

Neale, R.B., and B.J. Hoskins, 2000b: A standard test for AGCMS including their physical parameterizations. II: Results for the Met Office Model. *Atmos. Res. Lett.*, **1**, doi:10.1006/asle.2000.0020.

Neale, R.B., et al., 2010: Description of the NCAR Community Atmosphere Model (CAM 5.0), *Tech. Rep. TN-486+STR*, Natl. Cent. for Atmos. Res., Boulder, Colo.

Newman, M., M.A. Alexander, T.R. Ault, K.M. Cobb, C. Deser, E. Di Lorenzo, N.J. Mantua, A.J. Miller, S. Minobe, H. Nakamura, N. Schneider, D.J. Vimont, A.S. Phillips, J.D. Scott, and C.A. Smith, 2016: The Pacific Decadal Oscillation, Revisited. *J. Climate*, **29**, 4399 - 4427.

Nonaka, M., and S-P. Xie, 2003: Covariations of Sea Surface Temperature and Wind over the Kuroshio and Its Extension: Evidence for Ocean-to-Atmosphere Feedback, *J. Climate*, **16**, 1404 - 1413.

O'Neill, L.W., D.B. Chelton, and S.K. Esbensen, 2003: Observations of SST-Induced Perturbations of the Wind Stress Field over the Southern Ocean on Seasonal Timescales. *J. Climate*, **16**, 2340 - 2354.

O'Reilly, C.H., and A. Czaja, 2015: The response of the Pacific storm track and atmospheric circulation to Kuroshio Extension variability. *Q. J. R. Meteorol. Soc.*, **141**, 52 - 66.

O'Reilly, C.H., S. Minobe, A. Kuwano-Yoshida, and T. Woolings, 2017: The Gulf Stream influence on wintertime North Atlantic jet variability. *Q. J. R. Meteorol. Soc.*, **143**, 173 - 183.

Ogawa, F., H. Nakamura, K. Nishi, T. Miyasaka, and A. Kuwano-Yoshida, 2016: Importance of Midlatitude Oceanic Frontal Zones for the Annular Mode Variability: Interbasin Differences in the Southern Annular Mode Signature. *J. Climate*, **29**, 6179 - 6199.

Palmer, T.N., and Z. Sun, 1985: A modelling and observational study of the relationship between sea surface temperature in the north-west Atlantic and the atmospheric general circulation. *Q. J. R. Meteorol. Soc.*, **111**, 947 - 975.

Parfitt, R., A. Czaja, S. Minobe, and A. Kuwano-Yoshida, 2016: The atmospheric frontal response to SST perturbations in the Gulf Stream region. *G. R. L.*, DOI: 10.1002/2016GL067723.

Piazza, M., L. Terray, J. Boé, E. Maisonnave, E. Sanchez-Gomez, 2015: Influence of small-scale North Atlantic sea surface temperature patterns on the marine boundary layer and free troposphere: a study using the atmospheric ARPEGE model. *Clim. Dyn.*, DOI 10.1007/s00382-015-2669-z.

Quadrelli, R., and J.M. Wallace, 2004: A Simplified Linear Framework for Interpreting Patterns of Northern Hemisphere Wintertime Climate Variability. *J. Climate*, **17**, 3728 - 3744.

Révelard, A., C. Frankignoul, and N. Sennéchael, 2016: Influence of the Decadal Variability of the Kuroshio Extension on the Atmospheric Circulation in the Cold Season. *J. Climate*, **29**, 2123 - 2144.

Riviére, G., 2009: Effect of Latitudinal Variations in Low-Level Baroclinicity on Eddy Life Cycles and Upper-Tropospheric Wave-Breaking Processes. *J. Atmos. Sci.*, **66**, 1569 - 1592.

Sampe, T., H. Nakamura, A. Goto, and W. Ohfuchi, 2010: Significance of a Midlatitude SST Frontal Zone in the Formation of a Storm Track and an Eddy-Driven Westerly Jet. *J. Climate*, **23**, 1793 - 1814.

Sample, T., H. Nakamura, and A. Goto, 2013: Potential Influence of a Midlatitude Oceanic Frontal Zone on the Annular Variability in the Extratropical Atmosphere as Revealed by Aqua-Planet Experiments. *J. Met. Soc. Jap.*, **91A**, 243 - 267.

Schneider, N., and B. Qiu, 2015: The atmospheric response to weak sea surface temperature fronts. *J. Atmos. Sci.*, **72**, 3356 - 3377.

Seo, H., Y.-O. Kwon, T.M. Joyce, and C. Ummenhofer, 2017: On the Predominant Nonlinear Response to the Extratropical Atmosphere to Meridional Shifts of the Gulf Stream. *J. Climate*, **30**, 9679 - 9702.

Shaw, T.A., M. Baldwin, E.A. Barnes, R. Caballero, C.I. Garfinkel, Y.-T. Hwang, C. Li, P.A. O'Gorman, G. Riviére, I.R. Simpson, and A. Voigt, 2016: Storm track processes and the opposing influences of climate change. *Nat. Geos.*, DOI: 10.1038/NGEO2783.

Shaw, T.A., and A. Voigt, 2016: Understanding the Links between Subtropical and Extratropical Circulation Responses to Climate Change Using Aquaplanet Model Simulations. *J. Climate*, **29**, 6637 - 6657.

Sheldon, L., and A. Czaja, 2013: Seasonal and interannual variability of an index of deep atmospheric convection over western boundary currents. *Q. J. R. Meteorol. Soc.* DOI:10.1002/qj.2103.

Small, R.J., S.P. DeSzoeke, S.-P. Xie, L. O'Neill, H. Seo, Q. Song, P. Cornillon, M. Spall, and S. Minobe, 2008: Air-sea interaction over ocean fronts and eddies. *Dyn. Atmos. Ocean.*, **45**, 274 - 319.

Small, R.J., R.A. Tomas, F.O. Bryan, 2014: Storm track response to ocean fronts in a global high-resolution climate model. *Clim. Dyn.*, DOI 10.1007/s00382-013-1980-9.

Smirnov, D., M. Newman, and M.A. Alexander, 2014: Investigating the Role of Ocean-Atmosphere Coupling in the North Pacific Ocean. *J. Climate*, **27**, 592 - 606.

Smirnov, D., M. Newman, M.A. Alexander, Y-O. Kwon, and C. Frankignoul, 2015: Investigating the Local Atmospheric Response to a Realistic Shift in the Oyashio Sea Surface Temperature Front. *J. Climate*, **28**, 1126 - 1147.

Sugimoto, S., and K. Hanawa, 2011: Roles of SST Anomalies on the Wintertime Turbulent Heat Fluxes in the Kuroshio-Oyashio Confluence Region: Influences of Warm Eddies Detached from the Kuroshio Extension. *J. Climate*,**24**, 6551 - 6561.

Sugimoto, S., 2014: Influence of SST Anomalies on Winter Turbulent Heat Fluxes in the Eastern Kuroshio-Oyashio Confluence Region. *J. Climate*, **27**, 9349 - 9358.

Taguchi, B., H. Nakamura, M. Nonaka, N. Komori, A. Kuwano-Yoshida, K. Takaya, and A. Goto, 2012: Seasonal Evolutions of Atmospheric Response to Decadal SST Anomalies in the North Pacific Subarctic Frontal Zone: Observations and a Coupled Model Simulation. *J. Climate*, **25**, 111 - 139.

Thompson, D.W.J., and J.M. Wallace, 1998: The Arctic Oscillation signature in the wintertime geopotential height and temperature fields. *G. R. L.*, **25**, 1297 - 1300.

Thompson, D.W.J., and J.M. Wallace, 2000: Annular Modes in the Extratropical Circulation. Part I: Month-to-Month Variability. *J. Climate*, **13**, 1000 - 1016.

Trenberth, K.E., W.G. Large, and J.G. Olson, 1990: The Mean Annual Cycle in Global Ocean Wind Stress. *J. Phys. Ocean.*, **20**, 1742 - 1760.

Trenberth, K.E., and D.P., Stepaniak, 2003: Covariability of Components of Poleward Atmospheric Energy Transports on Seasonal and Interannual Timescales. *J. Climate*, **16**, 3691 - 3705.

Walker, Sir G.T., and E.W. Bliss, 1932: World Weather V. *Mem. Roy. Meteoro. Soc.*, **4**, 53 - 84.

Wallace, J.M., and D.S. Gutzler, 1980: Teleconnection in the Geopotential Height Field during the Northern Hemisphere Winter. *Mon. Wea. Rev.*, **109**, 784 - 812.

Wallace, J.M., and D.W.J. Thompson, 2002: The Pacific Center of Action of the Northern Hemisphere Annular Mode: Real or Artifact?. *J. Climate*, **15**, 1987 - 1991.

White, R.H., A.A. McFarlane, D.M.W. Frierson, S.M. Kang, Y. Shin, and M. Friedman, 2018: Tropical Precipitation and Cross-Equatorial Heat Transport in Reponse to Localized Heating: Basin and Hemisphere Dependence. *G. R. L.*, **45**, 11949 - 11958.

Williamson, D.L., M. Blackburn, K. Nakajima, W. Ohfuchi, Y.O. Takahashi, Y.-Y. Hayashi, H. Nakamura, M. Ishiwataria, J.L. McGregor, H. Borth, V. Wirth, H. Frank, P. Bechtold, N.P. Wedi, H. Tomita, M. Satoh, M. Zhao, I.M. Held, M.J. Suarez, M.-I. Lee, M. Watanabe, M. Kimoto, Y. Liu, Z. Wang, A. Molod, K. Rajendran, A. Kitoh, and R. Stratton, 2013: The Aqua-Planet Experiment (APE): Response to Changed Meridional SST Profile. *J. Meteor. Soc. Japan*, **91A**, 57 - 89.

Wills, S.M., D.W.J. Thompson, and L.M. Ciasto, 2016: On the Observed Relationships between Variability in Gulf Stream Sea Surface Temperatures and the Atmospheric Circulation over the North Atlantic. *J. Climate*, **29**, 3719 - 3730.

Wills, S.M., and D.W.J. Thompson, 2018: On the Observed Relationships between Wintertime Variability in Kuroshio-Oyashio Extension Sea Surface Temperatures and the Atmospheric Circulation over the North Pacific. *J. Climate*, **31**, 4669 - 4681.

Wright, P.B., J.M. Wallace, T.P. Mitchell, and C. Deser, 1988: Correlation Structure of the El Niño/Southern Oscillation Phenomenon. *J. Climate*, **1**, 609 - 625.